

Politecnico di Torino

EPFL



Politecnico di Torino

Laurea Magistrale in Environmental and Land Engineering

A.y. 2025/2026

Graduation Session September 2026

Observing and modelling height and mass flux of blowing snow in East Antarctica

Supervisors:
Rainette Engbers
Michael Lehning
Costantino Manes

Candidate:
Lorena Accossato

Abstract

Drifting and blowing snow are wind-driven phenomena of snow transport, by saltation and suspension respectively, that occur frequently over the Antarctic Ice Sheet. They are relevant at both local and regional scales, and can significantly influence the surface mass and energy balances, by redistributing snow and through the sublimation of the transported particles.

These processes are not fully understood, and constitute an active area of research, both regarding their physical mechanisms and their impacts. Estimates of blowing snow sublimation over Antarctica, for instance, differ widely, with model-derived values several times lower than the satellite-based estimate. Despite its relevance, drifting and blowing snow are mostly absent from regional and global climate models. This is a limitation over snow-covered areas, where the processes couple the snowpack and the atmosphere in a two-way exchange of mass, moisture and heat that is lost when they are omitted. Some models that include them are CRYOWRF, MAR and RACMO.

This work makes use of two years of multi-instrument observations of blowing snow at Princess Elisabeth Antarctica (PEA) station, in East Antarctica. The instruments specific to blowing snow are two near-surface mass-flux sensors, and a ceilometer, which resolves its vertical dimension. Together with standard meteorological and eddy-covariance measurements, they are used first to characterise blowing snow at the station, its frequency, intensity, vertical extent and the meteorological conditions under which it occurs, within the three regimes that describe the climate at PEA; and then to validate the blowing snow scheme in the state-of-the-art model CRYOWRF. To this end, one simulation of a blowing snow event was run for each of the three meteorological regimes. The validation concerned both the mass flux at the surface and the height of the blowing snow layer.

Blowing snow at PEA is found to be concentrated in the least frequent, cyclone-driven regime. Katabatic blowing snow events are rarer but produce the densest near-surface fluxes. In the simulations, the model shows a cold and dry bias and overestimates the wind speed. The near-surface mass flux is largely underestimated in every event, despite the wind overestimation, because the computed threshold friction velocity is too high. The vertical extent of the layer is instead well reproduced in the katabatic event, where the model resolves the gravity waves that set its height; this is lost at coarser resolution, where the waves are no longer resolved. Both the underestimated surface flux and the loss of the layer at coarse resolution may contribute to continental estimates of blowing snow sublimation from models being low compared to the satellite-derived estimate.

This study characterises blowing snow at PEA and provides, through the ceilometer, what is to our knowledge the first validation of a modelled blowing snow layer in its vertical extent. It shows that CRYOWRF, in katabatic conditions, reproduces the height of the layer when the relevant dynamics are resolved, despite an underestimation of the near-surface mass fluxes. The origin of the overly high transport threshold should be further investigated, starting from the modelled snow microstructure from which it is computed. We also highlight the relevance of topography, and consequently of horizontal resolution, to the representation of blowing snow. Reproducing it at a resolution able to resolve the topography remains a challenge for the large-scale, long-term simulations on which Antarctic mass-balance estimates depend.

Table of Contents

List of Tables VI

List of Figures VIII

Introduction 1

1 PEA station and data 7

1.1 Princess Elisabeth Antarctica station: site description 7

1.2 Instrumentation at Princess Elisabeth Antarctica station 7

1.2.1 Surface AWS 9

1.2.2 Snow Particle Counter 10

1.2.3 FlowCapt 12

1.2.4 Ceilometer 12

1.2.5 Micro Rain Radar 14

2 Methods 15

2.1 Meteorological clustering 15

2.2 The ceilometer's blowing snow detection algorithm 17

2.3 Statistical analysis: definition of DS and BS events 20

2.4 Simulations with CRYOWRF 21

2.4.1 The blowing snow scheme in CRYOWRF 22

2.4.2 Selection of events 23

2.4.3 Model setup 24
2.4.4 Validation against the observations 24

3 Results 27
3.1 Meteorological conditions in 2024 and 2025 27
3.2 Results of the meteorological clustering 27
3.2.1 The three regimes 28
3.2.2 Classification during transport events 29
3.3 Performance of the blowing snow detection algorithm 30
3.4 Statistical analysis 31
3.5 Validation of CRYOWRF 33
3.5.1 Atmospheric variables 34
3.5.2 Blowing snow mass flux 35
3.5.3 Blowing-snow cloud top 37

4 Discussion 41
4.1 Wind-driven snow transport at PEA 41
4.2 Cyclonic influence on simulation's accuracy 42
4.3 Underestimation of blowing snow fluxes 43
4.4 Validation of the vertical dimension of the blowing snow cloud . . . 47

Conclusion 51

Outlook 53

A Meteorological clustering 55
A.1 Detrending 55
A.2 Choice of the clustering period 57
A.3 Effect of temporal resolution 58

B Additional figures of the simulated events 61

B.1 Synoptic maps and vertical transect 61

B.2 Mass flux timeseries: transitional and warm synoptic 64

B.3 Blowing-snow cloud height 66

Bibliography 71

List of Tables

1.1 Heights above the snow surface of the instruments installed on the SFC AWS that were used in the study. The heights at the start of 2024 (12 February) and the end of 2025 (22 December) were measured directly during surveys, the remaining values are computed from the change in distance from snow surface height recorded by the SR-50A; "Cold Kat" and "Trans, Warm Syn" indicate the three simulations run in CRYOWRF, respectively Cold Katabatic, Transitional, and Warm Synoptic (discussed in section 2.4). 11

2.1 Simulation windows for the three selected events. 23

2.2 Mean values of meteorological variables over each selected event. P is surface pressure, T_a air temperature, ΔT_{inv} the near-surface temperature inversion, q specific humidity, $\mathrm{LW}_{\downarrow}$ incoming longwave radiation, WS wind speed and WD wind direction. 24

3.1 Annual mean conditions at PEA. 2009–2010: Gorodetskaya et al. (2013); 2024–2025: this study. 28

3.2 Mean conditions of the three regimes. Gorodetskaya 2009/2010: daily clustering; combined (2023–2025): hourly clustering, this study. 30

3.3 Frequency, near-surface mass flux and ceilometer cloud-top height of the 5 min categories (clustering-independent, 2024–2025). Fluxes in $\mathrm{g\,m^{-2}\,s^{-1}}$, height in m. 32

3.4 BS near-surface mass flux and ceilometer cloud-top height by regime (transport-based clustering). Fluxes in $\mathrm{g\,m^{-2}\,s^{-1}}$, height in m. . . . 33

3.5 Validation of the near-surface atmospheric variables against the SFC AWS, per event and pooled (overall). MAE and bias are in the units of each variable; r is the Pearson correlation. N is the number of observation-measurement pairs used for this comparison. The bias of wind direction is omitted because the variable is circular. 35

3.6 Validation of the blowing-snow mass flux and mean particle radius against the FlowCapt (FC) and SPC, per event. MAE and bias are in the units given in the first column; PBIAS is the percent bias (negative = underestimation) and applies to the fluxes only; N is the number of paired points and r the Pearson correlation. 36

A.1 Warm Synoptic regime across all years: per-year hourly clustering (2023–2025), combined 3-year hourly clustering, and Gorodetskaya et al. (2013) (2009/2010, daily). 57

A.2 Mean conditions of the Warm Synoptic regime within the combined classification, broken down by year. 2009–2010 from Gorodetskaya et al. (2013) (daily); 2023–2025: combined 3-year hourly clustering, this study. 58

List of Figures

1 (a) The average April through October blowing snow frequency for the period 2007–2015. (b) The average annual blowing snow sublimation for the same period as in (a). *Figure from Palm et al. (2017), The Cryosphere, 11, 2555–2569, https://doi.org/10.5194/tc-11-2555-2017. Reproduced under the Creative Commons Attribution 3.0 License.* 3

1.1 Location of the meteorological observatory at the Belgian Princess Elisabeth station, north of the Sør Rondane Mountains. Source: Landsat Image Mosaic of Antarctica (LIMA) Project, `http://lima.usgs.gov/` (last access: 8 June 2018). Colours in the inset and contours on the main figure denote topography height (metres). *Figure from Souverijns et al. (2018), distributed under the Creative Commons Attribution 4.0 License.* 8

1.2 Overview of the PEA station and location of its instruments: the Tall Tower and surface AWS are indicated in the blue circle, they are located approximately 100 m to the east of the station; the ceilometer and Micro Rain Radar are positioned on the roof of the station. 9

1.3 Overview of the Tall Tower (left) and surface automatic weather station (SFC AWS), located next to it (right). Instruments are indicated. 10

2.1 Typical ceilometer backscatter profiles for the two blowing-snow categories detected by the algorithm (Sect. 2.2): clear-sky blowing snow (cat 1, left) and blowing snow with cloud or precipitation (cat 2, right). For each category the solid line is the median profile over a sample of detected 5-minute periods, the shaded band the 25–75th percentile range, and the dashed line the clear-sky reference profile. Heights are given above the instrument. Notice the peak in backscatter in category 2, which represents clouds, or clouds and precipitation. 20

3.1 Wind roses for the three regimes (combined 2023–2025 hourly classification), from the 1-minute wind data of the hours in each regime. The height of each bar shows the fraction of time the wind came from a given direction, coloured by wind speed. Notice how the direction of the katabatic wind is south- southeast, and turns progressively more easterly as synoptic influence increases. The warm synoptic regime has the largest wind speeds. 29

3.2 Timeseries of the FlowCapt and SPC simulated (domain 5) and measured mass fluxes and mean particle radius, with their probability densities, for the Cold Katabatic event. 37

3.3 Top: timeheight plot, for the cold katabatic event, of the difference between the ceilometer backscatter and the clear sky reference profile [10^{-5} km^{-1} sr^{-1}]; the black line represents the blowing snow cloud top detected by the same algorithm. Bottom: timeheight plot, for the same event, of blowing snow mixing ratio in CRYOWRF ($kg\,kg^{-}1$); the black line represents the height at which the mixing ratio is equal to $10^{-6}\,kg\,k^{-1}$, threshold chosen to define the top of the blowing snow cloud in CRYOWRF. Notice how the model cloud height closely follows the observed one. 38

4.1 Mass flux vs friction velocity of both FlowCapt and SPC measurements, and corresponding value from CRYOWRF. Median modelled threshold friction velocity is represented as a dotted line. Observed friction velocities are derived from eddy-covariance measurements by the sonic anemometer on the SFC AWS. The threshold friction velocity here is too high compared to the measured friction velocities, which limitates the amount of snow entrained in saltation. 44

4.2 Timeheight plot of the blowing snow layer during the Cold Katabatic event, from the ceilometer and from CRYOWRF at the five different resolutions. Top left: ceilometer attenuated backscatter minus the clear-sky reference profile ($\mathrm{sr^{-1}\,m^{-1}}$), with the blowing snow layer top retrieved by the detection algorithm of Section 2.2 (black line). Remaining panels: modelled blowing snow mixing ratio ($\mathrm{kg\,kg^{-1}}$) at 27 km, 9 km, 3 km, 1 km and 200 m horizontal resolution. In each, the black line marks the modelled cloud top, defined as the height where the mixing ratio falls below $10^{-6}\,\mathrm{kg\,kg^{-1}}$, and the dashed lines the $10^{-8}\,\mathrm{kg\,kg^{-1}}$ iso-values. Heights are above ground level. The cloud is seen at 200 m and 1 km resolution, but becomes completely flat at 3 and 9 km, and vanishes at 27 km resolution. 49

A.1 Seasonal trend from climatology (computed using data from 2023 to 2025) and hourly data of air temperature in 2024. 56

A.2 Diurnal cycle of air temperature by month from climatology (computed using data from 2023 to 2025). 56

A.3 Ward clustering dendrograms for 2023–2025 at daily (left) and hourly (right) resolution. At daily resolution Ward is applied to all days, while at hourly resolution it is applied to a subset of 15 000 hours (the remaining hours are then assigned to the nearest cluster centroid in the standardised space). Each leaf at the bottom is one observation, and branches merge upwards into larger groups. Cutting the tree at $k = 3$ gives the three regimes (blue: cold katabatic; orange: transitional synoptic; red: warm synoptic), while grey links join different regimes above the cut. 59

B.1 The Cold Katabatic event on 2024-05-13 12:00 UTC from the CRYOWRF simulation. Left: mean sea level pressure in domain 1 (hPa). Right: 10 m wind speed ($\mathrm{m\,s^{-1}}$, shading) and wind vectors in domain 5; the reference arrow is $10\,\mathrm{m\,s^{-1}}$. PEA is marked by the black triangle, and the 2,000 and 3,000 m elevation contours are shown. In the right panel, the oval indicates the gap in the mountains, through which the flow is channeled (its direction highlighted with the three arrows). A low-pressure system lies to the east of the station (left), and the associated pressure gradient enhances the drainage flow and channels it through the Sør Rondane Mountains (right), producing the unusually high katabatic wind speeds visible near PEA in the right panel. 61

B.2 Evolution of the mean sea level pressure (hPa) during the two synoptic events, from the CRYOWRF simulation (domain 1), at four times: (a) 2025-04-23 06:00, (b) 2025-04-23 18:00, (c) 2025-04-24 01:00 and (d) 2025-04-24 12:00 UTC. PEA is marked by the black triangle. In (a) a single cyclone approaches the coast north of PEA, driving the Transitional Synoptic event. A second cyclone then develops to its east (b), and the two systems rotate around each other in a Fujiwhara interaction (c), until one is absorbed by the other into a single low (d). This low drives the Warm Synoptic event and brings precipitation to PEA. Sea-level reduction is not meaningful over the high interior. 62

B.3 Vertical cross-section along the mean flow (142°) through PEA for the cold katabatic event, 23:00 UTC 13 May 2024 (domain d05, 200 m). Axis: latitude/longitude along the transect; red dashed line = PEA; brown = model terrain. Panels: (a) potential temperature θ (°, with isolines); (b) wind speed ($\mathrm{m\,s^{-1}}$); (c) vertical velocity w ($\mathrm{m\,s^{-1}}$; red = ascent, blue = descent); (d) blowing-snow mixing ratio q_{bs} ($\mathrm{g\,kg^{-1}}$, log scale), magenta line = $q_{\mathrm{bs}} = 10^{-6}$ kg kg^{-1} isoline (top of the blowing-snow layer). In (b) and (c), arrows show the in-plane wind (reference vector $20\,\mathrm{m\,s^{-1}}$). The gravity waves cause updrafts with high vertical velocities, which at this precise time reach $4.5\,\mathrm{m\,s^{-1}}$, and determine the height of the cloud. 63

B.4 Same as Figure 3.2, but for the Transitional Synoptic event 64

B.5 Same as Figure 3.2, but for the Warm Synoptic event 65

B.6 Barplots, for the Cold Katabatic event, of MAE, Bias, and Pearson correlation of tested blowing snow mixing ratio thresholds to define the cloud top in CRYOWRF, compared to the cloud top obtained from the ceilometer algorithm. $bs_qi = 10^{-6}$ achieve the lowest MAE and highest correlation, and the second lowest bias. Correlation stays stable across 2 orders of magnitude, indicating that, independently of the chosen threshold, the evolution of the cloud is well represented. 66

B.7 Timeseries, for the Cold Katabatic event, of the cloud top obtained from the ceilometer algorithm (black) and from CRYOWRF (blue), where the top in the model is defined as the height where the blowing snow mixing ratio reaches a selected threshold. Thresholds from $10^{-8}\,\mathrm{kg\,kg^{-1}}$ to $10^{-5}\,\mathrm{kg\,kg^{-1}}$ are shown here. $10^{-6}\,\mathrm{kg\,kg^{-1}}$ follows the observed cloud best. 67

B.8 Blowing snow cloud top observed by the ceilometer (retrieved with the ceilometer algorithm of Section 2.2) and modelled by CRYOWRF. Modelled cloud top (colored lines) is defined as the height where the blowing snow mixing ratio is equal to $10^{-6}\,\mathrm{kg\,kg^{-1}}$. The three panels show the three simulated events. The black fine line is the cloud top retrieved from the ceilometer at 5 minute resolution, the black line instead the points used for comparison with CRYOWRF. In the two synoptic events, the transitional one especially, the modelled cloud reaches more rarely the selected threshold of $bs_qi = 10^{-6}\,\mathrm{kg\,kg^{-1}}$. 68

B.9 Same as Figure 4.2, but for the Transitional Synoptic event instead. In this event, there is no significant change in the simulated blowing snow cloud until up to 27 km horizontal resolution, where it disappears. 69

B.10 Same as Figure 4.2, but for the Warm Synoptic event instead. In this event, there is no significant change in the simulated blowing snow cloud until up to 27 km horizontal resolution, where it disappears. . 69

Introduction

Drifting and blowing snow are wind-driven phenomena of snow transport. Their definitions differ depending on the field. In meteorological observation the two are separated by height and by their effect on visibility: following the WMO convention, snow raised by the wind below eye level (about 1.8 m) is called drifting snow and does not reduce horizontal visibility, while snow lifted above that height reduces visibility, and is called blowing snow (Organization, 2017). This is also the distinction that is relevant for road-safety applications. In snow transport modelling the two terms are instead associated with the mode of transport: drifting snow with the saltation layer, in which the particles are moved close to the surface in ballistic trajectories within a shallow layer (of the order of 0.15 m), and blowing snow with the particles carried higher and farther in turbulent suspension (Nishimura et al., 2005; Bintanja, 2000).

Drifting and blowing snow are frequent and widespread on the Antarctic Ice Sheet (AIS), more than anywhere else on Earth (Palm et al., 2011), and prevail in katabatic wind zones (Palm et al., 2017). They have a significant impact on the surface mass balance (SMB) of the AIS through snow redistribution (Lenaerts et al., 2012a; Agosta et al., 2019) and blowing snow sublimation (Palm et al., 2017; Thiery et al., 2012; Gadde et al., 2024; Gerber et al., 2023). Equation 1 represents the surface mass balance:

$$\frac{dM}{dt} = P - \nabla D_{bs} - E_{bs} \pm E - R \tag{1}$$

The local mass change rate dM/dt of the snowpack depends on precipitation P, horizontal redistribution of surface snow by wind D_{bs}, sublimation of blowing snow E_{bs}, surface sublimation or condensation E, and runoff R (Armstrong et al., 2008). In this formulation, blowing snow can constitute significant negative terms, with its sublimation and horizontal transport directly reducing the net balance. Erosive winds redistribute snow at the surface, and they can form areas of near-zero net accumulation (wind glaze areas) or even net ablation (blue ice areas) (Gossart

et al., 2020). These surfaces profoundly influence the local surface energy balance (Bintanja, 1999; Scambos et al., 2012) and may enhance surface melt (Lenaerts et al., 2017). At the continental scale, mass loss through wind redistribution and export into the ocean has little influence on SMB (C. Amory, 2020). However, regional and local impacts of snow transport by wind can be substantial (Lenaerts et al., 2012a). Several studies demonstrate its influence on the Antarctic SMB across multiple scales, from kilometer to meter (Dattler et al., 2019; Kausch et al., 2020; Picard et al., 2019). For instance, in coastal areas, wind redistribution is responsible for a net export of mass beyond the ice-sheet margins, which has large potential impacts for sea level rise as well (Scarchilli et al., 2010).

Snow transport begins once the wind friction velocity exceeds a threshold value, which depends on the microstructural properties of the surface snow, such as grain size and bond size between grains (M. Lehning et al., 2000). When wind speeds are high enough, shear stress at the snow surface can dislodge snow grains and entrain them into the air. Larger particles saltate, meaning they are transported along the surface in ballistic trajectories. As they impact the surface, they dislodge more grains, so that drifting and blowing snow are easier to sustain than to initiate. Smaller particles are picked up by turbulent eddies and carried higher and farther; this constitutes suspension (Sharma et al., 2023).

Arguably the most significant impact of blowing snow is through its sublimation, which affects both the surface mass and energy balances. Because the drifting snow particles are aloft, they have a greater area exposed and available to sublimation than those at the surface. As a consequence, blowing snow sublimation is more efficient than surface sublimation. This process causes cooling and moistening of the near-surface air, which reduce the vapour pressure deficit that drives it (Taylor, 1998; Amory et al., 2019), inhibiting further sublimation both at the surface, and of snowdrift, despite ongoing transport by wind. It is therefore a self-limiting process. When integrated over the entire ice sheet, sublimation during snow transport is the dominant wind-driven mass sink. Its quantification is challenging, and studies that estimate sublimation over the Antarctic continent find very different values for it. On the one hand, there are studies based on climate models with a blowing snow scheme to estimate total sublimation of drifting and blowing snow: Gerber et al. (2023) obtain 101 Gtons/year in CRYOWRF v1.0, Gadde et al. (2024) get 175 $\pm$ 7 Gtons/year in RACMO2.3p3, and 115 $\pm$ 4 Gtons/year using a previous version of the blowing snow scheme of the same model version. On the other hand, Palm et al. (2017) estimates it from CALIPSO satellite observations, coupled with atmospheric variables from MERRA-2 reanalysis, and obtains 393 $\pm$ 196 Gtons/year, almost four times the lowest model's estimate.

The pattern of frequency of blowing snow events obtained from both models,

as well as that of their sublimation, is qualitatively similar to that obtained from the satellite observations (Palm et al., 2011; Palm et al., 2017). They showed that blowing snow occurs frequently across large parts of the ice sheet, mainly in the inland zones of East Antarctica, with clear gradients between coastal and inland regions. However, maximum blowing snow sublimation is found within approximately 200 km of the coastline. In these coastal zones, the relatively warmer and drier air masses, which result from adiabatic compression of the katabatic flow during its descent from the plateau to the coast, enhance sublimation of suspended snow particles. In contrast, the maximum frequency of blowing snow occurs considerably further inland. Here, lower air temperatures and higher relative humidity limit sublimation. The overall spatial patterns of blowing-snow transport and sublimation remain relatively stable from year to year (Palm et al., 2011). Both blowing snow frequency and sublimation are shown in Figure 1.

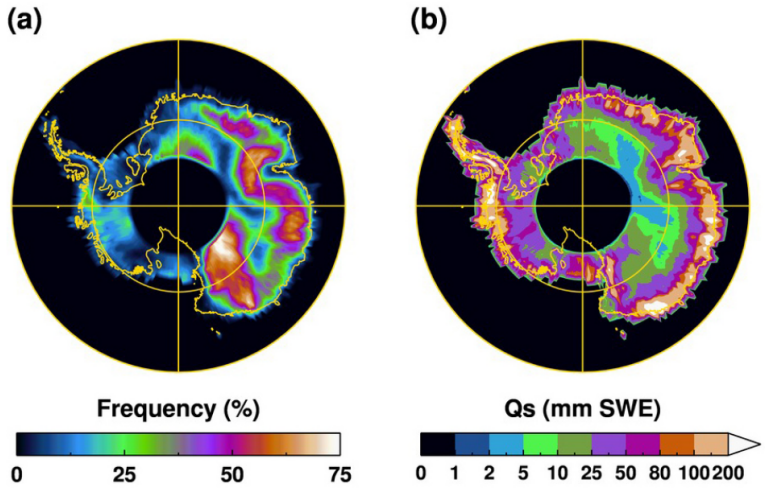


Figure 1: (a) The average April through October blowing snow frequency for the period 2007–2015. (b) The average annual blowing snow sublimation for the same period as in (a). *Figure from Palm et al. (2017), The Cryosphere, 11, 2555–2569, https://doi.org/10.5194/tc-11-2555-2017. Reproduced under the Creative Commons Attribution 3.0 License.*

These continental-scale characteristics are closely linked to Antarctica's large-scale atmospheric circulation. The ice-sheet is surrounded by a belt of extratropical cyclones that generate strong pressure gradients and drive persistent winds over the continent. Blowing snow is therefore the result of both katabatic forcing, due to radiative surface cooling over the high plateau, and synoptic disturbances associated with cyclonic systems. The relative contribution of these drivers varies regionally, shaping the observed distribution of blowing snow frequency, transport, and sublimation. We show that at Princess Elisabeth Antarctica (PEA) station

synoptic forcing drives wind transport of snow (Section 3.4), while katabatic flow leads to blowing snow more rarely, as the station is partly sheltered by the Sør Rondane Mountains.

Future changes in blowing snow are difficult to predict, because the variables governing it are themselves affected by climate change in different, and sometimes opposing, ways. A warming climate is expected to produce, on average, wetter snowpacks, increased atmospheric moisture, and a larger fraction of precipitation falling as rain rather than snow, alongside potential changes in circulation patterns. Because these factors influence blowing snow in competing directions, its response is expected to be highly non-linear and spatially variable. Moreover, since blowing snow is a threshold driven process, and, in some environments, a defining feature of the snow regime itself, its modification could potentially contribute to shifts in snow regimes. Understanding this process and its impacts is therefore important for both interpreting the observed effects of a warming climate, and for projecting its future evolution.

Despite their relevance, blowing snow is mostly absent from regional climate models. Some that explicitly represent it are CRYOWRF (Sharma et al., 2023), RACMO (Lenaerts et al., 2012b) and MAR (Gallée et al., 2001). Lenaerts et al. (2019) noted that the inclusion of processes such as blowing snow had substantially improved the representation of the ice-sheet SMB in regional climate models over the previous decade. Earth System Models, however, including those contributing to CMIP6, are still behind in this respect, as wind-driven snow transport remains a rarely represented process (Krinner et al., 2018). Still, the blowing snow schemes in these models largely rely on simplifying assumptions and parameterisations, and have not been fully validated yet. Together with the large spread in modeled sublimation, this motivates the acquisition of observations against which these models can be evaluated.

Measurements in Antarctica remain scarce in general, and even more so for drifting and blowing snow, due to the continent's remoteness and harsh environmental conditions. In situ mass flux observations, such as the ones analysed in this study, are particularly valuable for validating atmospheric and snow models and for providing ground truth for satellite retrievals. Their limitation is that they are not representative of the high spatial variability of the phenomenon, which on the other hand can be captured by satellite measurements. Moreover, there are limitations to the reliability of these instruments (Sections 1.2.2, 1.2.3). Nevertheless, unlike satellite remote sensing, mass flux point measurements are not limited to periods with no or low cloud cover. Ground-based remote sensing too, like the ceilometer, whose data is employed in this study, is less limited than satellite remote sensing in this sense: while it is true that data are more difficult to interpret in cloudy

conditions, these instruments are valuable, since from them we can estimate the height of the blowing snow cloud.

Data used in this thesis is retrieved from the PEA station, in East Antarctica. There, a comprehensive atmospheric monitoring system is operated, which includes both standard meteorological measurements, a Micro Rain Radar (MRR), which detects snowfall, and instruments specific for blowing snow measurements. These include a Snow Particle Counter and a FlowCapt, which measure surface snow transport near the surface, as well as a ceilometer, which allows observation of blowing snow in its vertical dimension.

In this context, this thesis characterizes drifting and blowing snow at PEA station, and validates the CRYOWRF model, and its blowing snow scheme, under the different meteorological conditions that drive snow transport at the site. Following Gorodetskaya et al. (2013), hourly meteorological data are first classified, through a cluster analysis, into three regimes: Cold Katabatic, Transitional Synoptic, and Warm Synoptic. For each regime, the frequency, the near-surface mass flux, and the vertical extent of snow transport are characterized. Finally, one representative event for each regime is simulated with CRYOWRF. Blowing snow in models has so far been evaluated against near-surface mass fluxes, which constrain the transport at the bottom of the layer but are not informative on its vertical development. The ceilometer at PEA measures precisely this dimension, and allows it to be compared with the model. To our knowledge this quantitative comparison has not been done before.

This thesis is organised as follows. Chapter 1 describes the PEA station and its instrumentation, with particular attention to the sensors used to observe blowing snow. Chapter 2 presents the methods: the clustering of the meteorological data into the three regimes, the ceilometer blowing snow detection algorithm, the definition of the transport events from the instruments, and the setup and validation strategy of the CRYOWRF simulations. Chapter 3 reports the results, from the characterisation of blowing snow at the station to the validation of the model against the surface variables, the near-surface mass fluxes and the vertical extent of the layer. Chapter 4 discusses these results, and the Conclusion and Outlook summarise the main findings and the directions they open.

Chapter 1

PEA station and data

1.1 Princess Elisabeth Antarctica station: site description

The Princess Elisabeth (PEA) station is located at 71.95°S and 23.35°E, in Dronning Maud Land, approximately 173 km inland from the coastline of East Antarctica. It lies at the northern foot of the Sør Rondane Mountains (Fig. 1.1), in the escarpment zone between the coastal area and the inland plateau. The station is anchored on the granite ridge of Utsteinen Nunatak, which runs nearly perfectly north-south, at an altitude of 1382 m above sea level (Fig. 1.2). The Sør Rondane mountain chain extends about 220 km in the east-west direction, with peaks protruding through the ice sheet and rising up to 3300 m above sea level. This particular topographic setting shapes the local climate. Sheltering by the Sør Rondane Mountains reduces the strength of the katabatic flow, while the station remains directly exposed to cyclonic systems approaching the coast. Overall, this leads to a relatively mild climate (Gorodetskaya et al., 2013).

1.2 Instrumentation at Princess Elisabeth Antarctica station

A comprehensive atmospheric monitoring system is operated at Princess Elisabeth Antarctica station. Its main infrastructure consists of a tall meteorological tower (González-Herrero, 2025) and a separate surface automatic weather station (SFC AWS), both located approximately 100 m from the main station buildings (Fig. 1.2), and shown in Fig. 1.3.

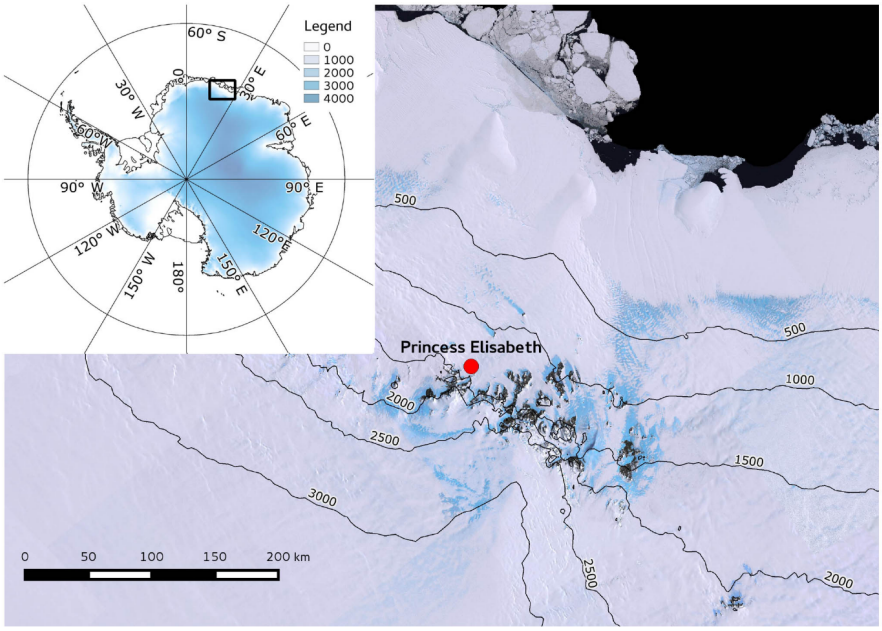


Figure 1.1: Location of the meteorological observatory at the Belgian Princess Elisabeth station, north of the Sør Rondane Mountains. Source: Landsat Image Mosaic of Antarctica (LIMA) Project, `http://lima.usgs.gov/` (last access: 8 June 2018). Colours in the inset and contours on the main figure denote topography height (metres). *Figure from Souverijns et al. (2018), distributed under the Creative Commons Attribution 4.0 License.*

The Tall Tower is equipped with instruments at multiple levels (5m, 10m, 16m, and 26m). These, together with those on the SFC AWS, include sonic anemometers and gas analysers, enabling eddy-covariance measurements of turbulent fluxes, in addition to standard meteorological instruments measuring air temperature, relative humidity, wind speed and direction, and radiation components. Overall, this setup provides a detailed characterisation of the atmospheric boundary layer structure.

Instruments specific to the observation of blowing snow are also present. Two near-surface mass flux instruments are integrated in the SFC AWS: a Snow Particle Counter (SPC), installed at about 0.5 m above the surface, provides a point measurement, while a FlowCapt measures the integrated mass flux over approximately the first metre above surface. Together, they provide vertically resolved information on snow transport intensity close to the ground. In addition, a ceilometer is installed on the roof of the station, which enables detection of the occurrence of blowing snow events and observation of their vertical extent, including the height of the blowing snow cloud. Finally, a vertically pointing Micro Rain Radar (MRR), similarly installed on the roof of the station, allows detection and observation of

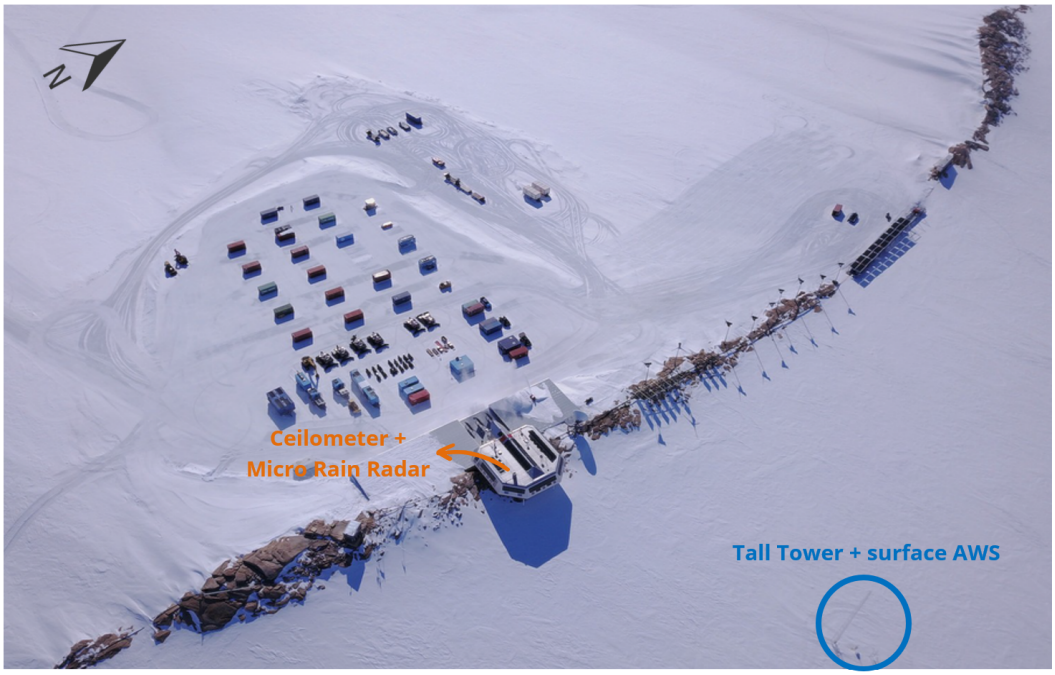


Figure 1.2: Overview of the PEA station and location of its instruments: the Tall Tower and surface AWS are indicated in the blue circle, they are located approximately 100 m to the east of the station; the ceilometer and Micro Rain Radar are positioned on the roof of the station.

precipitating snow.

1.2.1 Surface AWS

Meteorological variables used throughout this work are measured by the surface automatic weather station (SFC AWS), located a few metres from the Tall Tower. Air temperature and relative humidity, from which specific humidity is derived, are measured by a HygroVUE10 sensor. Surface pressure is obtained from the barometer in the LI-7500 gas analyser. Wind speed and direction are recorded by two Young 05108 anemometers, of which the lower one is used throughout. Radiation components are measured by a SN-500SS net radiometer, and the snow surface height is monitored by an acoustic SR-50A sensor.

The raw one-minute records are quality-controlled. Shortwave radiation values outside $[-20,\ 1300]\ \mathrm{W\,m^{-2}}$ are rejected, as well as steps where downwelling shortwave is lower than its upwelling component. Longwave fluxes are considered valid if they lie in the range $[10,\ 400]\ \mathrm{W\,m^{-2}}$, and air temperature if it is above $-60\ ^\circ\mathrm{C}$. Snow surface height is first filtered by the SR-50A internal quality

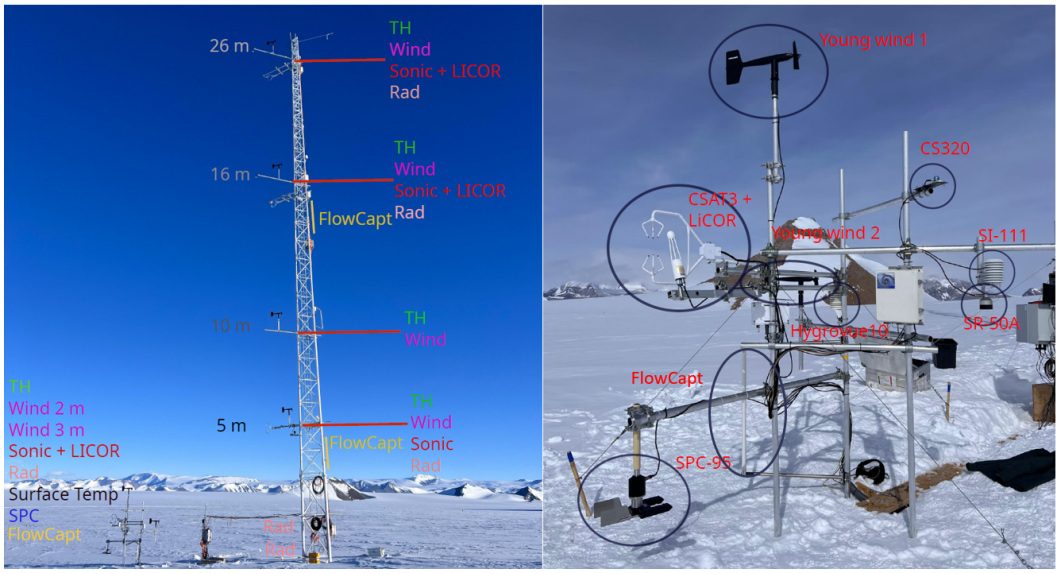


Figure 1.3: Overview of the Tall Tower (left) and surface automatic weather station (SFC AWS), located next to it (right). Instruments are indicated.

flag, then despiked using a daily rolling median. Discarded values and gaps in these meteorological records are filled by linear interpolation. The high-frequency turbulence data from the sonic anemometer, used for eddy correlation, are instead processed with EddyPro.

The instrument heights above the snow surface for each study period are reported in Table 1.1. Note that they change throughout the seasons due to snow erosion and accumulation.

1.2.2 Snow Particle Counter

The Snow Particle Counter (SPC-95, Niigata Electric Co.) measures the size and number of blowing snow particles from the attenuation of a near-infrared beam ($\lambda = 830$ nm) as particles pass through the sampling volume (Niigata Electric Co., Ltd., n.d.). Each particle generates a voltage pulse whose amplitude is proportional to its cross-sectional area. This signal is assigned to one of 64 size classes based on its amplitude, and for each class a representative diameter is derived from factory calibration (Niigata Electric Co., Ltd., 2019). When the sensor temperature deviates from the factory reference by more than ± 10 °C, the size-class boundaries shift and a temperature correction is applied (Niigata Electric Co., Ltd., 2019). Measurements are recorded at 1 s resolution (Niigata Electric Co., Ltd., n.d.) and then averaged to 1 min for analysis, for consistency with SFC AWS data.

Table 1.1: Heights above the snow surface of the instruments installed on the SFC AWS that were used in the study. The heights at the start of 2024 (12 February) and the end of 2025 (22 December) were measured directly during surveys, the remaining values are computed from the change in distance from snow surface height recorded by the SR-50A; "Cold Kat" and "Trans, Warm Syn" indicate the three simulations run in CRYOWRF, respectively Cold Katabatic, Transitional, and Warm Synoptic (discussed in section 2.4).

Instrument	2024			2025		
	12 Feb	Cold Kat (13–14 May)	31 Dec	8 Feb	Trans, Warm Syn (23–25 Apr)	22 Dec
SPC	0.590	0.598	0.686	0.384	0.488	0.430
LI-7500	2.030	2.038	2.126	1.734	1.838	1.780
HygroVUE10	1.550	1.558	1.646	1.374	1.478	1.420
Young wind 2 (lower)	1.740	1.748	1.836	1.664	1.768	1.710
FlowCapt (lower bar)	0.160	0.168	0.256	0.044	0.148	0.090
Radiation SN-500SS-1	1.735	1.743	1.831	1.674	1.778	1.720
SR-50A	1.600	1.608	1.696	1.374	1.478	1.420

The corrected measurements are then used to compute the horizontal mass flux $F\,[\mathrm{kg\,m^{-2}\,s^{-1}}]$ assuming spherical particles:

$$F = \frac{1}{A}\sum_{i=1}^{64}\frac{4}{3}\,\pi\left(\frac{d_i}{2}\right)^3\rho\,N_i \tag{1.1}$$

where d_i is the representative diameter of class i, N_i $[\mathrm{s^{-1}}]$ is the number of particles detected in class i per unit time, $\rho = 917\ \mathrm{kg\,m^{-3}}$ is the ice density, and $A = 50\ \mathrm{mm^2}$ is the sensor sampling area. The SPC cannot distinguish wind-transported snow from precipitation falling from above (Nishimura et al., 2005; Lehning et al., 2002). The measured flux F of equation 1.1 therefore includes both forms of transport.

The SPC is reliable down to very low mass fluxes, its output agreeing well with mechanical snow traps (Sato et al., 1993). Its main limitation lies at the opposite end: at very high particle concentrations two particles may cross the beam at the same instant, so that their overlapping shadows are registered as a single, larger particle. This leads to an undercount of the number of particles and a bias in the retrieved size distribution at the highest fluxes. It is however expected only under intense transport during strong winds (Sato et al. (1993) reports wind speed greater than 15 $m\ s^{-1}$ at 1 m) and close to the surface.

A second limitation concerns the smallest size classes. The measured size distributions show a peak at the lowest diameters, which departs from the gamma

distribution normally found adequate to describe them. This is because the sensitivity is not uniform across the sampling area, and particles crossing the edges of the light beam produce attenuated pulses. Since the diameter is retrieved from the pulse amplitude, these particles are assigned to the lowest size classes, which inflates their counts.

Another limitation concerns the resolution of the lowest classes. The SPC sorts particles into 64 classes of representative diameter from 36 to 490 µm, with an approximately constant width of about 7 µm. So, a single class spans a much larger fraction of the particle diameter at small sizes, meaning the relative resolution degrades towards low sizes.

Additionally, near the detection threshold the signal is weak: Schmidt (1982) reports that above an effective diameter of 100 µm the class limits are accurate to within 10 µm, but that the accuracy at smaller sizes is lower, and the instrument is insensitive to particles smaller than about 40 µm (Schmidt et al., 1977).

1.2.3 FlowCapt

The FlowCapt FC4 is a fourth-generation acoustic blowing snow sensor widely used in studies on drifting and blowing snow (. Amory et al., 2015). It consists of a 1 m cylindrical tube: particles impacting the tube generate acoustic pressure waves proportional to the local mass flux. The output is an integrated horizontal blowing snow mass flux over its height, in $\mathrm{kg\,m^{-2}\,s^{-1}}$.

The FlowCapt is a robust detector of aeolian snow transport above about $1\,\mathrm{g\,m^{-2}\,s^{-1}}$, but close to its detection limit of $10^{-3}\ \mathrm{g\,m^{-2}\,s^{-1}}$ it becomes unreliable (Trouvilliez et al., 2015). It also tends to underestimate the transported mass relative to the SPC: although the FC4 model used here is a more recent generation, Lehning et al. (2002) find that the first-generation FlowCapt consistently gives about 35 % of their mechanically measured fluxes, and Trouvilliez et al. (2015) report the second-generation sensor recording four to six times less than the SPC-S7 over a season.

1.2.4 Ceilometer

A Vaisala CL31 ceilometer is mounted on the roof of the station. The instrument is an elastic-backscatter lidar, which sends short near-infrared pulses (910 nm) upward and measures the light that atmospheric particles scatter back towards the receiver. Distance from the scatterers is calculated from the measured delay between emission of a pulse and its return, since the speed of light is known. Because particles are present at every level, a return signal is recorded at all ranges. The result is a backscatter signal as a function of height, which yields a full vertical

profile. At each level the strength of this signal increases with the number and size of the particles in the sampled volume, which is what makes the ceilometer sensitive to blowing snow. The CL31 reports a profile every 16 s, from 10 m up to about 7700 m above the instrument, with a vertical resolution of 10 m.

While ceilometers are conventionally used to retrieve cloud-base height, here the backscatter profile is exploited to detect drifting and blowing snow, since a layer of suspended snow increases backscatter values in the lowest ranges. The algorithm used to do so is described in Section 2.2. It returns the occurrence of blowing snow, the height of the top of the blowing snow layer, and the conditions under which it was detected (clear sky, or with cloud or precipitation). These outputs are used both to characterise blowing snow at PEA (Section 3.4) and as the reference against which the vertical extent of blowing snow in CRYOWRF is validated (Section 3.5.3).

Some limitations of these measurements should be noted:

i Absolute calibration: the CL31 reports range-corrected, internally calibrated attenuated backscatter, but no absolute calibration was applied, and the instrument-related background signal was not removed. The absolute magnitude of the backscatter reported here should therefore not be compared with values from other studies. Such a comparison would require an absolute calibration of the instrument, for instance the one proposed by O'Connor et al. (2004), as recommended by Kotthaus et al. (2016). This is not as relevant to this study, since the detection does not rely on the absolute backscatter values. In fact, it relies on the comparison of the measured profiles with a clear-sky reference profile derived from the same instrument, and on the shape of the profile.

ii Lowest range gates: below 70 m (with respect to the instrument's height) the overlap between the transmitter and receiver fields of view is incomplete, so the near-surface backscatter is underestimated. An internal correction is applied by the instrument, but it is derived under ideal conditions. In addition, when an obstruction is detected (e.g. ice on the window), the instrument automatically lowers the values at the lowest gates (Kotthaus et al., 2016). The signal in this part of the profile is therefore noisy, which the algorithm explicitly addresses (Section 2.2). For these reasons, values below 70 m are to be treated with caution.

iii Clouds and precipitation: in the presence of clouds or precipitation, the signal is strongly attenuated in the lowest gates, so that little of it reaches the upper part of the profile, which becomes then less accurate. In the most intense cases the returned signal above the near-surface layer is too weak to be interpreted,

and the profile can no longer be used to locate the top of the blowing snow layer at all. Such periods are identified by the detection algorithm through a fixed threshold on the lowest-gate backscatter, and are treated as a separate class (Section 2.2).

iv Ambiguity between blowing snow and overlying cloud or precipitation: when blowing snow occurs together with clouds or precipitation it is not possible to distinguish whether the signal originates from cloud alone or whether precipitation is also occurring. Moreover, in these conditions the boundary between the blowing snow layer and the cloud is harder to define.

v Height reference: the ceilometer is mounted on the roof of the station, about 15 m above ground level, and the heights it reports are relative to the instrument. The heights we report already account for this, and are referred to the ground level as set by the other instruments.

1.2.5 Micro Rain Radar

The Micro Rain Radar (MRR) is a vertically pointing frequency-modulated continuous-wave (FM-CW) Doppler radar operating at 24.1 GHz (K-band). It was originally designed to retrieve rain rate and drop size distribution from the Doppler spectrum of falling precipitation (Klugmann et al., 1996). Its standard processing assumes liquid hydrometeors and does not hold for snow. The data used here are therefore processed with IMProToo (Maahn et al., 2012), developed following the adaptation of the instrument to snowfall by Kneifel et al. (2011), which improves noise removal and returns equivalent reflectivity together with a signal-to-noise ratio (SNR) for each retrieval, a negative SNR indicating that the values are dominated by noise. The MRR is used in this work only to detect the occurrence of precipitation.

The MRR, in its vertical configuration, cannot detect blowing snow, for two reasons. First, since reflectivity scales with the sixth power of particle diameter, small particles return a very weak signal, and the instrument is essentially blind to those smaller than about 0.25 mm (Peters et al., 2005). This is well above the size of blowing snow particles, which in our SPC measurements (at about 50 cm above surface) have a median radius of around 100 µm. Second, being vertically pointing, the MRR measures only the vertical component of particle velocity, which for drifting and blowing snow is small.

Chapter 2

Methods

2.1 Meteorological clustering

A meteorological classification was performed following Gorodetskaya et al. (2013), who identify three regimes at PEA by unsupervised clustering of five near-surface variables. The cold katabatic regime is the background state of the site: under clear skies, radiative cooling of the surface builds a near-surface temperature inversion, the air is cold and dry, incoming longwave radiation is low, and the wind is the drainage flow. This flow descends the slope under gravity and is deflected to the left by the Coriolis force in the Southern Hemisphere, reaching the station from the south-east. At PEA, this flow is partly sheltered by the Sør Rondane Mountains. The warm synoptic regime is driven by the approach of cyclones from the coast: the air is warmer and moister, the sky is cloudy and incoming longwave radiation correspondingly high, the wind is stronger and turns to a more easterly direction, and the surface inversion is largely mixed away. It is the regime associated with snowfall and accumulation at the station. The transitional synoptic regime lies between the two, and represents developing or decaying synoptic conditions. The five cluster variables are chosen to capture this contrast. Near-surface temperature inversion is the signature of the katabatic flow. Incoming longwave radiation and specific humidity track cloudiness and air-mass origin. Wind speed separates the (typically) weaker drainage flow from cyclonic advection. Finally, surface pressure is a proxy for the large-scale forcing, with low pressure signalling the approach of a cyclone.

Near-surface temperature inversion is computed as the vertical temperature gradient between the air-temperature sensor and the snow surface. Because the surface level changes throughout the season as snow accumulates or erodes, the

height of the instrument above the snow surface is derived from the acoustic snow-height sensor, which measures the distance from the snow surface. Note that the instruments' heights vary from year to year (Table 1.1). The surface temperature T_{surf} is retrieved from the outgoing longwave radiation using the Stefan-Boltzmann law, treating snow as a grey body of emissivity $\varepsilon = 0.99$:

$$T_{\text{surf}} = \left[\frac{LW_{\text{out}} - (1-\varepsilon) LW_{\text{in}}}{\varepsilon \sigma} \right]^{1/4} \tag{2.1}$$

where $\sigma = 5.67 \times 10^{-8}\ \text{W m}^{-2}\,\text{K}^{-4}$ is the Stefan-Boltzmann constant and LW_{in} and LW_{out} are the measured downwelling and upwelling longwave fluxes (Gorodetskaya et al., 2013).

The same methodology as the reference paper is followed here, with the difference that we use hourly resolution rather than daily. The higher resolution allows a more detailed characterisation of blowing snow events, which are often shorter than a day. At hourly resolution, the diurnal cycle must also be removed, so detrending is done in three steps. First, we build a smooth seasonal baseline for each variable: we take the average value for each day of the year (over all years) and smooth it with a circular 30-day rolling mean (Figure A.1). Second, we compute the average daily cycle: for each hour, we measure how much it differs from its own daily mean, and then average these differences by month and hour of day (Figure A.2). Finally, we sum the seasonal and daily baselines and subtract them from the data, to obtain the anomalies used for clustering.

Then, detrended variables are standardised as z-scores:

$$z = \frac{x - \bar{x}}{\sigma_x} \tag{2.2}$$

where x is the hourly value of the cluster variable, $\bar{x}$ and σ_x are the average and standard deviation of the period over which the clustering is run, calculated from hourly values.

Unsupervised clustering is then applied. To compute the distance between data points, we use the Euclidean measure. Ward's hierarchical method (Smoliński et al., 2002) is used for clustering, which minimises the within-cluster variance at each merging step.

The number of clusters is set to $k = 3$ following Gorodetskaya et al. (2013). After clustering, the three groups are labelled by ranking them in decreasing order of mean temperature inversion: the group with the strongest inversion is designated

cold katabatic, the one with the weakest warm synoptic, and the intermediate group transitional synoptic.

This first clustering is run over the whole three-year record (2023–2025), so that it captures the site's mean meteorological regimes and their climatological frequencies of occurrence.

Intense transport hours are extreme with respect to the climatology on which this classification is built, and tend to be absorbed into the warm synoptic class independently of their origin (Section 3.2.2). For this reason a second clustering was run, following the same procedure, only on those hours during which drifting or blowing snow was recorded. This clustering is referred to as the transport-based clustering. Being built from the transport events themselves, it separates them into distinct groups even when the wind is strong. The two classifications are used for different purposes: the three-year climatological one for the mean regimes and their frequencies of occurrence, and the transport-based one for the characterisation of the transport events (Section 3.4).

2.2 The ceilometer's blowing snow detection algorithm

Blowing snow events are detected from the CL31 attenuated backscatter profiles using a modified version of the algorithm of Loeb et al. (2021), which was built on the one of Gossart et al. (2017). For each period the algorithm uses the shape of the backscatter profile and a set of near-surface meteorological thresholds to detect whether blowing snow is present, assigns the period to a category, and, when blowing snow is detected, estimates the height of the top of the layer. The same logical structure of the original algorithm is preserved, the changes made here concern the handling of missing values and of the time alignment between the ceilometer and the meteorological data, and add a criterion to determine the top of the blowing snow layer. This last change specifically makes the estimate of the cloud top more robust to noise in the profile, and will be detailed later in this section.

Before passing through the actual algorithm, the profiles are pre-processed by setting negative backscatter values to NaN, and by averaging the profiles to a 5-minute resolution. Detection relies on the shape of the profile and on its comparison with a clear-sky reference. The clear-sky reference is built from a set of clear-sky days selected from the meteorology. A day is considered as clear and calm if it has: downwelling shortwave radiation with a daily peak above $200\,\mathrm{W\,m^{-2}}$ and a 15-minute rolling coefficient of variation over the daytime hours below 0.05 for at

least 60% of the time, as well as a 2 m wind speed below 6 $\mathrm{m\,s^{-1}}$. The shortwave radiation criterion rejects days with passing clouds, the wind criterion excludes blowing snow. This yields 213 clear-sky, calm days over 2024–2025. The reference is computed gate by gate as a fixed percentile of the resulting backscatter distribution. This methodology for the selection of clear sky days differs from the one used by Gossart et al. (2017), which selected these days manually from the backscatter profiles. To be coherent with the profile obtained by them, here the percentile is chosen so that the reference at the lowest usable gate equals $21 \times 10^{-5}\,\mathrm{km^{-1}\,sr^{-1}}$, which is the near-surface threshold reported in their work for the CL-31 at Princess Elisabeth. On the present dataset this corresponds to the 96.8th percentile (Gossart et al. (2017) uses the 99th).

The algorithm is mainly divided in two phases: for each 5-minute period it first decides whether blowing snow is present, and if so, it moves upwards through the profile to classify the event and estimate the top of the layer. The detection stage is based on these criteria: i) the backscatter at the lowest usable gate exceeds the mean of the five gates above it; ii) the backscatter at that gate exceeds the clear-sky reference; iii) the 2 m wind speed is above 3 $\mathrm{m\,s^{-1}}$; iv) and the 2 m relative humidity is below a fog threshold of 90%.

When all these criteria are met, the algorithm moves upwards through the profile from the lowest usable gate to find the top of the blowing snow layer and assign the category. The period is labelled clear-sky blowing snow (category 1) if the ascent stops because the backscatter signal is lower than the clear-sky reference, or blowing snow with clouds or precipitation (category 2) if it stops because the signal increases higher up (Section 1.2.4, iv). These labels are overridden to an intense mixed event (category 3) whenever the backscatter at the lowest usable gate exceeds the category-3 threshold, with no distinction on the profile shape. If instead all the detection criteria are met except the one on humidity, meaning the humidity exceeds its threshold, the period is classified as fog (category 4); when blowing snow is not detected at all, it is assigned to category 0. The height of the detected top and the category are recorded for every period.

This stopping rule (for category 2), however, is very sensitive to the noise in the profile and to updrafts, local upward air motions that lift snow particles within the blowing snow layer. Both can lead to an underestimation of the height of the blowing snow layer and to a consequent misclassification of the period. In our cold katabatic event, for example, some noise led the original version of the algorithm to stop the ascent early, assigning a low cloud top and categorising several periods as blowing snow with clouds or precipitation, although that day was cloud-free, as confirmed by the surface weather station data. Retrieving this height reliably is important to the present work, since it is the quantity against which the height of

the blowing snow layer simulated by CRYOWRF is validated (Section 3.5.3). To make the retrieval more robust to these effects, the rule that ends the ascent on a single re-increase of the signal is modified, while the rest of the procedure is left unchanged.

Starting from the lowest usable gate, the algorithm moves upward one gate at a time and keeps track of the lowest backscatter value encountered so far, $b_{\min}$, and of the gate at which it occurred; the ascent stops when one of three criteria is met:

- Criterion a - clear-sky (unchanged from the original algorithm): the backscatter at the current gate, and at the one after, is lower than the clear-sky reference. The top is placed at the current gate and the period is labelled clear-sky blowing snow (category 1).
- Criterion b - global peak (the modification): in the original algorithm the ascent stopped at the first gate that was no longer strictly decreasing. The ascent is now allowed to tolerate small rises, and stops only when the backscatter has risen by more than a chosen percent threshold f above the current minimum, $b_{idx} > (1 + f)\, b_{\min}$. This identifies a sustained re-increase, like those produced by a cloud or precipitation, and the period is labelled blowing snow with clouds or precipitation (category 2).

When criterion b stops the ascent, the top is placed not at the gate where the re-increase is detected, but at the gate where the profile stopped decreasing. This global criterion is able to capture gradual, sustained re-increases that an only local comparison would miss. The single-bin noise check of the original algorithm, which ignores a single noisy gate among the lowest ten gates (about 100 m) and resumes the ascent, is also retained (Section 1.2.4, ii).

Criterion b uses a relative threshold, rather than an absolute one, because the backscatter at the lowest usable gate varies by more than an order of magnitude between events.The jump factor is set to $f = 0.25$ by parameter tuning against an independent reference for cloud and precipitation, detailed in Section 3.3.

Independently of the ascent, a period is flagged as an intense mixed event (category 3) whenever the backscatter at the lowest usable gate exceeds a fixed threshold, overriding the category assigned by the ascent. In these conditions the profile can no longer be used to reliably locate the top of the layer (Section 1.2.4, iii). Following Gossart et al. (2017) and Gorodetskaya et al. (2015), these events are treated as a separate class, flagging them when the lowest-gate backscatter exceeds $10000 \times 10^{-5}\,\mathrm{km^{-1}\,sr^{-1}}$.

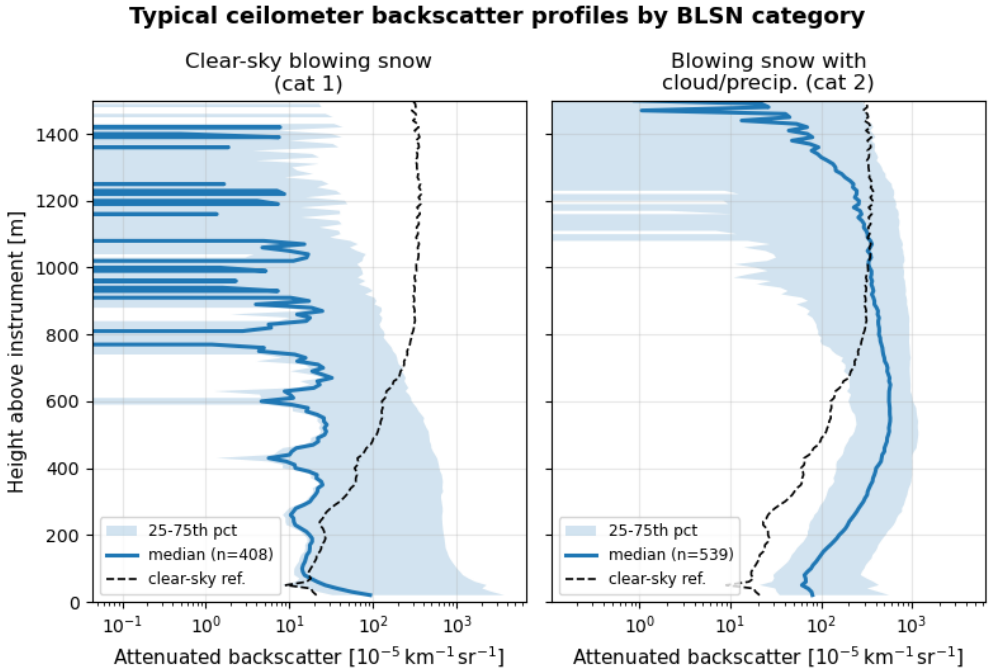


Figure 2.1: Typical ceilometer backscatter profiles for the two blowing-snow categories detected by the algorithm (Sect. 2.2): clear-sky blowing snow (cat 1, left) and blowing snow with cloud or precipitation (cat 2, right). For each category the solid line is the median profile over a sample of detected 5-minute periods, the shaded band the 25–75th percentile range, and the dashed line the clear-sky reference profile. Heights are given above the instrument. Notice the peak in backscatter in category 2, which represents clouds, or clouds and precipitation.

2.3 Statistical analysis: definition of DS and BS events

Drifting and blowing snow, and the boundary between the two, can have different definitions depending on the field. In this statistical analysis, for simplicity, a definition based on which instruments record transport is used. Surface transport is considered to occur when the SPC flux exceeds $10^{-2}\,\mathrm{g\,m^{-2}\,s^{-1}}$ or the FlowCapt flux exceeds $1\,\mathrm{g\,m^{-2}\,s^{-1}}$. These two thresholds reflect the reliability range of each instrument, the SPC being reliable down to very low fluxes (Section 1.2.2), and the FlowCapt only above about $1\,\mathrm{g\,m^{-2}\,s^{-1}}$ (Section 1.2.3). Suspended snow is considered to occur when the ceilometer detection algorithm of Section 2.2 identifies a blowing snow cloud. Instruments' records are averaged in 5 min steps, a resolution chosen to be consistent with the ceilometer's algorithm.

A step is classified as drifting snow (DS) when the surface sensors record transport but the ceilometer does not, meaning that snow is not transported high enough to be seen by the ceilometer. When the surface sensors and the ceilometer both observe snow transport, the step is classified as blowing snow (BS). There is also the possibility of a ceilometer signal of snow transport with no measurable surface flux. This is found to occur on average under light winds (median $\approx 5\,\mathrm{m\,s^{-1}}$), at cold temperatures (median $\approx -19\,^{\circ}\mathrm{C}$), and at humidities close to saturation with respect to ice, and is likely ice fog. Concurrent precipitation is identified from the MRR, when it has an SNR above 0 dB over at least three consecutive range gates for a minimum of 10 min.

It should be noted that, because drifting snow has no sharp onset or end, but it weakens gradually as the wind drops, the frequency of the DS class depends on the exact surface threshold. Lowering the SPC cut by one order of magnitude, from 10^{-2} to $10^{-3}\,\mathrm{g\,m^{-2}\,s^{-1}}$, raises the DS frequency from about 14 % to 18 % of the record. Instead, the BS class, which additionally requires the ceilometer's detection, is insensitive to this choice, since its events lie well above any of these thresholds.

Each event step is finally associated with the hourly meteorological regime, and the two clusterings of Section 2.1 are used. The regime frequencies of occurrence are taken from the three-year climatological clustering. The characterisation of the transport events is instead based on the transport-based clustering. For each regime and category we report the frequency of occurrence, the near-surface mass flux from the SPC and the FlowCapt, and the ceilometer cloud-top height.

2.4 Simulations with CRYOWRF

Simulations of selected events are run using the CRYOWRF model, developed by the WSL Snow and Avalanche Research Centre (SLF) and the EPFL Laboratory of Cryospheric Sciences (CRYOS), which couples the atmospheric Weather Research and Forecasting (WRF) model with the surface model SNOWPACK. Specifically, CRYOWRF v1.2.3 is used, a later version of the model first presented in Sharma et al. (2023) (v1.0). WRF, a widely used state-of-the-art model, provides the dynamical core. Its Advanced Research WRF (ARW) version (Skamarock et al., 2019) solves the fully compressible, Eulerian non-hydrostatic equations for the three velocity components, in Cartesian coordinates in the horizontal, and hybrid sigma pressure coordinates in the vertical. SNOWPACK (Bartelt et al., 2002; M. Lehning et al., 2002a; M. Lehning et al., 2002b) is a one-dimensional model that represents the snowpack at each grid point as a multi-layer column. It solves the heat equation, together with snow compaction and water percolation. Additionally, CRYOWRF implements a blowing snow scheme to represent the aeolian transport

of snow particles, their sublimation and redeposition.

2.4.1 The blowing snow scheme in CRYOWRF

Saltation begins when high wind speeds cause a sufficiently high shear stress at the snow surface to dislodge snow grains and entrain them into the air. In the model, this is represented by the condition that friction velocity exceeds a threshold, computed from the snow microstructure simulated by SNOWPACK:

$$u_{*,t} = \sqrt{\frac{A_t \rho_{\text{ice}} g r_g (SP + 1) + B_t \sigma_{\text{ref}} \dfrac{N_3 r_b^2}{r_g^2}}{\rho_{\text{air}}}} \tag{2.3}$$

where A_t, B_t are geometrical parameters; SP is the sphericity of the snow grains; N_3 is the coordination number of the snow grains; σ_{ref} is the reference shear strength; r_g is the grain radius; and r_b is the bond size between grains. The first term in the numerator of this equation represents the gravitational contribution, the second the cohesion between grains. In drifting and blowing snow, there are two modes of transport of snow particles: saltation, where particles are transported along the surface in ballistic trajectories, and suspension, where particles are picked up by turbulent eddies and transported at much greater heights and over much greater horizontal distances (Sharma et al., 2023). Explicitly resolving the saltation layer would require unattainable vertical resolution near the surface. For this reason, the saltation layer in CRYOWRF is parameterised. The saltation scheme used for the simulations in this study is Sørensen. This uses an empirical expression to compute the mass flux in saltation, which was originally developed for sand (Sørensen, 1991), and was later adapted to snow by Vionnet et al. (2014). Saltation acts as a lower boundary condition for the suspension layer, whose modelling constitutes the actual blowing snow model. This model consists of a double-moment scheme, solving Eulerian advection-diffusion-type equations for the mass and number mixing ratios of blowing snow particles, with additional terms for sedimentation and phase change. The prognostic advection-diffusion equation for the blowing snow mass mixing ratio q_{bs}, in Einstein notation, is:

$$\frac{\partial q_{bs}}{\partial t} + u_i \frac{\partial q_{bs}}{\partial x_i} = -K_{bs} \frac{\partial^2 q_{bs}}{\partial x_i^2} \delta_{i3} + \frac{\partial}{\partial x_i} \left(q_{bs} V_q \delta_{i3} \right) + S_q, \tag{2.4}$$

where u_i are the wind components, K_{bs} is the turbulent diffusion coefficient for blowing snow particles, V_q is the mass-weighted terminal fall velocity, and S_q is a sink (source) term accounting for sublimation (deposition) (Sharma et al., 2023). The mass of blowing snow has a single source, the saltation flux entering at the

lower boundary (q_{bs}), which is set at the top of the saltation layer. This mass is redistributed above the saltation layer, by advection, turbulent diffusion, and sedimentation, and reduced by sublimation. Precipitation is treated as a separate hydrometeor category in the atmospheric microphysics, and does not feed q_{bs}. The computation is analogous for the number mixing ratio N_{bs}. Being double-moment, the scheme can represent the evolution of the particle size in space and time.

The mean particle diameter at the saltation boundary is prescribed, to 140 µm in the configuration used in this work. To resolve the large near-surface gradients, a fine mesh is added below WRF's first layer. In this way, the scheme represents the interface between the atmosphere, computed by WRF, and the snow surface, given by SNOWPACK, enabling two-way communication between them: friction velocity from WRF triggers transport of surface snow, and the blowing snow, in turn, exchanges mass, moisture and the associated latent heat with the atmosphere. The version used here (CRYOWRF v1.2.3) follows Sigmund et al. (2025) and places these near-surface levels lower and more closely spaced than the original model, where the fine mesh was equally spaced above 0.5 m (Sharma et al., 2023).

2.4.2 Selection of events

To validate CRYOWRF under each meteorological regime, one drifting and blowing snow event per regime was selected: a Cold Katabatic event on 13–14 May 2024, a Transitional Synoptic event on 23–24 April 2025, and a Warm Synoptic event on 24–25 April 2025. The exact simulation windows are shown in Table 2.1. The selection followed three criteria: the meteorological conditions of the event had to be representative of the mean conditions of its regime; the event had to constitute an intense blowing snow event (high mass fluxes and tall blowing snow clouds); and all three instruments had to be recording for most of its duration.

Event	Start	End
Cold katabatic	2024-05-13 01:00	2024-05-14 14:00
Transitional synoptic	2025-04-23 05:00	2025-04-24 00:00
Warm synoptic	2025-04-24 12:00	2025-04-25 12:00

Table 2.1: Simulation windows for the three selected events.

Mean values of meteorological variables for each event are reported in Table 2.2. The Cold Katabatic event is cold, dry and cloud-free; the Transitional Synoptic event is milder, more humid and intermittently cloudy; the Warm Synoptic event is the warmest and most humid, overcast and accompanied by precipitation. They therefore fall close to the centroid of their own regime.

Table 2.2: Mean values of meteorological variables over each selected event. P is surface pressure, T_a air temperature, ΔT_{inv} the near-surface temperature inversion, q specific humidity, $\text{LW}_{\downarrow}$ incoming longwave radiation, WS wind speed and WD wind direction.

Variable	Cold Katabatic	Transitional Syn.	Warm Synoptic
P (kPa)	83.3	81.6	82.2
T_a (°C)	−21.6	−15.4	−14.8
ΔT_{inv} (°C)	1.7	1.5	1.2
q (g kg^{-1})	0.4	0.9	1.0
$\text{LW}_{\downarrow}$ (W m^{-2})	135	187	215
WS (m s^{-1})	12.7	11.2	11.1
WD (°)	142	111	98

2.4.3 Model setup

CRYOWRF is set up with a vertical grid of 97 layers on terrain-following pressure coordinates, extending up to 50 hPa. We use a total of five domains. The first has a horizontal resolution of 27 km, and a total grid size of 3240 km by 3240 km. The following domains have a resolution of 9 km, 3 km, 1 km and 200 m, respectively. The first domain has a spin-up time of 4 days. The nested domains have initial and boundary conditions given by the parent, and a spin-up time of 3 hours before the period of interest. Initial snowpack conditions were obtained from a separate 30 year spin-up SNOWPACK simulation at continental scale (27 km resolution), then interpolated to the model domain via nearest-neighbour. The model time step is 90 s on the parent domain, and about 0.67 s for the smallest nested domain. For the physics, we use the Morrison two-moments scheme for microphysics, MYNN 2.5 for the planetary boundary layer (with MYNN surface-layer scheme), and RRTMG for both shortwave and longwave radiation. The snow cover is handled by the SNOWPACK land-surface scheme, and the blowing snow module, with sublimation, is active on all domains. Grid nudging is applied to the first domain every six hours. The projection is polar stereographic. The boundary conditions and the input for the first time step are extracted from ERA-5 reanalysis.

2.4.4 Validation against the observations

CRYOWRF is validated at PEA over the three simulated events (Table 2.1), against the surface AWS, the two near-surface blowing snow instruments (the Snow Particle Counter and the FlowCapt), and the ceilometer. All comparisons use the innermost domain (d05, 200 m horizontal resolution), and every model field is extracted at the station by bilinear interpolation of the four surrounding grid points to PEA's coordinates. The location is different for the ceilometer, which is positioned on the

roof of the station, while the SFC AWS is approximately 100 m away. Each hourly model output is then paired with the corresponding observation, averaged over a 10 min window (±5 min) centred on the output time. Note that the surface sensor heights differ from one event to the other, following the change in snow surface height (Table 1.1).

Atmospheric variables

The near-surface atmospheric variables are compared at the height of the corresponding sensor. Surface pressure is taken directly from the model surface pressure field (`PSFC`). Potential temperature and relative humidity (with respect to water) are the 2 m diagnostics. Wind direction is the WRF 10 m diagnostic. Wind speed is not taken from the 10 m diagnostic, but from the CRYOWRF fine mesh. Among its levels, whose heights are given by `SN_C_HEIGHT`, the one closest to the lower Young anemometer (about 1.75 m) is selected, and the fine-mesh wind speed `VW_SFC` at that level is used. These fields are compared with the surface pressure, potential temperature, relative humidity, wind speed (lower anemometer) and wind direction recorded by the AWS.

Blowing snow mass flux

The model produces a vertical profile of the horizontal blowing snow flux, $q(z)$ (`BS_QI_DRIFT`), on CRYOWRF's fine mesh, below WRF's first level. The profile is bilinearly interpolated to PEA at each of these levels.

The FlowCapt reaches below the lowest fine mesh height, so the profile is first extended using the saltation boundary condition. In CRYOWRF the saltation layer is treated with the Sørensen parameterisation (Sharma et al., 2023), and its output is the vertically integrated saltation mass flux Q_{salt} (`SNOW_DRIFT`), in $\mathrm{kg\,m^{-2}\,s^{-1}}$. As implemented in the model code, the saltation flux density at height z is the product of a mass concentration and the particle velocity, $q(z) = c_{\mathrm{salt}}(z)\, u_{\mathrm{part}}$, with

$$c_{\mathrm{salt}}(z) = \frac{Q_{\mathrm{salt}}}{u_{\mathrm{part}}}\, \alpha\, e^{-\alpha z}, \qquad \alpha = \max\!\left(\frac{\lambda\, g}{u_*^2},\ \frac{1}{0.04}\right). \tag{2.5}$$

In this equation, u_* is the friction velocity (`UST`), $\lambda = 0.45$, and α is the inverse decay length of the layer (Melo et al., 2024). At the top of the saltation layer, $z = H_{\mathrm{salt}} = 0.15\,\mathrm{m}$. This yields

$$q_{\mathrm{salt}}(H_{\mathrm{salt}}) \;=\; c_{\mathrm{salt}}(H_{\mathrm{salt}})\, u_{\mathrm{part}} \;=\; Q_{\mathrm{salt}}\, \alpha\, e^{-\alpha H_{\mathrm{salt}}}. \tag{2.6}$$

Dimensionally $Q_{\mathrm{salt}}\,[\mathrm{kg\,m^{-1}\,s^{-1}}] \times \alpha\,[\mathrm{m^{-1}}] = [\mathrm{kg\,m^{-2}\,s^{-1}}]$, the same units as the blowing snow flux profile, so q_{salt} can be added to it at $z = H_{\mathrm{salt}}$.

Each instrument then samples this extended profile according to its geometry. The SPC is a point sensor at a fixed height z_{SPC}, so its model value is the drift flux linearly interpolated between the two adjacent levels at that height, $q(z_{\mathrm{SPC}})$. The FlowCapt is a tube that integrates the transported mass over its whole length (about 1 m, between z_{lo} and z_{hi}), so its model value is the profile integrated over the same interval by the trapezoidal rule, with both bounds linearly interpolated from the profile, and normalised by the tube length,

$$Q_{\mathrm{FC}} \;=\; \frac{1}{z_{\mathrm{hi}} - z_{\mathrm{lo}}} \int_{z_{\mathrm{lo}}}^{z_{\mathrm{hi}}} q(z)\,\mathrm{d}z. \tag{2.7}$$

This gives the mean horizontal mass-flux density over the instrument's height. This is directly comparable to the FlowCapt measurement. All fluxes are converted to $\mathrm{g\,m^{-2}\,s^{-1}}$.

In addition to the flux, the mean particle radius is compared at the SPC height. On the observation side, the SPC resolves the particle size distribution into diameter bins. The mean radius is obtained from the per-bin counts N_i and bin-centre diameters d_i (from about 36 to 490 µm) as

$$\bar{r} \;=\; \frac{\sum_i N_i\,(d_i/2)}{\sum_i N_i}, \tag{2.8}$$

in µm, and is set to NaN whenever the total count is zero. On the model side, the mean radius is taken from `SFC_MEANR`, the blowing-snow mean particle radius computed on the same eight drift levels as `BS_QI_DRIFT`: it is interpolated to PEA, linearly interpolated to the SPC height (as for the flux), and converted from metres to micrometres.

Blowing snow cloud top

The vertical dimension of blowing snow is validated through the height of the blowing snow layer. On the model side, the blowing snow mixing ratio `bs_qi` is interpolated to PEA at every level, and the cloud top is taken as the first height at which it falls below $10^{-6}\,\mathrm{kg\,kg^{-1}}$. This threshold constitutes the upper end of the range $10^{-8}\,\mathrm{kg\,kg^{-1}}$ to $10^{-6}\,\mathrm{kg\,kg^{-1}}$ used by Gerber et al. (2023) to define blowing snow occurrence in CRYOWRF, and it coincides with the value of $1\,\mathrm{mg\,kg^{-1}}$ used to locate cloud top from the total mixing ratio. The sensitivity of the retrieved height to this choice is assessed in Section 3.5.3. The modelled top is compared with the top of blowing snow layer estimated from the ceilometer, with the detection algorithm described in Section 2.2.

Chapter 3

Results

3.1 Meteorological conditions in 2024 and 2025

Princess Elisabeth station experiences distinctive meteorological conditions linked to its location on the East Antarctic escarpment, where a persistent katabatic background is repeatedly interrupted by synoptic disturbances (Section 2.1).

The overall picture of the mean meteorological conditions for 2024 and 2025 are similar to those found by (Gorodetskaya et al., 2013) for 2009 and 2010, as summarised in Table 3.1. Mean air temperature was −18.0 °C in 2024 and −18.6 °C in 2025. The hourly values spanned more than thirty degrees, from below −35 °C on clear, calm nights to temperatures approaching the melting point during strong storms. Wind blew predominantly from the east-south-east in both years, consistent with katabatic drainage channelled by the Sør Rondane Mountains and rotated by approaching low-pressure systems. During both years, the snow surface was lowered by snow erosion, by 3.3 cm in 2024, and 4 cm in 2025 (calculated with respect to the first measurement of the year with the acoustic sensor).

3.2 Results of the meteorological clustering

The clustering was run on the three years 2023—2025 together, rather than on each year separately. Clustering one year at a time makes the cluster boundaries adapt to the conditions of that year, and produces a warm synoptic regime whose frequency and mean conditions vary substantially from year to year, up to 29 % of the hours in 2025 against 10 % in 2024. The combined classification is more stable across years and closer to Gorodetskaya et al. (2013) in both frequency and mean cluster variables. The comparison between the two is given in Appendix A.2. The

Table 3.1: Annual mean conditions at PEA. 2009–2010: Gorodetskaya et al. (2013); 2024–2025: this study.

Year	Period	TA [°C]	q [g kg^{-1}]	P [hPa]	WS [m s^{-1}]	LW_{in} [W m^{-2}]
2009	02 Feb – 21 Nov	-19.0 ± 5.4	0.58 ± 0.37	827 ± 9	5.3 ± 3.4	171 ± 39
2010	12 Jan – 31 Dec	-19.5 ± 7.1	0.52 ± 0.51	824 ± 10	4.6 ± 2.6	158 ± 39
2024	01 Jan – 31 Dec	-18.0 ± 6.3	0.64 ± 0.46	830 ± 8	3.9 ± 3.3	175 ± 39
2025	08 Feb – 31 Dec	-18.6 ± 5.8	0.57 ± 0.38	826 ± 7	4.2 ± 3.0	170 ± 36

combined classification is used throughout this work.

3.2.1 The three regimes

The mean conditions of the three regimes are given in Table 3.2. The classification reproduces the expected structure, with the cold katabatic regime being the most frequent (59 % of the hours), and the warm synoptic the rarest (14 %). The two are opposite in every clustering variable, and the transitional synoptic regime is intermediate in each of them, so that the three are ordered monotonically with the synoptic forcing. The only exception to this ordering is surface pressure, which is highest rather than lowest in the warm synoptic regime. Pressure is not consistently ordered in Gorodetskaya et al. (2013) either (Table 3.2), where in 2010 they find a higher pressure in the cold katabatic regime, followed by the warm and finally by the transitional synoptic ones.

These values agree well with those reported by Gorodetskaya et al. (2013) (Table 3.2): incoming longwave radiation, wind speed and air temperature reproduce both the values and the pattern where the warm synoptic and cold katabatic clusters have opposite conditions, and the transitional synoptic lies in between. The wind directions are rotated by about 30° towards the east, possibly due to different instrument positioning. Still, the same pattern holds, where the wind has a more south-easterly direction in the cold regime and turns to the east as conditions become synoptic (Fig. 3.1).

The same clustering applied at daily resolution, as in Gorodetskaya et al. (2013), recovers the same three physical states, with regime means that change little, but it over-represents the transitional regime (44 % of days against 27 % of hours), likely because most regime episodes are shorter than a day. The hourly resolution is adopted here because it resolves the brief synoptic intrusions that a daily mean

averages out, and because it is closer to the duration of the transport events (Appendix A.3).

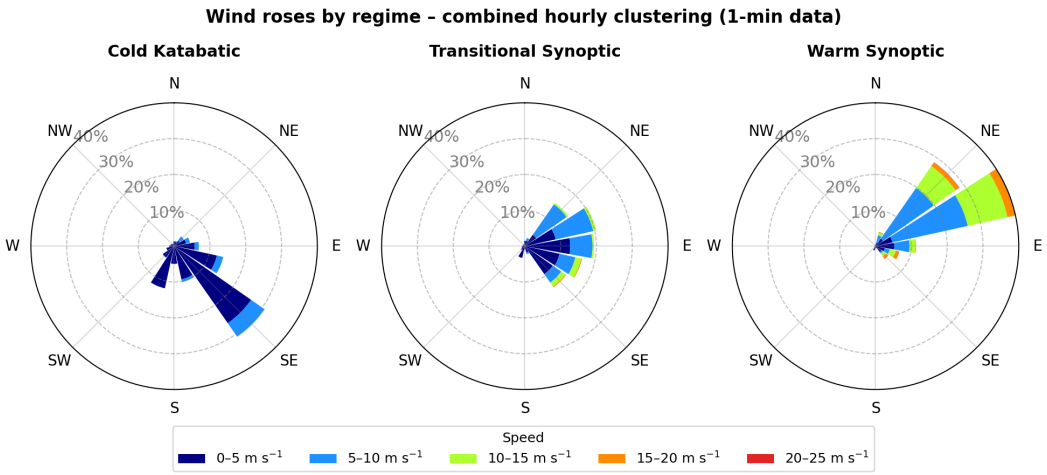


Figure 3.1: Wind roses for the three regimes (combined 2023–2025 hourly classification), from the 1-minute wind data of the hours in each regime. The height of each bar shows the fraction of time the wind came from a given direction, coloured by wind speed. Notice how the direction of the katabatic wind is south- southeast, and turns progressively more easterly as synoptic influence increases. The warm synoptic regime has the largest wind speeds.

3.2.2 Classification during transport events

The clustering classifies periods of intense snow transport with lower confidence: hours with FlowCapt mass flux greater than $100\,\mathrm{g\,m^{-2}\,s^{-1}}$ have a mean distance to their assigned centroid of 2.79, compared to 1.51 for the full dataset. These are extreme conditions with respect to the climatology on which the classification is built. As a result, both the Cold Katabatic and Transitional Synoptic blowing snow events selected to simulate with CRYOWRF (Sect. 2.4.2) are classified as warm synoptic during their peak transport hours. Wind speed is the main cause. During those hours the wind reaches 15.5 and $15.1\,\mathrm{m\,s^{-1}}$ respectively, far above the cold katabatic ($2.7\,\mathrm{m\,s^{-1}}$) and transitional ($4.8\,\mathrm{m\,s^{-1}}$) means, and well above the warm synoptic one ($8.2\,\mathrm{m\,s^{-1}}$). Strong wind is both a defining feature of the warm synoptic regime and a major driver of blowing snow, so its extreme values dominate the classification. The same wind mixes the surface inversion away, which falls to 1.14 and $0.81\,\mathrm{K\,m^{-1}}$, during the two events, close to the warm synoptic mean (0.8), and this pushes these hours further towards the warm class. This is the reason for the additional transport based clustering described in Section 2.1. Under that classification the peak transport of the three simulated events each fall

Table 3.2: Mean conditions of the three regimes. Gorodetskaya 2009/2010: daily clustering; combined (2023–2025): hourly clustering, this study.

Variable	Gorod. 2009 daily	Gorod. 2010 daily	Combined hourly
Cold Katabatic			
Freq [%]	52	59	59
TA [°C]	-21.0	-20.0	-19.2
q [g kg^{-1}]	0.30	0.40	0.45
P [hPa]	829	827	829
WS [m s^{-1}]	3.5	4.0	2.7
LW_{in} [W m^{-2}]	144	144	151
WD [°]	175	169	154
Transitional Synoptic			
Freq [%]	34	23	27
TA [°C]	-18.0	-21.0	-18.0
q [g kg^{-1}]	0.70	0.50	0.66
P [hPa]	827	818	825
WS [m s^{-1}]	5.5	5.0	4.8
LW_{in} [W m^{-2}]	189	157	195
WD [°]	141	147	104
Warm Synoptic			
Freq [%]	14	18	14
TA [°C]	-16.0	-16.0	-13.8
q [g kg^{-1}]	1.10	1.00	1.15
P [hPa]	824	825	832
WS [m s^{-1}]	12.0	7.0	8.2
LW_{in} [W m^{-2}]	228	207	225
WD [°]	95	113	80

in their expected regime.

3.3 Performance of the blowing snow detection algorithm

The jump factor f was set by comparing the category assigned by the algorithm with a reference for cloud and precipitation independent of the ceilometer, built

from the SFC AWS longwave radiation and from the MRR: precipitation is taken directly from the MRR, when it has an signal-to-noise ratio above 0 dB over at least three consecutive range gates for a minimum of 10 min; the cloud label is derived from the downwelling longwave radiation. Treating the sky as a grey body at near-surface air temperature, the Stefan–Boltzmann law (T_a, $LW_{\mathrm{down}} = \varepsilon_{\mathrm{sky}}\,\sigma T_a^4$, where σ is the Stefan–Boltzmann constant), gives the apparent sky emissivity. Its distribution is bimodal (clear sky $\varepsilon \approx 0.6$–0.7, overcast $\varepsilon \approx 1.0$). The clear/cloudy threshold is set on this bimodal distribution by Otsu's method (Otsu, 1979), which selects the value maximising the between class variance of the two modes, yielding $\varepsilon_{\mathrm{Otsu}} = 0.755$. A point is labelled cloudy when $\varepsilon > \varepsilon_{\mathrm{Otsu}}$.

The blowing snow detection algorithm was run for f from 0.10 to 0.40, and data was split 80/20 into a validation and a test set, grouped by day to avoid leakage. The category-1 versus category-2 decision is found to be largely insensitive to the choice, which mainly affects the retrieved top of a minority of profiles, so the initially selected value ($f = 0.25$) was kept. On the test set the decision reaches an F1 score of 0.93 and a balanced accuracy of 0.89 against the independent reference. The correct classification of the period goes along with an accurate estimate of the cloud top height, for which instead we have no ground truth. These scores therefore give confidence that the algorithm reliably estimates them.

The ceilometer categories provide an independent check on the meteorological classification, since they are derived from the backscatter profile alone and carry no information on the regime. The intense mixed events (cat 3), which Gossart et al. (2017) associate with storms, fall for 88 % in the warm synoptic regime (in the transport-based clustering) and never in the cold katabatic one, while cloudless blowing snow (cat 1) is found for 57 % in the cold katabatic regime, in agreement with their observation that clear-sky blowing snow occurs mostly under katabatic conditions. The two classifications therefore agree on which events belong to which regime, supporting the clustering, and the ceilometer algorithm's performance as well.

3.4 Statistical analysis

Over 2024 and 2025, some form of snow transport is present at the station 22 % of the time. Drifting snow seen only by the surface sensors (DS) is by far the most common, at 14.0 % of the time. BS, where the ceilometer also detects blowing snow, accounts for 7.8 %. The ceilometer-only class is rare, at 1.4 %. In this class, 78 % of the steps have a weak surface signal, but below the chosen thresholds for SPC and FlowCapt mass fluxes. The signal from the ceilometer in this class is consistently weak, with a median in-cloud backscatter about sixty times weaker

Table 3.3: Frequency, near-surface mass flux and ceilometer cloud-top height of the 5 min categories (clustering-independent, 2024–2025). Fluxes in $\mathrm{g\,m^{-2}\,s^{-1}}$, height in m.

		SPC		FlowCapt		Cloud top	
Category	Freq. [%]	med	mean	med	mean	med	mean
BS	7.8	20.11	74.9	3.00	17.9	210	299
DS	14.0	0.27	8.9	0.07	1.9	–	–
Ceilo-only	1.4	0.00	0.0	0.00	0.0	50	101
No event	76.7	0.00	0.0	0.00	0.0	–	–

than in the BS class and a cloud top at the lowest resolvable gate (65 m) in 77 % of the cases, under weak winds ($4.6\,\mathrm{m\,s^{-1}}$) and cold air. This points to fog, and this class is excluded from the DS and BS statistics.

The intensity of transport increases sharply from one class to the next (Table 3.3). The median SPC flux goes from $0.27\,\mathrm{g\,m^{-2}\,s^{-1}}$ in DS to $20.1\,\mathrm{g\,m^{-2}\,s^{-1}}$ in BS, almost two orders of magnitude, and the FlowCapt is systematically lower but follows the same order. BS also adds the vertical dimension, with a median cloud top of 210 m against the 50 m (the lowest height the algorithm can assign) of the ceilometer-only class. The classes also differ in the weather: BS occurs in the windiest ($10.9\,\mathrm{m\,s^{-1}}$), warmest (−18.0 °C) and most humid (80 %) conditions, DS at more moderate winds ($6.9\,\mathrm{m\,s^{-1}}$), and the no-event periods in the calmest, coldest and driest air ($3.2\,\mathrm{m\,s^{-1}}$, −20.0 °C, 47 %). Wind speed therefore increases with the intensity of the class.

Classified by the transport-based clustering, BS splits into 54 % Warm Synoptic, 23 % Transitional and 23 % Cold Katabatic, while DS is more evenly spread (32 %, 37 % and 32 %). Each regime seems to have its own transport mode (Table 3.4). Warm-synoptic BS is the most intense and by far the deepest, with the highest mean flux and a cloud top around 480 m, driven by the strong cyclonic forcing. Cold-katabatic BS is the opposite: intense at the surface (the highest medians, SPC 33 and FlowCapt $15\,\mathrm{g\,m^{-2}\,s^{-1}}$) but shallow, with a cloud top of only 80 m. Transitional BS is weaker at the surface and intermediate in depth. Drifting snow grows more regularly with the synoptic forcing, its median flux rising from $0.17\,\mathrm{g\,m^{-2}\,s^{-1}}$ to $0.20\,\mathrm{g\,m^{-2}\,s^{-1}}$ in the Cold and Transitional regimes to about $1.9\,\mathrm{g\,m^{-2}\,s^{-1}}$ (mean 24) in the Warm Synoptic.

Precipitation concurrent with transport, at least as observed by the MRR at the station, does not occur often, 4.8 % of the transport steps. It is confined almost entirely to the Warm Synoptic regime, coinciding with 15.3 % of the warm-synoptic BS steps and 9.8 % of the corresponding DS steps, and essentially never with

Table 3.4: BS near-surface mass flux and ceilometer cloud-top height by regime (transport-based clustering). Fluxes in $\mathrm{g\,m^{-2}\,s^{-1}}$, height in m.

	SPC		FlowCapt		Cloud top	
Regime (BS)	med	mean	med	mean	med	mean
Cold Katabatic	32.8	72.3	14.8	36.3	80	114
Transitional Synoptic	1.8	19.8	0.4	7.7	90	229
Warm Synoptic	26.0	99.4	2.9	14.3	480	409

the other regimes or the ceilometer-only class. When it occurs, it increases the transport considerably: warm-synoptic BS averages an SPC flux of 166 against $87\,\mathrm{g\,m^{-2}\,s^{-1}}$ with and without concurrent precipitation, roughly twice as much, and warm-synoptic DS rises from 18 to $83\,\mathrm{g\,m^{-2}\,s^{-1}}$, a nearly five-fold increase. In fact, fresh snow is easier to dislodge, and the falling particles themselves are measured together with blowing snow ones.

The two surface instruments are consistent during BS, when the fluxes are large and well above their detection limits. Pooled over all BS steps the Pearson correlation between the SPC and the FlowCapt flux is $r = 0.66$ (Spearman $\rho = 0.84$). The two instruments therefore track the same events reliably. Their absolute magnitudes, however, differ: the FlowCapt reads on average about a fifth of the SPC, in accordance with the analyses of (Trouvilliez et al., 2015) and Lehning et al. (2002) (Section 1.2.3). During DS the agreement is weaker ($r = 0.44$, $\rho = 0.69$), reflecting the noisier signal close to the detection threshold.

3.5 Validation of CRYOWRF

The CRYOWRF model is validated against the surface automatic weather station, the two blowing snow mass flux measuring instruments (FlowCapt and SPC), and the ceilometer, over the three simulated events, one per regime (Table 2.1). For each variable the mean absolute error (MAE) and the bias are reported, together with the Pearson correlation r, which measures how well the model reproduces the temporal evolution of the quantity. For the blowing-snow mass flux, the percent bias (PBIAS) is additionally reported.

The three events derive from distinct configurations of increasing synoptic influence, which were identified from simulation results. The Cold Katabatic event is an exceptionally strong katabatic event: a low pressure system to the east of the station enhanced and channeled the drainage flow through the Sør Rondane Mountains, allowing for unusually high wind speeds for this regime (Fig. B.1).

The Transitional Synoptic event was caused by a single cyclone approaching the coast. The Warm Synoptic event, finally, resulted from a Fujiwhara interaction (Fujiwhara, 1921) between that same cyclone and a second one that approached shortly after. The two systems rotated around each other, until one was eventually absorbed by the other (Fig. B.2). This brought precipitation at Princess Elisabeth during the Warm Synoptic event.

The surface mass flux peaked in the katabatic event (480 and 305 $\mathrm{g\,m^{-2}\,s^{-1}}$ at the SPC and FlowCapt), and was lower in the Transitional Synoptic (359/300) and Warm Synoptic (176/182 $\mathrm{g\,m^{-2}\,s^{-1}}$) events. The blowing snow cloud height, conversely, deepened with synoptic forcing, its mean top height rising from about 140 m in the katabatic event to 185 m and 350 m in the two synoptic ones. The ceilometer retrieval is least reliable for the Warm Synoptic event, where cloud and precipitation likely inflate the retrieved plume top (Section 1.2.4, iv), and most reliable for the Cold Katabatic event, which is cloud-free and for which the instrument recorded continuously.

3.5.1 Atmospheric variables

Accuracy of near-surface atmospheric variables changes considerably among the simulated events (Table 3.5). The best agreement is found for the Cold Katabatic event, it is intermediate for the Warm Synoptic event, and it is poorest for the Transitional Synoptic event.

Potential temperature is reproduced with an overall bias of −2.85 °C and MAE of 2.93 °C ($r = 0.88$ over the pooled sample). The model is systematically too cold in every event, and the near coincidence of MAE and |bias| (for example −5.10 °C and 5.10 °C in the Transitional event, −3.85 °C and 3.85 °C in the Warm one) shows that the error is almost entirely a constant offset rather than random scatter. The cold bias is smallest in the Cold Katabatic event (−1.32 °C) and largest in the Transitional one (−5.10 °C, with a much weaker correlation, $r = 0.24$).

Relative humidity (with respect to water) shows a marked dry bias, −13.3 % overall, which follows the same regime ordering: it is moderate in the Cold Katabatic event (−6.3 %, $r = 0.77$) and severe in the two synoptic events (−16.5 % in the Warm, −25.0 % in the Transitional), for which correlation even becomes slightly negative.

On the contrary, wind speed is overestimated, with an overall bias of $2.4\,\mathrm{m\,s^{-1}}$ (MAE $4.4\,\mathrm{m\,s^{-1}}$) and a low correlation ($r = 0.12$ over the pooled sample). The overestimation is largest in the Warm Synoptic event ($4.6\,\mathrm{m\,s^{-1}}$). The weak, and in the Transitional event negative ($r = -0.37$), correlation indicates that the model does not capture well wind fluctuations, but only their mean level. Wind direction

Table 3.5: Validation of the near-surface atmospheric variables against the SFC AWS, per event and pooled (overall). MAE and bias are in the units of each variable; r is the Pearson correlation. N is the number of observation-measurement pairs used for this comparison. The bias of wind direction is omitted because the variable is circular.

Variable	Event	N	MAE	Bias	r
Surface pressure [hPa]	Cold katabatic	45	5.92	−5.92	0.654
	Transitional	20	3.51	+3.51	0.665
	Warm synoptic	24	1.63	−0.20	0.954
	Overall	89	4.22	−2.26	0.918
Pot. temperature [°C]	Cold katabatic	45	1.47	−1.32	0.672
	Transitional	20	5.10	−5.10	0.243
	Warm synoptic	24	3.85	−3.85	0.612
	Overall	89	2.93	−2.85	0.878
Wind speed [$\mathrm{m\,s^{-1}}$]	Cold katabatic	45	4.14	+2.63	0.265
	Transitional	20	4.39	−0.87	−0.369
	Warm synoptic	24	4.77	+4.64	0.454
	Overall	89	4.37	+2.39	0.120
Wind direction [°]	Cold katabatic	45	17.19	—	0.220
	Transitional	20	10.64	—	0.254
	Warm synoptic	24	12.58	—	0.003
	Overall	89	14.48	—	0.788
Relative humidity [%]	Cold katabatic	45	9.84	−6.31	0.771
	Transitional	20	26.21	−24.98	−0.167
	Warm synoptic	24	19.88	−16.47	−0.239
	Overall	89	16.23	−13.25	0.421

also has low correlation in the single events, and null in the Warm Synoptic one. It is however consistent with the south-easterly to easterly rotation expected as conditions become synoptic.

Surface pressure is well captured in all three events, especially in the Warm one, which has a correlation of $r = 0.95$. Errors are within a few hPa (overall MAE 4.2 hPa), and largest in the Cold Katabatic case (bias of −5.9 hPa, against 3.51 hPa in the Transitional and −0.2 hPa in the Warm cases).

3.5.2 Blowing snow mass flux

The modelled mass flux is compared against the FlowCapt (FC) and SPC records at their respective heights (Table 3.6). For both instruments, the model reproduces the timing of transport well only in the Cold Katabatic event, and it systematically

Table 3.6: Validation of the blowing-snow mass flux and mean particle radius against the FlowCapt (FC) and SPC, per event. MAE and bias are in the units given in the first column; PBIAS is the percent bias (negative = underestimation) and applies to the fluxes only; N is the number of paired points and r the Pearson correlation.

Quantity	Event	N	MAE	Bias	PBIAS [%]	r
FC flux $[\mathrm{g\,m^{-2}\,s^{-1}}]$	Cold katabatic	38	48.03	−33.71	−46.2	0.527
	Transitional synoptic	20	25.57	−24.15	−95.2	−0.095
	Warm synoptic	24	13.61	−3.05	−20.8	0.282
SPC flux $[\mathrm{g\,m^{-2}\,s^{-1}}]$	Cold katabatic	38	99.02	−94.63	−76.6	0.463
	Transitional synoptic	20	34.76	−33.55	−96.8	−0.115
	Warm synoptic	24	22.90	−16.83	−60.4	0.179
SPC radius [µm]	Cold katabatic	38	37.6	−37.6	—	0.539
	Transitional synoptic	12	35.4	−35.4	—	−0.042
	Warm synoptic	24	27.4	−27.4	—	0.573

and strongly underestimates the flux in every event. The timeseries for the Cold Katabatic event of the two fluxes is shown in Figure 3.2, and for the other two in the Appendix (Figures B.4 and B.5).

The temporal agreement follows the same regime ordering as the atmospheric fields. In the Cold Katabatic event the model simulates the observed transport reasonably ($r = 0.53$ for FC and 0.46 for SPC). In the Warm Synoptic event the correlation drops ($r = 0.28$ and 0.18), and in the Transitional Synoptic event it collapses, becoming slightly negative ($r = -0.10$ and -0.12). In the last one, the model does not reproduce the observed transport at all, with just one point in time having a positive mass flux.

There is a systematic underestimation of the flux, which is large in every event. The bias is negative for both instruments throughout, and the underestimation, in terms of percent bias, is of −46 % (FC) and −77 % (SPC) in the Cold Katabatic event, −21 % (FC) and −60 % (SPC) in the Warm Synoptic event, and is almost total in the Transitional Synoptic event, with a percent bias of −95 % (FC) and −97 % (SPC). In absolute terms the underestimation is largest in the Cold Katabatic event, which also has the strongest observed fluxes (bias $-34\,\mathrm{g\,m^{-2}\,s^{-1}}$ for FC and $-95\,\mathrm{g\,m^{-2}\,s^{-1}}$ for SPC, with event-peak fluxes of 305 and $480\,\mathrm{g\,m^{-2}\,s^{-1}}$). The SPC shows a larger underestimation than the FlowCapt in every event, due to the fact that the FlowCapt reads systematically lower than the SPC (Section 1.2.3).

The SPC measures the particle size distribution, so the mean particle radius can be compared with the model's, over the timesteps with transport in both. Here

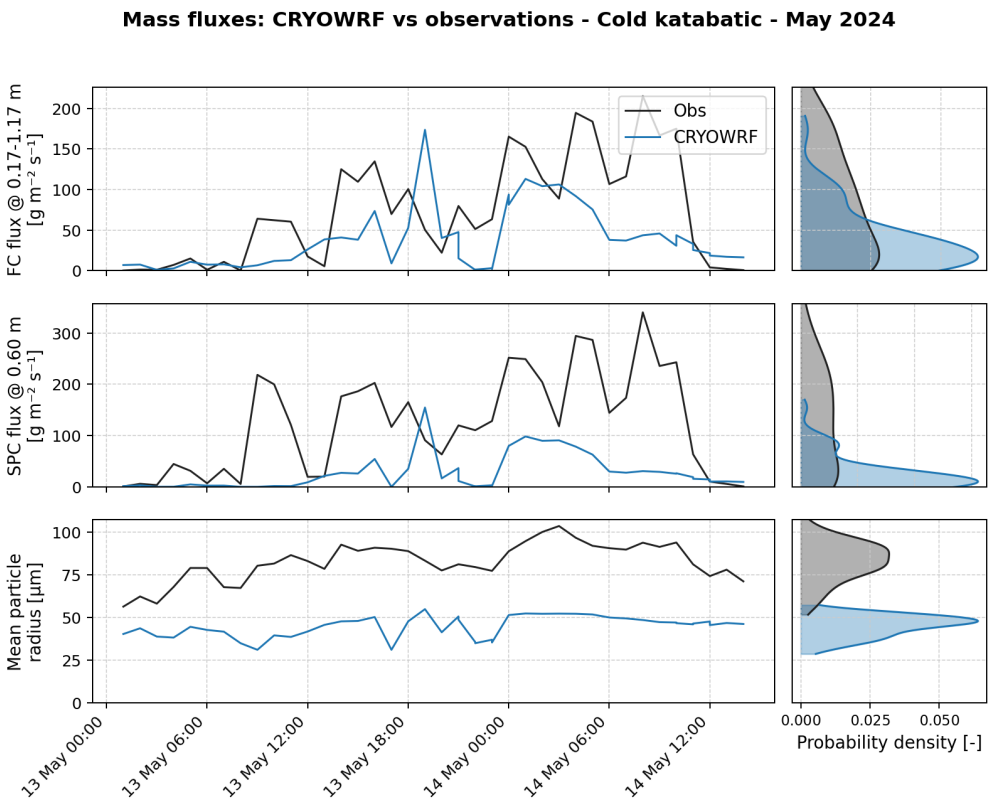


Figure 3.2: Timeseries of the FlowCapt and SPC simulated (domain 5) and measured mass fluxes and mean particle radius, with their probability densities, for the Cold Katabatic event.

too the model underestimates, at every paired timestep: the bias equals the mean absolute error in magnitude, so the modelled radius lies systematically below the observed one. The underestimation is about 34 µm overall (observed radii of roughly 60 µm to 90 µm against modelled 35 µm to 55 µm), with a moderate correlation ($r = 0.42$) that is higher within the Cold Katabatic and Warm Synoptic events ($r = 0.54$ and 0.57) than in the Transitional one, where it vanishes ($r = -0.04$, on only $N = 12$ points). The blowing-snow particles simulated by CRYOWRF are therefore systematically too small.

3.5.3 Blowing-snow cloud top

The validation has so far concerned the mass flux at the surface, and the ceilometer allows a comparison in the vertical dimension. Two aspects are compared. The first is the amount of snow in the column, quantified with different variables for the model and the instrument: the blowing snow mixing ratio, integrated over the

model column at PEA, is compared with the ceilometer backscatter integrated within the detected blowing snow layer. Being different quantities in different units, the two cannot be compared in absolute terms, but during the Cold Katabatic event they have a high Pearson correlation ($r = 0.67$), indicating that they co-vary closely in time. The second, and principal, comparison concerns the cloud-top height itself, defined as in Section 2.4.4 (Fig. 3.3).

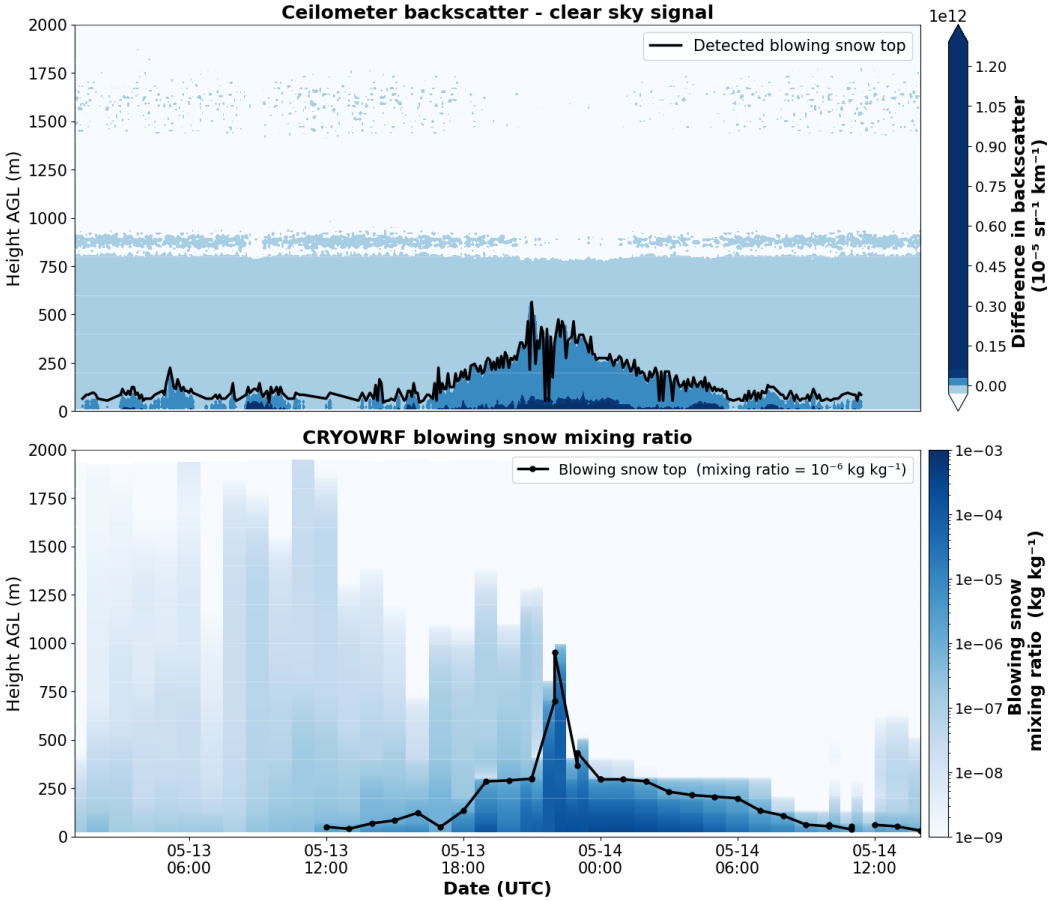


Figure 3.3: Top: timeheight plot, for the cold katabatic event, of the difference between the ceilometer backscatter and the clear sky reference profile [10^{-5} km^{-1} sr^{-1}]; the black line represents the blowing snow cloud top detected by the same algorithm. Bottom: timeheight plot, for the same event, of blowing snow mixing ratio in CRYOWRF ($kg\,kg^{-}1$); the black line represents the height at which the mixing ratio is equal to $10^{-6}\,kg\,k^{-1}$, threshold chosen to define the top of the blowing snow cloud in CRYOWRF. Notice how the model cloud height closely follows the observed one.

The retrieved height depends on the mixing-ratio threshold, which was selected by comparison with the ceilometer over the Cold Katabatic event. Its effect was

quantified through a sensitivity analysis over five values from 10^{-8} to $10^{-5}\,\mathrm{kg\,kg^{-1}}$. Across these, the bias decreased monotonically from 558 m to −11 m, with a MAE minimum of 85 m at the adopted value of $10^{-6}\,\mathrm{kg\,kg^{-1}}$. The correlation stays between 0.5 and 0.7 except at $10^{-8}\,\mathrm{kg\,kg^{-1}}$, where it is almost zero, and which places the cloud top far too high. The threshold therefore shifts the retrieved top vertically without substantially altering its evolution.

At the selected threshold the modelled cloud top follows the observed one well throughout the Cold Katabatic event (MAE 90 m, bias 45 m, $r = 0.70$). The height is slightly overestimated, and its temporal variation is well reproduced. The largest discrepancy in the height of the cloud is at the peak, where the modelled top overshoots the observed one by almost 500 m.

For the two synoptic events the comparison is of limited value, since the modelled and observed layer rarely coincide in time and the paired points are few (N = 5 for the Warm and N = 3 for the Transitional event). In both events the model produces a blowing snow cloud, but it is mostly flat, and much shallower than observed, reaching the $10^{-6}\,\mathrm{kg\,kg^{-1}}$ threshold only at a few points. In the Transitional Synoptic event the observed plume forms in the morning and peaks at about 750 m, while the modelled cloud appears only several hours later, peaking at about 300 m when the observed one had already dissipated (Figure B.9). This is consistent with the delayed initiation of transport observed for this event in the near-surface mass fluxes. In the Warm Synoptic event the ceilometer records a tall plume exceeding 1,200 m around midnight of April 25th (before it wasn't recording). The model produces a layer that partly overlaps with it in time but reaches only about 150–200 m (Figure B.10). Note that during this event precipitation was present, whose signal likely inflated the observed cloud height, being partly responsible for its found underestimation.

Chapter 4

Discussion

4.1 Wind-driven snow transport at PEA

The statistical analysis shows that snow transport at PEA is concentrated in the least frequent of the three regimes: the Warm Synoptic regime covers only 14 % of the record but transports snow during about three quarters of its hours, and produces the largest mean surface fluxes and the deepest blowing snow clouds, while the Cold Katabatic regime, which is present more than half of the time, transports snow more rarely. The frequencies of blowing snow detected by the ceilometer reproduce what Gossart et al. (2017) found at the same station using ceilometer data from 2010 to 2016. Blowing snow detected by the ceilometer algorithm (both BS and ceilometer-only classes) is present 9.2 % of the time here against their 13 %, and the split between clear-sky and mixed events is very similar: cloudless blowing snow (cat 1 in the blowing snow detection algorithm of 2.2) accounts for 32 % of the detections here and 30 % in their study.

These numbers also show that PEA is not representative of the ice sheet in the frequency of blowing snow and the conditions that lead to it. Blowing snow is detected by the ceilometer algorithm of Gossart et al. (2017) 36 % of the time at Neumayer station, which lies on the ice shelf and is exposed to storms (Gossart et al., 2017), against the 9 % to 14 % found at PEA with the same instrument. The contrast is even larger for the near-surface transport: at PEA snow is transported 22 % of the time, against 57 % at D17 and 81 % at D47 in coastal Adélie Land, where the katabatic winds sustain blowing snow throughout the year (C. Amory, 2020). Still, even if rarer than at other stations, katabatic blowing snow is present at PEA. When the drainage flow is strong enough it produces the highest median near-surface fluxes of the whole dataset, although the layer is on average shallower

than in synoptically driven blowing snow. These are the conditions for which the vertical extent of the blowing snow layer is best reproduced by the model (Section 4.4).

4.2 Cyclonic influence on simulation's accuracy

The errors in the simulation of mean variables fall within the spread that Gerber et al. (2023) report for CRYOWRF across the Antarctic stations, in the model evaluation that includes PEA. For surface pressure and potential temperature the MAE obtained here lies in the middle of the range spanned by their stations, while wind speed and relative humidity approach its edges. Wind speed is the least well reproduced variable in both studies, and they too find an overestimation at PEA. The two are however not directly comparable, since their innermost resolution is 27 km against 200 m here, which matters for a station as influenced by the surrounding topography as PEA.

The accuracy is not uniform, but changes markedly from one event to the next, and the ordering is the same for almost every variable. The Cold Katabatic event is the most consistent: all correlations are positive, and the biases are the lowest of the three simulations, except for pressure. The Transitional Synoptic event is the least accurate in every field. The Warm Synoptic case lies in between, but unevenly: it reaches the highest correlation of the whole validation for surface pressure ($r = 0.95$, bias -0.2 hPa), a field set by the large scale circulation, while its relative humidity correlation is negative and the wind speed is overestimated by $4.6\,\mathrm{m\,s^{-1}}$. Accuracy is therefore best for the locally forced katabatic flow and lowers when synoptic influence is present. It does not degrade for surface pressure though, meaning that, during the disturbed events, the model reproduces the large scale pressure field, but misses what these systems carry with them.

The synoptic conditions at PEA are not generated by the model, but inherited from the ERA-5 reanalysis used as initial and boundary conditions, to which the outer domain is nudged every six hours. So, the skill of the simulation during disturbed conditions is bounded by that of the reanalysis. Cyclones are hard to capture in the Southern Hemisphere, and in Antarctica, where observations are scarce, reanalyses and models are weakly constrained. The difficulty is found across scales: Priestley et al. (2023) show that the latest climate models (CMIP6) place the Southern Hemisphere storm track too far equatorward and underestimate cyclone intensity, while for short-range simulations Deb et al. (2016) find that Polar WRF sometimes fails to capture transient cyclones and their effect on the coastal winds, the same situation as the two synoptic events simulated here. ERA-5 itself carries documented biases in the intensity and moisture of these systems,

underestimating the surface wind, the water vapour and the cloud water within Southern Hemisphere cyclones (McErlich et al., 2023). This is what the Warm Synoptic event shows: the timing of the system is captured, since pressure has extremely high pearson correlation, but not its moisture content, nor more generally its structure and intensity. The cold and dry biases go in the same direction. Overall they are of −2.85 °C and −13 %, but they are not uniform: they are small in the Cold Katabatic event (−1.3 °C and −6 %) and much larger in the cyclonically driven ones (up to −5.1 °C and −25 % in the Transitional event, and −3.9 °C and −16 % in the Warm one). Since the warmth and moisture that reach PEA during disturbed conditions are carried by the cyclones (Gorodetskaya et al., 2013), and that moisture is already underestimated in the driving reanalysis, both biases may be also tied to the imperfect representation of the cyclonic conditions.

This is relevant for continental estimates of blowing snow sublimation as well. In fact, this sublimation is largest in the coastal areas (Palm et al., 2017), where cyclonic activity is strongest. Its estimates may therefore depend on how well models reproduce these coastal, cyclonically driven events, together with the temperature and humidity that come with them, which are here the least well captured. At the same time, these biases act in different directions and can lead to compensating errors: while the overestimated wind would increase transport and sublimation, the cold and dry biases and the too-high transport threshold go in the opposite direction. Because the system is highly non-linear, these errors can cancel out, and a modelled flux or sublimation close to the observations may hide compensating errors that still need to be investigated.

4.3 Underestimation of blowing snow fluxes

The model underestimates the near-surface mass flux in every simulated event. The cause is the threshold friction velocity of Eq. 2.3, which is too high (Fig. 4.1). Transport is observed to start at friction velocities between $0.4\,\mathrm{m\,s^{-1}}$ to $0.6\,\mathrm{m\,s^{-1}}$, while the median threshold computed by CRYOWRF is almost $0.8\,\mathrm{m\,s^{-1}}$ in the Cold Katabatic event, and almost $1\,\mathrm{m\,s^{-1}}$ in the other two. Li et al. (1997) report typical threshold friction velocities between $0.15\,\mathrm{m\,s^{-1}}$ to $0.25\,\mathrm{m\,s^{-1}}$ for fresh, loose and dry snow, and between $0.25\,\mathrm{m\,s^{-1}}$ to $1.0\,\mathrm{m\,s^{-1}}$ for older, wind-hardened, dense or wet snow. The observed values fall in the upper half of this range, while the modelled ones sit at its upper limit, and at times above it.

The uncertainty of the measurements against which the model is validated should also be considered. Both the SPC and the FlowCapt carry large uncertainties on the absolute flux (Sections 1.2.3 and 1.2.2). Therefore, while the underestimation itself is robust, being consistent across both instruments and all events, its exact

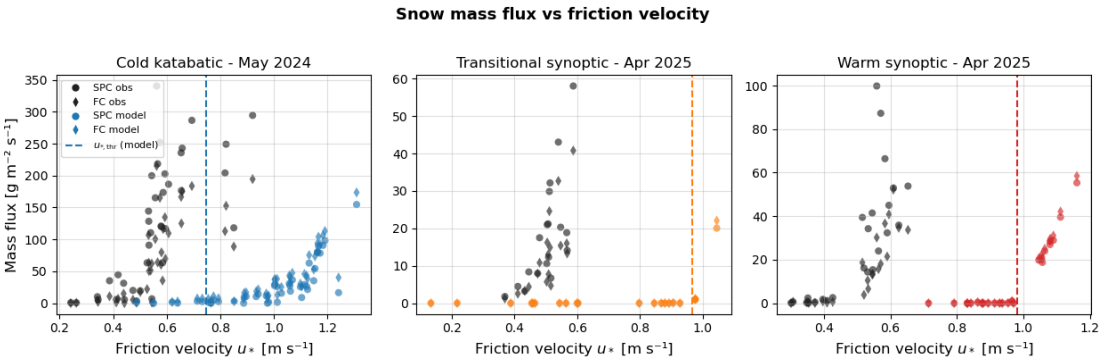


Figure 4.1: Mass flux vs friction velocity of both FlowCapt and SPC measurements, and corresponding value from CRYOWRF. Median modelled threshold friction velocity is represented as a dotted line. Observed friction velocities are derived from eddy-covariance measurements by the sonic anemometer on the SFC AWS. The threshold friction velocity here is too high compared to the measured friction velocities, which limitates the amount of snow entrained in saltation.

magnitude is not.

Snow density could possibly also be underestimated in the events. In fact, snow density given by the spin-up is between $300\,\mathrm{kg\,m^{-3}}$ to $400\,\mathrm{kg\,m^{-3}}$, against the $464\,\mathrm{kg\,m^{-3}}$ measured in a snow pit at PEA in January 2025. Note however that this value represents a single point in time, and continuous measurements are not available. Moreover, it was retrieved with a density cutter, and therefore does not provide density purely of the snow surface, but its average over the first few centimetres. If the modelled density were indeed too low, this would lower the coordination number and, through Eq. 2.3, the threshold itself. This possible error, and the overestimation of wind speed, would both on their own increase snow transport. Nonetheless, the flux is underestimated.

A third factor would push to an increase in snow transport. It is the roughness length: its value is prescribed and fixed throughout the simulation, to $2 \times 10^{-3}\,\mathrm{m}$, while measurements at PEA are an order of magnitude smaller (ranging from $1 \times 10^{-4}\,\mathrm{m}$ to $6 \times 10^{-4}\,\mathrm{m}$ in 2024 data). The choice of increasing the imposed roughness length in WRF is commonly made to compensate for the overestimation of wind speed, which can occur when topography is not resolved. A higher value of roughness length is expected to have two consequences. The first is that it should dampen wind speed. Nonetheless, wind speed remains too high. The second is that it increases friction velocities, and consequently should lead to increased snow drift. The friction velocity is diagnosed from the logarithmic wind profile, so it depends on the simulated wind speed and on the roughness length. In figure 4.1 we can

see that the whole distribution of friction velocity is shifted towards higher than measured values: part of the shift comes from the overestimation of wind speed, and the high roughness length also partly contributes.

A feedback in this process is expected, where high wind speed, through snow transport, compacts the surface snow, raising its density, therefore the threshold friction velocity of Eq. 2.3, which in turn damps the drift. It is a self-limiting mechanism. This is visible in the Cold Katabatic event: the surface density grows during the event, from about 90 to 520 $\mathrm{kg\,m^{-3}}$, and the threshold friction velocity too, rising from about 0.4 to 0.8 $\mathrm{m\,s^{-1}}$. The friction velocity, however, grows as well and stays above the threshold, so transport is sustained. This is the event with the highest modelled fluxes, exceeding 150 $\mathrm{g\,m^{-2}\,s^{-1}}$ at the peak. In the two synoptic events the density is instead almost constant, with a single step of about 100 and 50 $\mathrm{kg\,m^{-3}}$ in the Transitional and Warm cases, and the threshold friction velocity stays constant throughout. These are the events with little modelled transport, almost none in the Transitional case and not exceeding 60 $\mathrm{g\,m^{-2}\,s^{-1}}$ in the Warm one.

Gerber et al. (2023) find lower simulated than measured fluxes at D-17 and D-47, and since the FlowCapt sensors used there underestimate the transported mass themselves (Sect. 1.2.3), they conclude that an underestimation of blowing snow fluxes may be present in CRYOWRF, and that more case studies are needed to confirm it. At PEA they find the opposite, and relate the higher simulated fluxes to an overestimation of the wind speed. Here the wind is overestimated as well, but the flux is underestimated.

Several sources of uncertainty may contribute to this overestimation of the threshold friction velocity. The first is the microstructure simulated for the events: grain radius, bond radius, sphericity and coordination number are used to compute the threshold friction velocity, but none of them is measured at PEA, and directly comparable measurements are scarce in the literature. These values come from the snowpack spin-up, which is a further source of uncertainty in itself: it was run at continental scale, with a resolution of 27 km, and interpolated to the model domain via nearest neighbour. The state of the snowpack is highly variable in space, especially in topographically complex areas, and the topography around PEA, with the Sør Rondane Mountains, the escarpment and the nunatak, is not resolved at that resolution.

Though not affecting the threshold friction velocity, other empirical parameters of the scheme are a further source of uncertainty. Some are the three constants in the computation of the saltating mass flux, calibrated by Vionnet et al. (2014) on wind-tunnel tests.

The formulation of the scheme is a third one. Snow particles enter saltation either by aerodynamic entrainment, or by being ejected by the impact of a saltating particle, which is called splash. Splash makes the process easier to maintain than to initiate, so initiation and maintenance are described by two different thresholds: the fluid threshold, and the impact threshold (Melo et al., 2024). In CRYOWRF only the fluid threshold is considered, therefore splash is not accounted for explicitly, but only implicitly through the saltation parameterisation. Melo et al. (2024) show that this assumption is shared by RACMO, MAR and Meso-NH. They also show that splash is the dominant entrainment mechanism at high friction velocities, which are the conditions of the events simulated here.

A further factor concerns the Warm Synoptic event specifically. Gerber et al. (2023) note that precipitation is not represented on the fine mesh below the first WRF level, where the surface flux is computed. During precipitation, the SPC and the FlowCapt measure the falling and horizontally advected particles together with the blowing snow, while the model does not include them at this level. Part of the observed surface flux in this event is therefore precipitation that the model, by construction, cannot reproduce, which adds to the underestimation from the threshold.

The mean radius of the blowing snow particles is underestimated as well. Several elements of the scheme control it: the mean diameter prescribed at the saltation boundary, and the advection-diffusion equations themselves. In this case too, it is hard to establish which factor is responsible for this bias. The comparison is also affected by the SPC, which at the high fluxes of these events undercounts the particles and overestimates their size (Section 1.2.2). Therefore, part of the difference may be observational.

For the mass flux, then, the accuracy of the simulation seems to depend on the state of the snowpack, and more generally on the blowing snow scheme, more than on the synoptic conditions of the event, unlike the near-surface atmospheric variables (Section 4.2). Future work should concentrate on isolating which of these components generate the biases, enabling a more accurate representation of blowing snow in CRYOWRF. It is important to also note that both the SPC and the FlowCapt sensors, especially the latter, are notably not reliable (see Sections 1.2.3 and 1.2.2).

4.4 Validation of the vertical dimension of the blowing snow cloud

Because the ceilometer resolves the blowing snow layer in the vertical, the model can be compared on a quantity that evaluations of blowing snow schemes have not used so far, its height. The agreement, during the Cold Katabatic event, is better in this dimension than at the surface. The modelled top follows the observed one with a high correlation of $r = 0.70$, higher than any value obtained for the mass flux at the surface. The height of the cloud, though with the inherent limitation that comes from the selection of the threshold by calibration against observation (Sect. 2.4.4), is well captured, with a bias of 45 m, against a mass flux that in the same event is largely underestimated. The model therefore places the top of the layer correctly, or even slightly too high, and follows its variation in time, even where it transports too little snow. It should be noted that, since the modelled top was calibrated on observation, it is not an independent result. Its temporal agreement, instead, is, and it is stable for three orders of magnitude of the threshold. This gives confidence in the representation of the vertical development of the blowing snow cloud under katabatic conditions, and, with the limitations above, of its height.

The same cannot be established for the other two events, where the modelled cloud is strongly underestimated in height and its timing is not captured. Since the blowing snow mixing ratio has a single source, the saltation flux at the lower boundary (Section 2.4.1, Eq. 2.4), the low modelled top here is likely a consequence of the very low modelled surface fluxes in the synoptic cases. The modelled cloud top in the Cold Katabatic case doesn't seem to be influenced by the underestimation though. This event has high biases and underestimation of the flux, but also the highest modelled near-surface fluxes in absolute terms. The Warm Synoptic event is further affected by the presence of precipitation, which makes ceilometer measurements, and the derived cloud top, less reliable (Section 1.2.4 iii and iv). Since blowing snow at PEA is to a large extent driven by synoptic conditions, the regime for which the vertical validation is found to hold is not the one that produces most of it.

PEA is however a peculiar site in this respect, because its katabatic flow is strongly sheltered by the Sør Rondane mountains. Instead, along the coast and the escarpment the katabatic winds dominate the near-surface flow (Parish et al., 2007) and sustain drifting snow throughout the year (C. Amory, 2020). The conditions under which the model is here shown to reproduce the height of the layer are therefore those that prevail over much of the Antarctic continent, which makes the result relevant well beyond the station.

The vertical development of the cloud is tied to the vertical velocity field, and this differs between the events. In the advection diffusion equation for blowing snow (Eq. 2.4), which governs the blowing snow scheme in CRYOWRF, the particles are carried upward in two ways: by the vertical wind, which is part of the resolved flow, and by turbulent diffusion, which is not resolved but represented through the turbulent diffusion coefficient K_{bs}, tied to the boundary layer scheme (Skamarock et al., 2019; Sharma et al., 2023). Which of the two dominates depends on the event. The along-flow transects (Fig. B.3), taken through PEA along the mean flow direction of each event, show gravity waves forming as the stably stratified katabatic flow crosses the Sør Rondane Mountains, with vertical velocities reaching about $6.3\,\mathrm{m\,s^{-1}}$. There, the cloud is lifted by a vertical motion that the model resolves explicitly at 200 m, and its height is well reproduced. In the two synoptic events no comparable wave structure forms, and the vertical velocities are weaker, up to about $1.5\,\mathrm{m\,s^{-1}}$. The depth of the layer is then left mostly to the parameterised diffusion.

The two mechanisms above describe how the snow already in the column is carried upward, but the advection term of Eq. 2.4 also acts horizontally, so the blowing snow at PEA could also come from upstream sources. Suspended particles travel long distances before settling, and part of the layer over the station may have been eroded upstream and advected into the column. This is especially relevant in the katabatic event, where the flow crosses the Sør Rondane Mountains and the escarpment before reaching PEA: over these barriers the accelerated flow enhances erosion, and the snow mobilised there can be carried downstream and lifted over the station.

The synoptic events are moreover tied to the large-scale circulation, which is harder to reproduce than the locally forced katabatic flow. The katabatic flow is generated within the domain, by the drainage interacting with the topography and by the radiative cooling of the surface, so the model reproduces it largely independently of its boundaries. The synoptic forcing, instead, is inherited from the ERA-5 reanalysis to which the outer domain is nudged (Section 4.2): the large-scale pressure field, and with it the position and timing of the systems, is captured, but not the moisture and warmth they carry.

The two synoptic events fail for different reasons. In the transitional one the modelled flux collapses almost to zero, so that too little snow is available for a layer to form. In the warm one the comparison is limited by the observation itself: the tall cloud seen by the ceilometer coincides with a lower surface flux and likely reflects precipitation, which the model does not represent (Section 1.2.4). The vertical extent is therefore well captured only in the katabatic event.

The role of resolution can be seen in Figures 4.2, B.9 and B.10. In the Cold

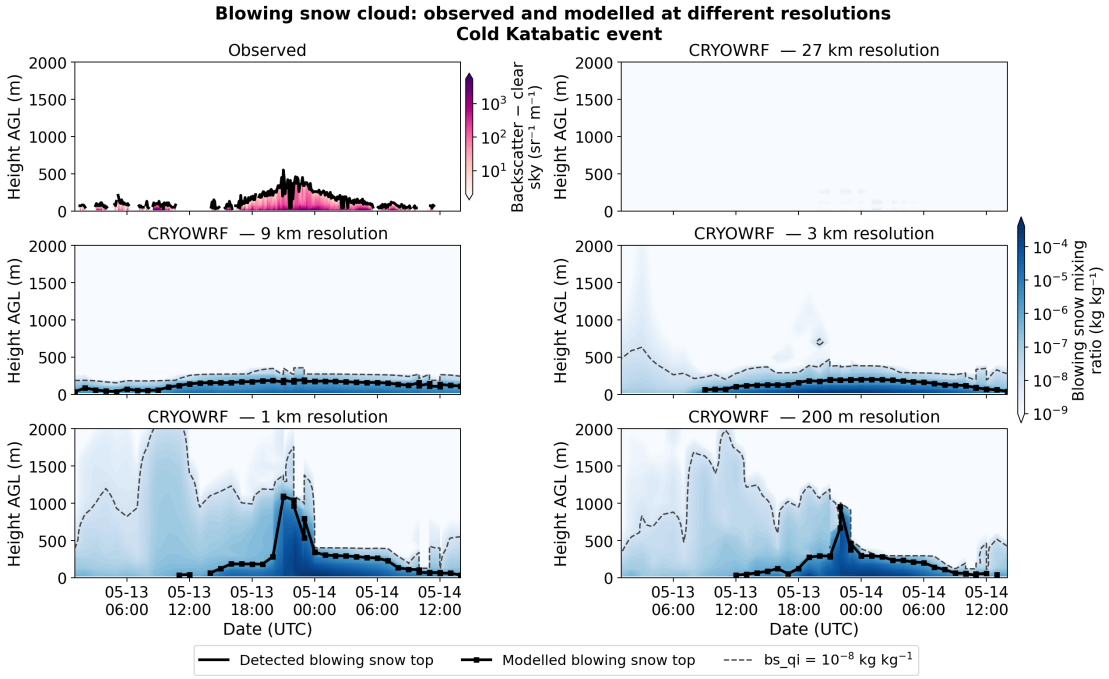


Figure 4.2: Timeheight plot of the blowing snow layer during the Cold Katabatic event, from the ceilometer and from CRYOWRF at the five different resolutions. Top left: ceilometer attenuated backscatter minus the clear-sky reference profile ($\mathrm{sr}^{-1}\,\mathrm{m}^{-1}$), with the blowing snow layer top retrieved by the detection algorithm of Section 2.2 (black line). Remaining panels: modelled blowing snow mixing ratio ($\mathrm{kg\,kg}^{-1}$) at 27 km, 9 km, 3 km, 1 km and 200 m horizontal resolution. In each, the black line marks the modelled cloud top, defined as the height where the mixing ratio falls below $10^{-6}\,\mathrm{kg\,kg}^{-1}$, and the dashed lines the $10^{-8}\,\mathrm{kg\,kg}^{-1}$ iso-values. Heights are above ground level. The cloud is seen at 200 m and 1 km resolution, but becomes completely flat at 3 and 9 km, and vanishes at 27 km resolution.

Katabatic event the modelled cloud collapses between 1 and 3 km: at 1 km its height still reaches about 1,000 m, while at 3 km it flattens to about 200 m, since the gravity waves are no longer resolved. In the two synoptic events the modelled top is instead almost independent of resolution, staying around 250 m to 300 m from 9 km down to 200 m, as expected for a layer set by parameterised diffusion rather than by resolved motion. At 27 km, however, all three events lose the blowing snow cloud entirely. Resolution is therefore essential to represent the vertical extent of blowing snow, particularly for katabatic flow, where the topography and the gravity waves it generates need to be resolved, but also in general, since the cloud disappears at continental resolution.

This is relevant for interpreting continental estimates of blowing snow sublimation.

The estimate from CRYOWRF, of about 101 Gt/year (Gerber et al., 2023), was obtained at 27 km, the resolution at which the blowing snow cloud is here shown to disappear. In general, estimates obtained from models (CRYOWRF and RACMO in two different configurations) are lower than the satellite-based one (Palm et al., 2017). The fact that both of these models were run at this coarse resolution, which here we show is unable to represent the vertical extent of the layer over which sublimation occurs, may be part of the reason. Long or continental-scale simulations, however, cannot currently afford the resolution used here, which makes the representation of blowing snow at coarse resolution an open challenge.

Conclusion

This thesis characterised drifting and blowing snow at Princess Elisabeth Antarctica station, and validated the CRYOWRF model against the observations, under the different meteorological regimes that drive snow transport at the site. Hourly meteorological data of 2024 and 2025 was classified, following Gorodetskaya et al. (2013), into three regimes: Cold Katabatic, Transitional Synoptic and Warm Synoptic. Transport events were then defined from the instruments, and their frequency, near-surface mass flux and vertical extent were characterised for each regime. Finally, one event per regime was simulated with CRYOWRF up to 200 m horizontal resolution, and the model validated against the surface variables, the near-surface mass fluxes, and, for the first time, the height of the blowing snow layer retrieved from the ceilometer.

The statistical analysis showed that, at this station, snow transport is dominant in the Warm Synoptic regime: it covers only 14 % of the record but transports snow during about three quarters of its hours, while the Cold Katabatic regime, present more than half of the time, transports snow about 5 % of its hours. PEA is therefore not representative of the conditions in which blowing snow prevails at continental scale, which are the regions of strong katabatic flow. Drainage flow at this station is instead reduced by the sheltering of the Sør Rondane Mountains. Strong katabatic blowing snow events, such as the one simulated here, are nonetheless present, even if much rarer, and produce the densest near-surface fluxes of the whole dataset.

The accuracy of the simulation of the near-surface atmospheric variables is not uniform, but best for the locally forced katabatic flow and degrading when synoptic influence is present. During the disturbed events the model reproduces the large-scale pressure field, but not the temperature and moisture the cyclones carry, which are likely already underestimated in the ERA-5 reanalysis used as boundary conditions. This dependence on the driving boundary conditions is a challenge for simulations, and even more so for projections, where, obviously, unlike reanalyses, simulations cannot be constrained to observations. It also matters for sublimation of blowing snow, which depends on the temperature and humidity that

are here the least well captured.

The near-surface mass flux is underestimated in every simulated event. This is not explained by the atmospheric forcing: the wind speed is in fact overestimated, which would increase transport rather than reduce it. The underestimation stems instead from the threshold friction velocity, which is too high, and which is computed directly from the snow microstructure. The accuracy of the flux therefore depends on the initial state of the snowpack and on the blowing snow scheme, and in particular on the computation of the threshold, more than on the synoptic conditions of the event. Several factors push towards more transport, yet the flux is underestimated.

The vertical extent of blowing snow had not been used before to evaluate a blowing snow scheme. Here it could be, and in this aspect the model agrees with the observations better than at the surface. In the Cold Katabatic event the model transports too little snow, but it places the top of the layer correctly, and follows its evolution in time: the modelled top reproduces the observed one with a mean absolute error of 90 m and a correlation of r=0.70, higher than any value obtained for the mass flux. The reason is that at 200 m the model resolves the gravity waves that form as the stably stratified katabatic flow crosses the Sør Rondane Mountains, and their updrafts set the height of the layer. This vertical development is lost at resolutions coarser than 1 km, where the waves are no longer resolved. In the two synoptic events no such waves form, so the height is left to the turbulent diffusion, and is strongly underestimated at every resolution. At 27 km the blowing snow cloud vanishes entirely in all three events. Horizontal resolution is therefore essential to represent the vertical extent of blowing snow, in particular under katabatic conditions, where the topography is essential.

These results are relevant for continental estimates of blowing snow sublimation. Two results found in this work both suggest that the estimate obtained with CRYOWRF (101 Gt/year) may be too low: the underestimation of the near-surface mass fluxes, and the disappearance of the blowing snow cloud at 27 km, the resolution at which the continental estimate was produced. This would be consistent with the fact that this estimate, and the one from RACMO (175 $\pm$ 7 Gtons/year, also obtained at continental resolution), are well below the satellite-based one (393 $\pm$ 196 Gtons/year).

CRYOWRF is one of the few atmospheric models that represent blowing snow explicitly, which matters in snow-covered regions because blowing snow contributes to the two-way exchange of mass, moisture and heat between the snowpack and the atmosphere. This work evaluated CRYOWRF against a multi-instrument dataset at PEA, identified some weaknesses, and pointed to directions for its improvement and for its use at larger scale.

Outlook

The overestimation of the threshold friction velocity should be further investigated. The threshold is computed from the snow microstructure, which here comes from a spin-up run at continental resolution. A higher-resolution spin-up restricted to PEA, though not generalisable to other locations, could help assess whether the computed microstructure is actually responsible for this error. Field measurements of surface snow microstructure, currently scarce, would help constrain it further and could be included in future measurement campaigns at PEA.

Beyond the accuracy of the scheme itself, a further challenge lies in the horizontal resolution. The very high resolution used here, 200 m, was needed to resolve the complex topography around PEA and to reproduce the height of the blowing snow layer, and it is not affordable over larger areas or longer periods. At the coarse resolutions used for continental simulations the model does not see the blowing snow cloud, and it does not resolve the topography that controls it under katabatic conditions. Representing blowing snow, and its vertical extent, at coarse resolution therefore remains an open challenge.

A promising approach is offered by intermediate-complexity models, such as HICAR (Reynolds et al., 2024). By using a simplified flow solver, HICAR is far more efficient than high-resolution models like CRYOWRF, reaching comparable or higher resolution at much lower computational cost, and can therefore cover the seasonal to climatological time scales required for long-term simulations. HICARsnow, the coupling of HICAR with the snow model SNOWPACK, shares the same physically-based representation of blowing snow as CRYOWRF. The main question for these approaches is whether a simplified representation of the atmospheric dynamics can reproduce blowing snow with an accuracy comparable to CRYOWRF, while preserving the processes key to its representation, such as the gravity waves that in this thesis are shown to be essential to capturing the height of the blowing snow cloud in katabatic conditions. Where explicit representation remains too costly, machine-learning emulators, such as physics-informed neural networks (PINNs), offer a further promising route.

Ultimately, a reliable representation of blowing snow is needed for more accurate estimates of its sublimation, which currently disagree widely between studies. More generally, it is essential for including the process in long-term simulations and future climate projections. Such a model is particularly important in Antarctica, where in situ observations are scarce and difficult to obtain, and where models are consequently an essential tool for studying how these processes have evolved, and will continue to evolve, in one of the fastest-warming regions of a changing climate.

Appendix A

Meteorological clustering

A.1 Detrending

The clustering variables are detrended before standardisation, by removing a seasonal and a diurnal baseline built from the 2023–2025 climatology (Section 2.1). Figures A.1 and A.2 illustrate the two baselines for air temperature, taken as an example: the seasonal cycle, smoothed with a circular 30-day rolling mean and shown against the hourly data of 2024, and the mean daily cycle, computed by month and hour of day.

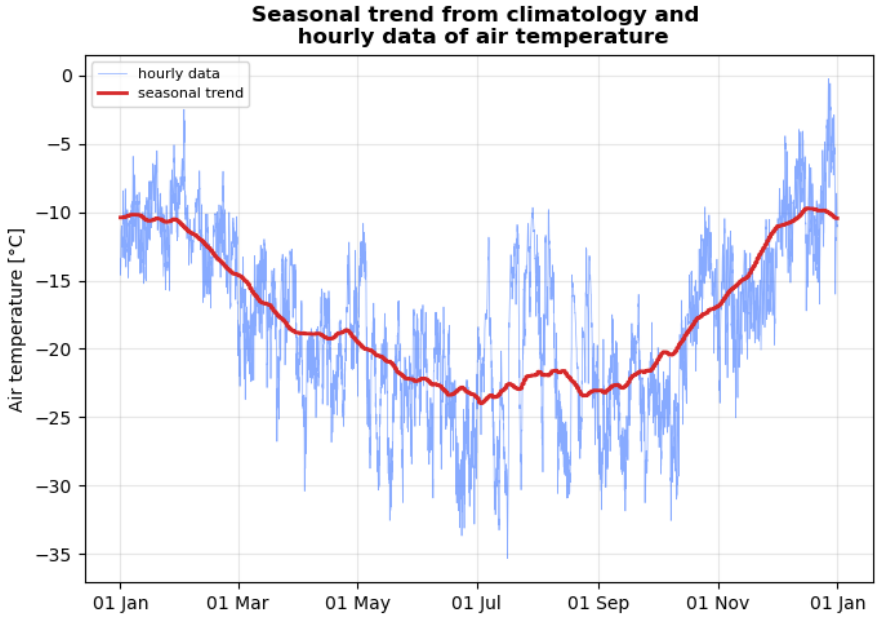


Figure A.1: Seasonal trend from climatology (computed using data from 2023 to 2025) and hourly data of air temperature in 2024.

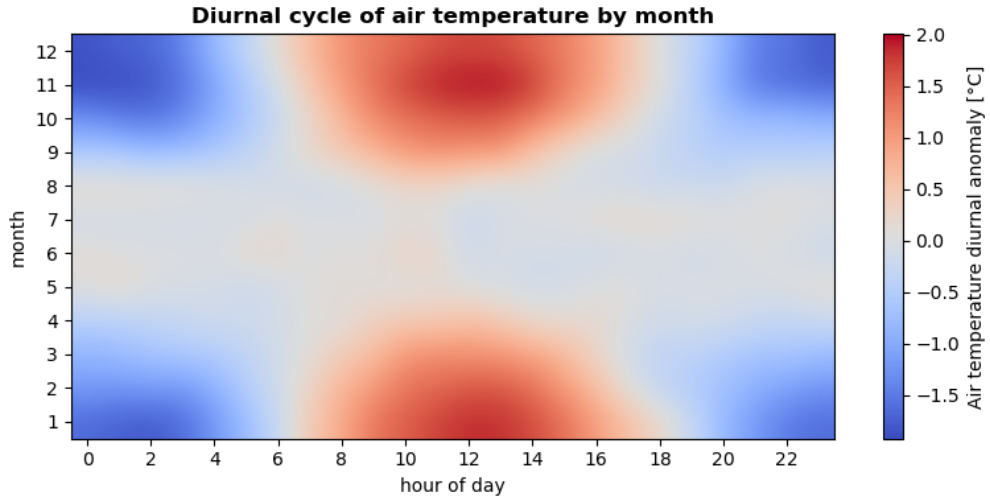


Figure A.2: Diurnal cycle of air temperature by month from climatology (computed using data from 2023 to 2025).

Table A.1: Warm Synoptic regime across all years: per-year hourly clustering (2023–2025), combined 3-year hourly clustering, and Gorodetskaya et al. (2013) (2009/2010, daily).

Variable	2009	2010	Per-year 2023	Per-year 2024	Per-year 2025	Combined
Freq [%]	14	18	21	10	29	14
TA [°C]	-16.0	-16.0	-15.0	-14.2	-17.1	-13.8
q [g kg^{-1}]	1.10	1.00	1.02	1.16	0.79	1.15
P [hPa]	824	825	830	833	823	832
WS [m s^{-1}]	12.0	7.0	8.2	10.5	6.8	8.2
LW_{in} [W m^{-2}]	228	207	208	238	206	225
$\partial T/\partial z$ [K m^{-1}]	0.4	0.9	0.9	0.6	1.3	0.8
WD [°]	95	113	88	70	89	80

A.2 Choice of the clustering period

The clustering was first applied to each year separately. By clustering one year at a time, cluster boundaries adapt to the conditions of that year. The three regimes of Gorodetskaya et al. (2013) were found in each year, at both hourly and daily resolution. However, the per-year classification produces an inconsistent warm synoptic regime. At hourly resolution its frequency is 29% in 2025, about three times the value in 2024, well above the 21% of 2023, and almost double the values reported by Gorodetskaya et al. (2013) for 2009 and 2010. This over inclusive 2025 cluster is also weaker overall than the warm clusters of the other years (Table A.1): it is colder, drier, less windy, and retains a stronger inversion. This is likely an artefact of the per-year clustering: since genuine synoptic events were fewer that year, the algorithm pushes the warm boundary too wide and includes transitional hours, diluting the cluster mean towards intermediate values. Since both the cluster boundaries and their mean conditions vary from one year to the next (for all groups, and especially for the warm synoptic), the per-year classification does not provide a stable basis for the subsequent analyses.

To obtain a definition consistent across years, the clustering was run on three years (2023-2025) together. 2023 was also included to limit the influence of conditions specific to one year biasing the classification. For the hourly three year run regimes were defined using a subset of 15000 hours, and the remaining ones were assigned based on their distance to the identified centroids in the standardised space, to reduce computing time. Switching from the per-year classification to this combined one reassigns about 35% of the 2025 hours: many of the over-estimated warm synoptic hours are reclassified as transitional ($\sim$ 1430 hours), and many of the

Table A.2: Mean conditions of the Warm Synoptic regime within the combined classification, broken down by year. 2009–2010 from Gorodetskaya et al. (2013) (daily); 2023–2025: combined 3-year hourly clustering, this study.

Year	Freq [%]	TA [°C]	q [g kg^{-1}]	P [hPa]	WS [m s^{-1}]	LW_{in} [W m^{-2}]	$\partial T/\partial z$ [K m^{-1}]	WD [°]
2009	14	-16.0	1.10	824	12.0	228	0.4	95
2010	18	-16.0	1.00	825	7.0	207	0.9	113
2023	14	-13.7	1.15	833	8.0	219	0.9	86
2024	17	-13.7	1.18	833	8.2	228	0.7	76
2025	12	-14.0	1.10	827	8.3	228	0.8	77

transitional synoptic hours move to the cold katabatic regime ($\sim$ 960 hours).The 2025 warm synoptic cluster's frequency is now 12% of the hours, with mean cluster variables much closer to those of the other years (2024, 2009, 2010) (Table A.2). The year 2024 is more stable, with about 19% of its hours reassigned mainly from the transitional to the warm and cold regimes. This three-year combined clustering provides a single, consistent definition of the clusters, more similar to values found by Gorodetskaya et al. (2013) both in frequency and mean cluster variables. It is the classification that we use consistently throughout this work.

A.3 Effect of temporal resolution

The dendrograms of the regimes are shown in Figure A.3, and represent the hierarchy of the clustering as a tree, where the height at which two branches join measures how different the corresponding groups are. At hourly resolution the first split of the tree separates the cold katabatic regime from the synoptic family, and the second splits the latter into transitional and warm, reproducing the expected hierarchy.

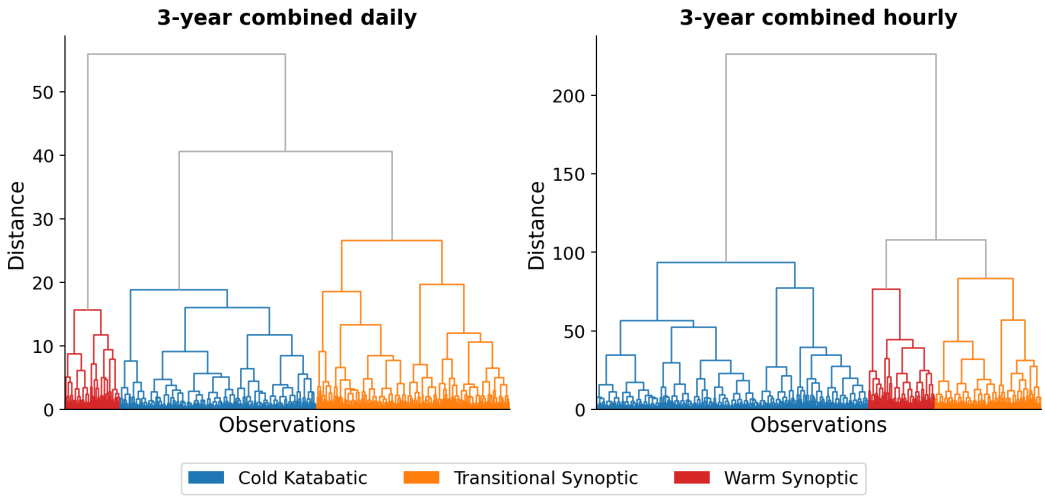


Figure A.3: Ward clustering dendrograms for 2023–2025 at daily (left) and hourly (right) resolution. At daily resolution Ward is applied to all days, while at hourly resolution it is applied to a subset of 15 000 hours (the remaining hours are then assigned to the nearest cluster centroid in the standardised space). Each leaf at the bottom is one observation, and branches merge upwards into larger groups. Cutting the tree at $k = 3$ gives the three regimes (blue: cold katabatic; orange: transitional synoptic; red: warm synoptic), while grey links join different regimes above the cut.

The hierarchy of the clustering, and the regime frequencies, change between the two resolutions. At daily resolution the warm synoptic regime is the most distinct one and separates first, while the cold and transitional regimes are the closest pair (the distance between their centroids in the standardised space is 1.77, against 2.73 for transitional–warm and 4.29 for cold–warm). This is a consequence of daily averaging, in fact most regime episodes are shorter than a day. At hourly resolution the median length of regime occurrences is 6–7 h for the cold regime, 4 h for the warm and 3–4 h for the transitional, and over 90% of transitional episodes last less than 24 h. A day that has both katabatic conditions and synoptic incursions is more easily averaged into a transitional synoptic day. As a result, daily resolution over-represents the transitional regime (44% of days against 27% of hours).

At hourly resolution these short synoptic periods can instead be resolved, and frequencies change. The cold katabatic regime is now the most compact and distinct cluster and the one that separates first (Fig. A.3), while the transitional and warm regimes fall in the same synoptic branch (Fig. A.3). The transitional regime sits almost exactly between the other two (its centroid is 2.16 from the cold and 2.25 from the warm), meaning the three regimes are evenly spaced. The regime mean values themselves change little between resolutions, confirming that the same

physical states are captured. The hourly resolution is adopted here because it resolves the brief synoptic intrusions that the daily mean would otherwise average out, and because it is closer to the duration of drifting and blowing snow events, the main focus of this work.

Appendix B

Additional figures of the simulated events

B.1 Synoptic maps and vertical transect

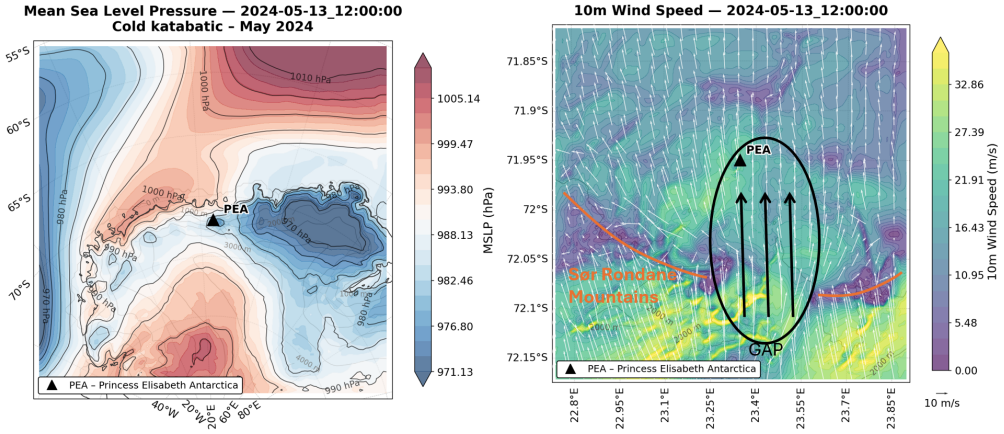


Figure B.1: The Cold Katabatic event on 2024-05-13 12:00 UTC from the CRYOWRF simulation. Left: mean sea level pressure in domain 1 (hPa). Right: 10 m wind speed ($\mathrm{m\,s^{-1}}$, shading) and wind vectors in domain 5; the reference arrow is $10\,\mathrm{m\,s^{-1}}$. PEA is marked by the black triangle, and the 2,000 and 3,000 m elevation contours are shown. In the right panel, the oval indicates the gap in the mountains, through which the flow is channeled (its direction highlighted with the three arrows). A low-pressure system lies to the east of the station (left), and the associated pressure gradient enhances the drainage flow and channels it through the Sør Rondane Mountains (right), producing the unusually high katabatic wind speeds visible near PEA in the right panel.

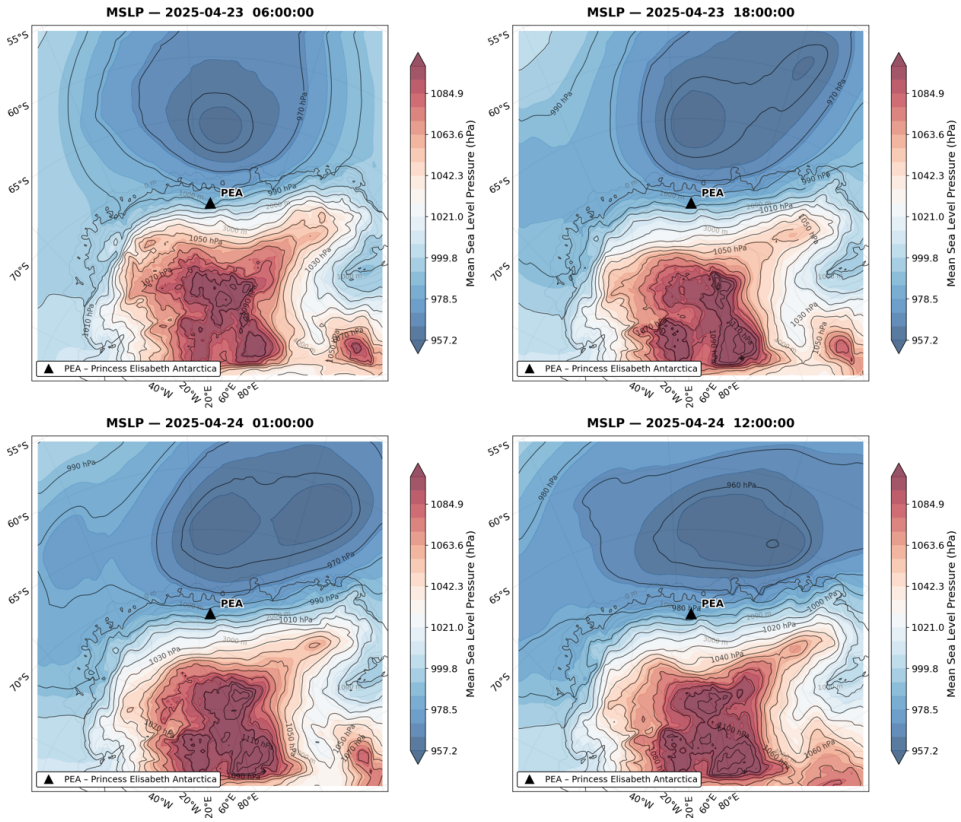


Figure B.2: Evolution of the mean sea level pressure (hPa) during the two synoptic events, from the CRYOWRF simulation (domain 1), at four times: (a) 2025-04-23 06:00, (b) 2025-04-23 18:00, (c) 2025-04-24 01:00 and (d) 2025-04-24 12:00 UTC. PEA is marked by the black triangle. In (a) a single cyclone approaches the coast north of PEA, driving the Transitional Synoptic event. A second cyclone then develops to its east (b), and the two systems rotate around each other in a Fujiwhara interaction (c), until one is absorbed by the other into a single low (d). This low drives the Warm Synoptic event and brings precipitation to PEA. Sea-level reduction is not meaningful over the high interior.

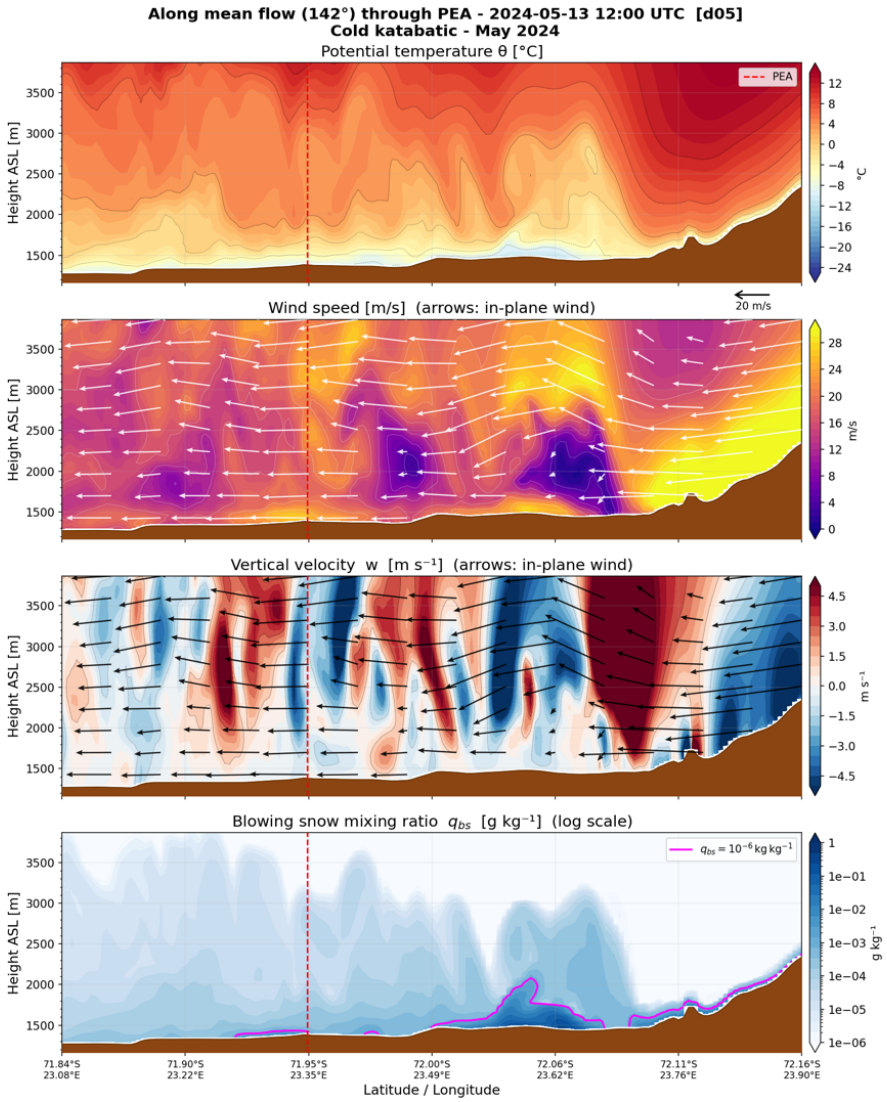


Figure B.3: Vertical cross-section along the mean flow (142°) through PEA for the cold katabatic event, 23:00 UTC 13 May 2024 (domain d05, 200 m). Axis: latitude/longitude along the transect; red dashed line = PEA; brown = model terrain. Panels: (a) potential temperature θ (°, with isolines); (b) wind speed ($\mathrm{m\,s^{-1}}$); (c) vertical velocity w ($\mathrm{m\,s^{-1}}$; red = ascent, blue = descent); (d) blowing-snow mixing ratio q_{bs} ($\mathrm{g\,kg^{-1}}$, log scale), magenta line = $q_{\mathrm{bs}} = 10^{-6}$ kg kg^{-1} isoline (top of the blowing-snow layer). In (b) and (c), arrows show the in-plane wind (reference vector $20\,\mathrm{m\,s^{-1}}$). The gravity waves cause updrafts with high vertical velocities, which at this precise time reach $4.5\,\mathrm{m\,s^{-1}}$, and determine the height of the cloud.

B.2 Mass flux timeseries: transitional and warm synoptic

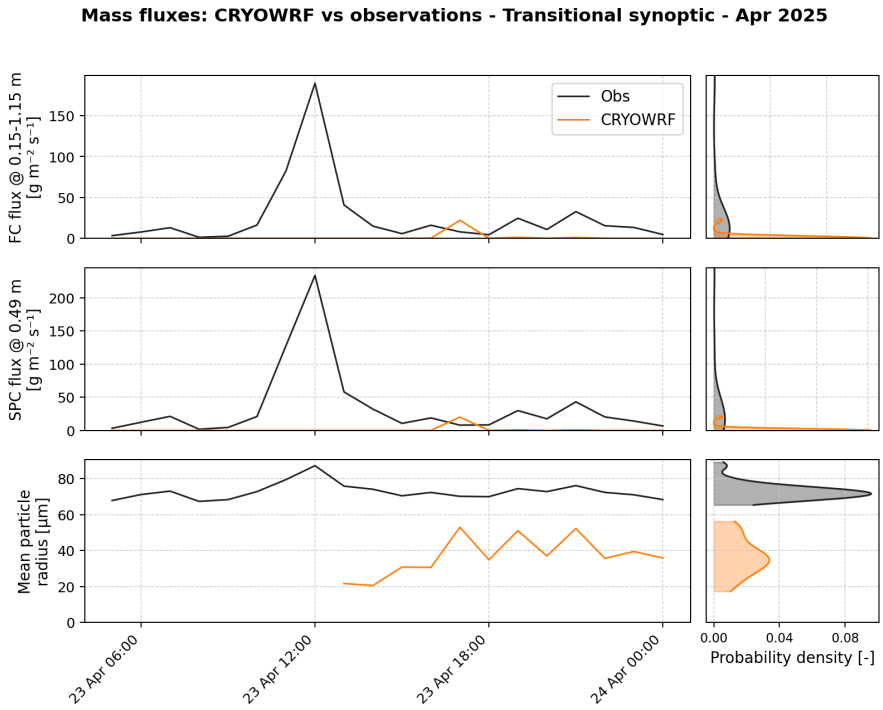


Figure B.4: Same as Figure 3.2, but for the Transitional Synoptic event

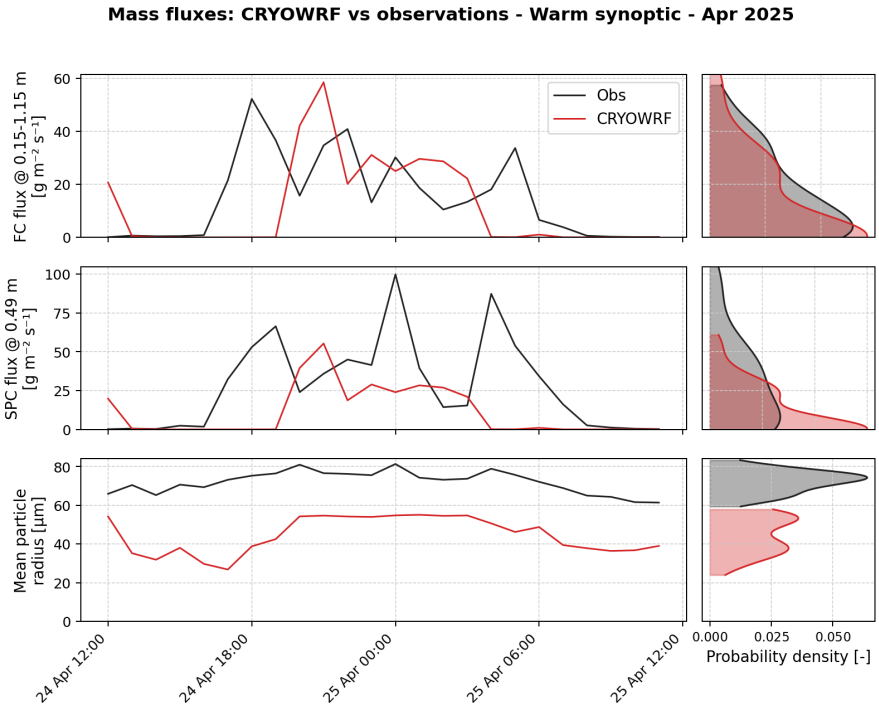


Figure B.5: Same as Figure 3.2, but for the Warm Synoptic event

B.3 Blowing-snow cloud height

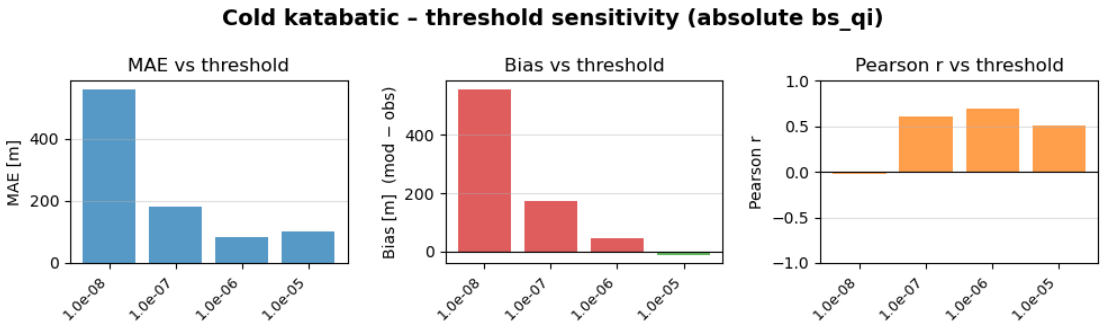


Figure B.6: Barplots, for the Cold Katabatic event, of MAE, Bias, and Pearson correlation of tested blowing snow mixing ratio thresholds to define the cloud top in CRYOWRF, compared to the cloud top obtained from the ceilometer algorithm. $bs_qi = 10^{-6}$ achieve the lowest MAE and highest correlation, and the second lowest bias. Correlation stays stable across 2 orders of magnitude, indicating that, independently of the chosen threshold, the evolution of the cloud is well represented.

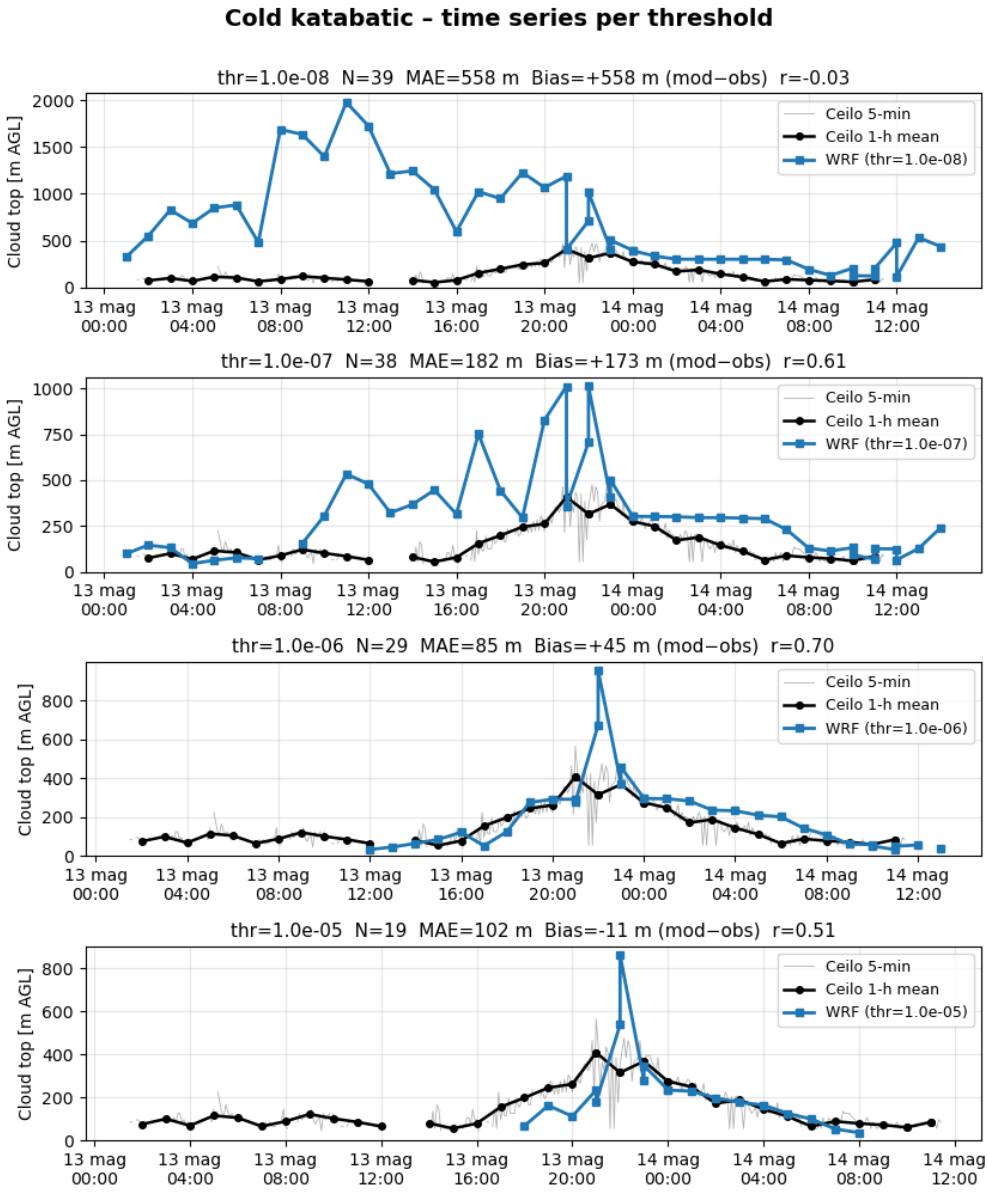


Figure B.7: Timeseries, for the Cold Katabatic event, of the cloud top obtained from the ceilometer algorithm (black) and from CRYOWRF (blue), where the top in the model is defined as the height where the blowing snow mixing ratio reaches a selected threshold. Thresholds from $10^{-8}\,\mathrm{kg\,kg^{-1}}$ to $10^{-5}\,\mathrm{kg\,kg^{-1}}$ are shown here. $10^{-6}\,\mathrm{kg\,kg^{-1}}$ follows the observed cloud best.

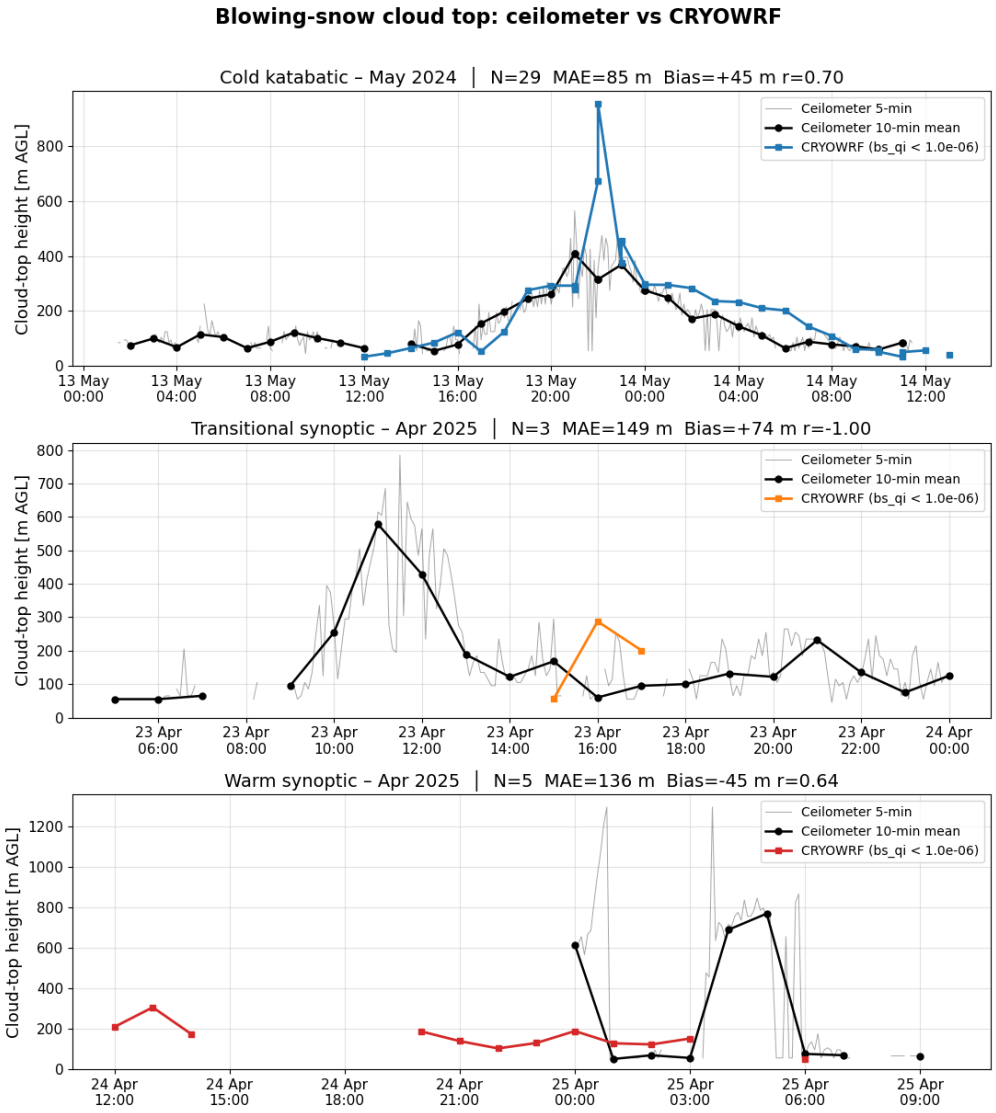


Figure B.8: Blowing snow cloud top observed by the ceilometer (retrieved with the ceilometer algorithm of Section 2.2) and modelled by CRYOWRF. Modelled cloud top (colored lines) is defined as the height where the blowing snow mixing ratio is equal to $10^{-6}\,\mathrm{kg\,kg^{-1}}$. The three panels show the three simulated events. The black fine line is the cloud top retrieved from the ceilometer at 5 minute resolution, the black line instead the points used for comparison with CRYOWRF. In the two synoptic events, the transitional one especially, the modelled cloud reaches more rarely the selected threshold of $bs_qi = 10^{-6}\,\mathrm{kg\,kg^{-1}}$.

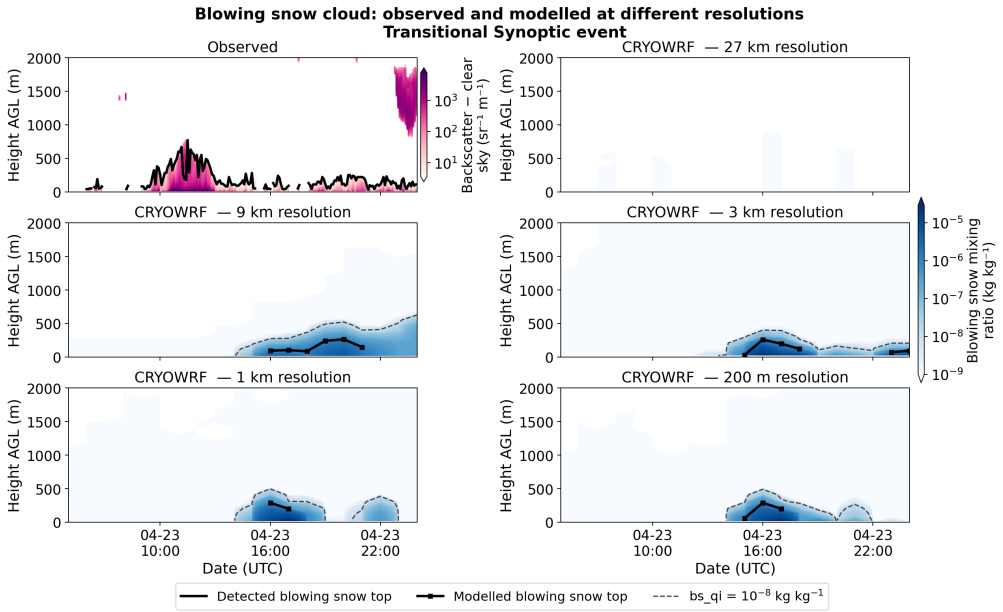


Figure B.9: Same as Figure 4.2, but for the Transitional Synoptic event instead. In this event, there is no significant change in the simulated blowing snow cloud until up to 27 km horizontal resolution, where it disappears.

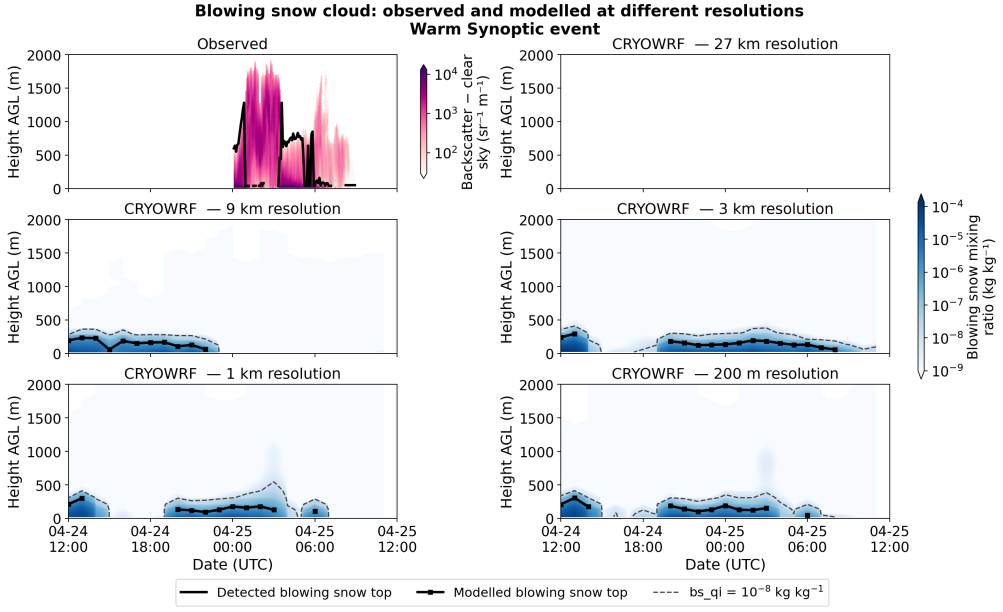


Figure B.10: Same as Figure 4.2, but for the Warm Synoptic event instead. In this event, there is no significant change in the simulated blowing snow cloud until up to 27 km horizontal resolution, where it disappears.

Bibliography

Agosta, Cécile, Charles Amory, Christoph Kittel, Anais Orsi, Vincent Favier, Hubert Gallée, Michiel R. van den Broeke, Jan T. M. Lenaerts, Jan Melchior van Wessem, Willem Jan van de Berg, and Xavier Fettweis (Jan. 29, 2019). «Estimation of the Antarctic surface mass balance using the regional climate model MAR (1979–2015) and identification of dominant processes». In: *The Cryosphere* 13.1, pp. 281–296. ISSN: 1994-0416. DOI: 10.5194/tc-13-281-2019. URL: https://tc.copernicus.org/articles/13/281/2019/ (visited on 02/24/2026).

Amory, ., A. Trouvilliez, H. Gallée, V. Favier, F. Naaim-Bouvet, C. Genthon, C. Agosta, L. Piard, and H. Bellot (July 30, 2015). «Comparison between observed and simulated aeolian snow mass fluxes in Adélie Land, East Antarctica». In: *The Cryosphere* 9.4, pp. 1373–1383. ISSN: 1994-0424. DOI: 10.5194/tc-9-1373-2015. URL: https://tc.copernicus.org/articles/9/1373/2015/ (visited on 06/15/2026).

Amory, Charles (May 29, 2020). «Drifting-snow statistics from multiple-year autonomous measurements in Adélie Land, East Antarctica». In: *The Cryosphere* 14.5, pp. 1713–1725. ISSN: 1994-0416. DOI: 10.5194/tc-14-1713-2020. URL: https://tc.copernicus.org/articles/14/1713/2020/ (visited on 02/18/2026).

Amory and Christoph Kittel (Dec. 19, 2019). «Brief communication: Rare ambient saturation during drifting snow occurrences at a coastal location of East Antarctica». In: *The Cryosphere* 13.12, pp. 3405–3412. ISSN: 1994-0424. DOI: 10.5194/tc-13-3405-2019. URL: https://tc.copernicus.org/articles/13/3405/2019/ (visited on 06/16/2026).

Armstrong, R.L. and E. Brun (2008). «Snow and climate: physical processes, surface energy exchange and modelling. Cambridge, etc., Cambridge University Press. 256pp. ISBN-10: 0-521854-54-7, ISBN-13: 978-0-52185-454-7, hardback, £65/US$130.» In: *Journal of Glaciology* 55.190, pp. 384–384. ISSN: 0022-1430, 1727-5652. DOI: 10.3189/002214309788608741. URL: https://www.cambridge.org/core/journals/journal-of-glaciology/article/rl-armstrong-and-

e-brun-eds-2008-snow-and-climate-physical-processes-surface-energy-exchange-and-modelling-cambridge-etc-cambridge-university-press-256pp-isbn10-0521854547-isbn13-9780521854547-hardback-65us130/72AD88148BE78B7C64BB71E5F87D1D87 (visited on 03/05/2026).

Bartelt, Perry and Michael Lehning (Nov. 2002). «A physical SNOWPACK model for the Swiss avalanche warning». In: *Cold Regions Science and Technology* 35.3, pp. 123–145. ISSN: 0165232X. DOI: 10.1016/S0165-232X(02)00074-5. URL: https://linkinghub.elsevier.com/retrieve/pii/S0165232X02000745 (visited on 07/01/2026).

Bintanja, Richard (1999). «On the glaciological, meteorological, and climatological significance of Antarctic blue ice areas». In: *Reviews of Geophysics* 37.3. _eprint: https://agupubs.onlinelibrary.wiley.com/doi/pdf/10.1029/1999RG900007, pp. 337–359. ISSN: 1944-9208. DOI: 10.1029/1999RG900007. URL: https://onlinelibrary.wiley.com/doi/abs/10.1029/1999RG900007 (visited on 03/05/2026).

– (June 2000). «Snowdrift Suspension And Atmospheric Turbulence. Part II: Results Of Model Simulations». In: *Boundary-Layer Meteorology* 95.3, pp. 369–395. ISSN: 0006-8314, 1573-1472. DOI: 10.1023/A:1002643921326. URL: https://link.springer.com/10.1023/A:1002643921326 (visited on 06/16/2026).

Dattler, Marissa E., Jan T. M. Lenaerts, and Brooke Medley (2019). «Significant Spatial Variability in Radar-Derived West Antarctic Accumulation Linked to Surface Winds and Topography». In: *Geophysical Research Letters* 46.22. _eprint: https://agupubs.onlinelibrary.wiley.com/doi/pdf/10.1029/2019GL085363, pp. 13126–13134. ISSN: 1944-8007. DOI: 10.1029/2019GL085363. URL: https://onlinelibrary.wiley.com/doi/abs/10.1029/2019GL085363 (visited on 03/05/2026).

Deb, Pranab, Andrew Orr, J. Scott Hosking, Tony Phillips, John Turner, Daniel Bannister, James O. Pope, and Steve Colwell (Feb. 27, 2016). «An assessment of the Polar Weather Research and Forecasting (WRF) model representation of near-surface meteorological variables over West Antarctica». In: *Journal of Geophysical Research: Atmospheres* 121.4, pp. 1532–1548. ISSN: 2169-897X, 2169-8996. DOI: 10.1002/2015JD024037. URL: https://agupubs.onlinelibrary.wiley.com/doi/10.1002/2015JD024037 (visited on 07/14/2026).

Fujiwhara, S. (1921). «The natural tendency towards symmetry of motion and its application as a principle in meteorology». In: *Quarterly Journal of the Royal Meteorological Society* 47.200, pp. 287–292. ISSN: 1477-870X. DOI: 10.1002/qj.49704720010. URL: https://onlinelibrary.wiley.com/doi/abs/10.1002/qj.49704720010 (visited on 06/09/2026).

Gadde, Srinidhi and Willem Jan van de Berg (Nov. 2, 2024). «Contribution of blowing-snow sublimation to the surface mass balance of Antarctica». In: *The Cryosphere* 18.11, pp. 4933–4953. ISSN: 1994-0416. DOI: 10.5194/tc-18-4933-

2024. URL: https://tc.copernicus.org/articles/18/4933/2024/ (visited on 06/09/2026).

Gallée, Hubert, Gilbert Guyomarc'h, and Eric Brun (Apr. 2001). «Impact Of Snow Drift On The Antarctic Ice Sheet Surface Mass Balance: Possible Sensitivity To Snow-Surface Properties». In: *Boundary-Layer Meteorology* 99.1, pp. 1–19. ISSN: 0006-8314, 1573-1472. DOI: 10.1023/A:1018776422809. URL: https://link.springer.com/10.1023/A:1018776422809 (visited on 06/15/2026).

Gerber, Franziska, Varun Sharma, and Michael Lehning (June 27, 2023). «CRYOWRF—Model Evaluation and the Effect of Blowing Snow on the Antarctic Surface Mass Balance». In: *Journal of Geophysical Research: Atmospheres* 128.12, e2022JD037744. ISSN: 2169-897X, 2169-8996. DOI: 10.1029/2022JD037744. URL: https://agupubs.onlinelibrary.wiley.com/doi/10.1029/2022JD037744 (visited on 02/16/2026).

González-Herrero, Sergi (Apr. 2025). «A tall tower to measure the blowing snow in Antarctica». In: *Nature Reviews Earth & Environment* 6.4, pp. 229–229. ISSN: 2662-138X. DOI: 10.1038/s43017-025-00664-z. URL: https://www.nature.com/articles/s43017-025-00664-z (visited on 06/09/2026).

Gorodetskaya, I. V., S. Kneifel, M. Maahn, K. Van Tricht, W. Thiery, J. H. Schween, A. Mangold, S. Crewell, and N. P. M. Van Lipzig (Feb. 11, 2015). «Cloud and precipitation properties from ground-based remote-sensing instruments in East Antarctica». In: *The Cryosphere* 9.1, pp. 285–304. ISSN: 1994-0416. DOI: 10.5194/tc-9-285-2015. URL: https://tc.copernicus.org/articles/9/285/2015/ (visited on 05/04/2026).

Gorodetskaya, I. V., N. P. M. Van Lipzig, M. R. Van den Broeke, A. Mangold, W. Boot, and C. H. Reijmer (2013). «Meteorological regimes and accumulation patterns at Utsteinen, Dronning Maud Land, East Antarctica: Analysis of two contrasting years». In: *Journal of Geophysical Research: Atmospheres* 118.4, pp. 1700–1715. ISSN: 2169-8996. DOI: 10.1002/jgrd.50177. URL: https://onlinelibrary.wiley.com/doi/abs/10.1002/jgrd.50177 (visited on 02/19/2026).

Gossart, Alexandra, Stephen P. Palm, Niels Souverijns, Jan T. M. Lenaerts, Irina V. Gorodetskaya, Stef Lhermitte, and Nicole P. M. van Lipzig (July 8, 2020). «Importance of Blowing Snow During Cloudy Conditions in East Antarctica: Comparison of Ground-Based and Space-Borne Retrievals Over Ice-Shelf and Mountain Regions». In: *Frontiers in Earth Science* 8. ISSN: 2296-6463. DOI: 10.3389/feart.2020.00240. URL: https://www.frontiersin.org/journals/earth-science/articles/10.3389/feart.2020.00240/full (visited on 02/18/2026).

Gossart, Alexandra, Niels Souverijns, Irina V. Gorodetskaya, Stef Lhermitte, Jan T. M. Lenaerts, Jan H. Schween, Alexander Mangold, Quentin Laffineur, and

Nicole P. M. Van Lipzig (Dec. 5, 2017). «Blowing snow detection from ground-based ceilometers: Application to East Antarctica». In: *The Cryosphere* 11.6, pp. 2755–2772. ISSN: 1994-0424. DOI: 10.5194/tc-11-2755-2017. URL: https://tc.copernicus.org/articles/11/2755/2017/ (visited on 02/16/2026).

Kausch, Thore, Stef Lhermitte, Jan T. M. Lenaerts, Nander Wever, Mana Inoue, Frank Pattyn, Sainan Sun, Sarah Wauthy, Jean-Louis Tison, and Willem Jan van de Berg (Oct. 9, 2020). «Impact of coastal East Antarctic ice rises on surface mass balance: insights from observations and modeling». In: *The Cryosphere* 14.10, pp. 3367–3380. ISSN: 1994-0416. DOI: 10.5194/tc-14-3367-2020. URL: https://tc.copernicus.org/articles/14/3367/2020/ (visited on 03/05/2026).

Klugmann, Dirk, K. Heinsohn, and H.-J Kirtzel (Jan. 1, 1996). «A low cost 24 GHz FM-CW doppler radar rain profiler». In: *Contributions to Atmospheric Physics* 69, pp. 247–253.

Kneifel, Stefan, Maximilian Maahn, Gerhard Peters, and Clemens Simmer (2011). «Observation of snowfall with a low-power FM-CW K-band radar (Micro Rain Radar)». In: *Meteorology and atmospheric physics* 113.1, pp. 75–87. ISSN: 0177-7971. DOI: 10.1007/s00703-011-0142-z.

Kotthaus, Simone, Ewan O'Connor, Christoph Münkel, Cristina Charlton-Perez, Martial Haeffelin, Andrew M. Gabey, and C. Sue B. Grimmond (Aug. 17, 2016). «Recommendations for processing atmospheric attenuated backscatter profilesfrom Vaisala CL31 ceilometers». In: *Atmospheric Measurement Techniques* 9.8, pp. 3769–3791. ISSN: 1867-8548. DOI: 10.5194/amt-9-3769-2016. URL: https://amt.copernicus.org/articles/9/3769/2016/ (visited on 06/14/2026).

Krinner, Gerhard, Chris Derksen, Richard Essery, Mark Flanner, Stefan Hagemann, Martyn Clark, Alex Hall, Helmut Rott, Claire Brutel-Vuilmet, Hyungjun Kim, Cécile B. Ménard, Lawrence Mudryk, Chad Thackeray, Libo Wang, Gabriele Arduini, Gianpaolo Balsamo, Paul Bartlett, Julia Boike, Aaron Boone, Frédérique Chéruy, Jeanne Colin, Matthias Cuntz, Yongjiu Dai, Bertrand Decharme, Jeff Derry, Agnès Ducharne, Emanuel Dutra, Xing Fang, Charles Fierz, Josephine Ghattas, Yeugeniy Gusev, Vanessa Haverd, Anna Kontu, Matthieu Lafaysse, Rachel Law, Dave Lawrence, Weiping Li, Thomas Marke, Danny Marks, Martin Ménégoz, Olga Nasonova, Tomoko Nitta, Masashi Niwano, John Pomeroy, Mark S. Raleigh, Gerd Schaedler, Vladimir Semenov, Tanya G. Smirnova, Tobias Stacke, Ulrich Strasser, Sean Svenson, Dmitry Turkov, Tao Wang, Nander Wever, Hua Yuan, Wenyan Zhou, and Dan Zhu (Dec. 10, 2018). «ESM-SnowMIP: assessing snow models and quantifying snow-related climate feedbacks». In: *Geoscientific Model Development* 11.12, pp. 5027–5049. ISSN: 1991-9603. DOI: 10.5194/gmd-11-5027-2018. URL: https://gmd.copernicus.org/articles/11/5027/2018/ (visited on 06/16/2026).

Lehning, Michael, Perry Bartelt, Bob Brown, and Charles Fierz (Nov. 2002a). «A physical SNOWPACK model for the Swiss avalanche warning». In: *Cold Regions Science and Technology* 35.3, pp. 169–184. ISSN: 0165232X. DOI: 10.1016/S0165-232X(02)00072-1. URL: https://linkinghub.elsevier.com/retrieve/pii/S0165232X02000721 (visited on 07/01/2026).

Lehning, Michael, Perry Bartelt, Bob Brown, Charles Fierz, and Pramod Satyawali (Nov. 2002b). «A physical SNOWPACK model for the Swiss avalanche warning». In: *Cold Regions Science and Technology* 35.3, pp. 147–167. ISSN: 0165232X. DOI: 10.1016/S0165-232X(02)00073-3. URL: https://linkinghub.elsevier.com/retrieve/pii/S0165232X02000733 (visited on 06/16/2026).

Lehning, Michael, Judith Doorschot, and Perry Bartelt (2000). «A snowdrift index based on SNOWPACK model calculations». In: *Annals of Glaciology* 31, pp. 382–386. ISSN: 0260-3055, 1727-5644. DOI: 10.3189/172756400781819770. URL: https://www.cambridge.org/core/product/identifier/S0260305500267116/type/journal_article (visited on 06/16/2026).

Lehning, F. Naaim, M. Naaim, B. Brabec, J. Doorschot, Y. Durand, G. Guyomarc'h, J.-L. Michaux, and M. Zimmerli (Dec. 31, 2002). «Snow drift: acoustic sensors for avalanche warning and research». In: *Natural Hazards and Earth System Sciences* 2.3, pp. 121–128. ISSN: 1684-9981. DOI: 10.5194/nhess-2-121-2002. URL: https://nhess.copernicus.org/articles/2/121/2002/ (visited on 07/26/2026).

Lenaerts and M. R. van den Broeke (Mar. 16, 2012a). «Modeling drifting snow in Antarctica with a regional climate model: 2. Results». In: *Journal of Geophysical Research: Atmospheres* 117 (D5). ISSN: 2156-2202. URL: https://onlinelibrary.wiley.com/doi/abs/10.1029/2010JD015419 (visited on 03/05/2026).

Lenaerts, S. Lhermitte, R. Drews, S. R. M. Ligtenberg, S. Berger, V. Helm, C. J. P. P. Smeets, M. R. van den Broeke, W. J. van de Berg, E. van Meijgaard, M. Eijkelboom, O. Eisen, and F. Pattyn (Jan. 2017). «Meltwater produced by wind–albedo interaction stored in an East Antarctic ice shelf». In: *Nature Climate Change* 7.1, pp. 58–62. ISSN: 1758-6798. DOI: 10.1038/nclimate3180. URL: https://www.nature.com/articles/nclimate3180 (visited on 03/05/2026).

Lenaerts, Brooke Medley, Michiel R. van den Broeke, and Bert Wouters (June 2019). «Observing and Modeling Ice Sheet Surface Mass Balance». In: *Reviews of Geophysics (Washington, D.C. : 1985)* 57.2, pp. 376–420. ISSN: 8755-1209. DOI: 10.1029/2018RG000622. URL: https://pmc.ncbi.nlm.nih.gov/articles/PMC6774314/ (visited on 06/16/2026).

Lenaerts, M. R. Van Den Broeke, S. J. Déry, E. Van Meijgaard, W. J. Van De Berg, Stephen P. Palm, and J. Sanz Rodrigo (Mar. 16, 2012b). «Modeling drifting snow in Antarctica with a regional climate model: 1. Methods and model evaluation». In: *Journal of Geophysical Research: Atmospheres* 117 (D5), 2011JD016145. ISSN: 0148-0227. DOI: 10.1029/2011JD016145. URL: https:

//agupubs.onlinelibrary.wiley.com/doi/10.1029/2011JD016145 (visited on 06/15/2026).

Li, Long and John W. Pomeroy (Mar. 1997). «Estimates of Threshold Wind Speeds for Snow Transport Using Meteorological Data». In: *Journal of Applied Meteorology* 36.3, pp. 205–213. ISSN: 0894-8763, 1520-0450. DOI: 10.1175/1520-0450(1997)036<0205:EOTWSF>2.0.CO;2. URL: http://journals.ametsoc.org/doi/10.1175/1520-0450(1997)036%3C0205:EOTWSF%3E2.0.CO;2 (visited on 07/20/2026).

Loeb, Nicole A. and Aaron Kennedy (Apr. 16, 2021). «Blowing Snow at McMurdo Station, Antarctica During the AWARE Field Campaign: Surface and Ceilometer Observations». In: *Journal of Geophysical Research: Atmospheres* 126.7, e2020JD033935. ISSN: 2169-8996. DOI: 10.1029/2020JD033935. URL: https://agupubs.onlinelibrary.wiley.com/doi/10.1029/2020JD033935 (visited on 04/09/2026).

Maahn, M. and P. Kollias (2012). «Improved Micro Rain Radar snow measurements using Doppler spectra post-processing». In: *Atmospheric measurement techniques* 5.11, pp. 2661–2673. ISSN: 1867-8548. DOI: 10.5194/amt-5-2661-2012.

McErlich, Cameron, Adrian McDonald, James Renwick, and Alex Schuddeboom (Nov. 27, 2023). «An Assessment of Southern Hemisphere Extratropical Cyclones in ERA5 Using WindSat». In: *Journal of Geophysical Research: Atmospheres* 128.22, e2023JD038554. ISSN: 2169-897X, 2169-8996. DOI: 10.1029/2023JD038554. URL: https://agupubs.onlinelibrary.wiley.com/doi/10.1029/2023JD038554 (visited on 07/20/2026).

Melo, Daniela Brito, Armin Sigmund, and Michael Lehning (Mar. 20, 2024). «Understanding snow saltation parameterizations: lessons from theory, experiments and numerical simulations». In: *The Cryosphere* 18.3, pp. 1287–1313. ISSN: 1994-0416. DOI: 10.5194/tc-18-1287-2024. URL: https://tc.copernicus.org/articles/18/1287/2024/ (visited on 03/25/2026).

Niigata Electric Co., Ltd. (2019). *SPC Low Temperature Test Sheet, Sensor No. 1603*.

– (n.d.). *Snow Particle Counter SPC-95 Installation Manual, Sensor No. 1604*.

Nishimura, Kouichi and Masaki Nemoto (July 15, 2005). «Blowing snow at Mizuho station, Antarctica». In: *Philosophical Transactions of the Royal Society A: Mathematical, Physical and Engineering Sciences* 363.1832, pp. 1647–1662. ISSN: 1364-503X, 1471-2962. DOI: 10.1098/rsta.2005.1599. URL: https://royalsocietypublishing.org/doi/10.1098/rsta.2005.1599 (visited on 02/23/2026).

O'Connor, Ewan J., Anthony J. Illingworth, and Robin J. Hogan (May 2004). «A Technique for Autocalibration of Cloud Lidar». In: *Journal of Atmospheric and Oceanic Technology* 21.5, pp. 777–786. ISSN: 0739-0572, 1520-0426. DOI: 10.1175/1520-0426(2004)021<0777:ATFAOC>2.0.CO;2. URL: http://journals.

ametsoc.org/doi/10.1175/1520-0426(2004)021%3C0777:ATFAOC%3E2.0.CO;2 (visited on 06/19/2026).

Organization, World Meteorological (2017). *Drifting and Blowing Snow*. International Cloud Atlas: Manual on the Observation of Clouds and Other Meteors (WMO-No. 407). URL: https://cloudatlas.wmo.int/drifting-and-blowing-snow.html (visited on 07/16/2026).

Otsu, Nobuyuki (Jan. 1979). «A Threshold Selection Method from Gray-Level Histograms». In: *IEEE Transactions on Systems, Man, and Cybernetics* 9.1, pp. 62–66. ISSN: 0018-9472, 2168-2909. DOI: 10.1109/TSMC.1979.4310076. URL: http://ieeexplore.ieee.org/document/4310076/ (visited on 07/29/2026).

Palm, Stephen P., Vinay Kayetha, Yuekui Yang, and Rebecca Pauly (2017). «Blowing Snow Sublimation and Transport over Antarctica from 11 Years of CALIPSO Observations». In: *The cryosphere* 11.6, pp. 2555–2569. ISSN: 1994-0424. DOI: 10.5194/tc-11-2555-2017.

Palm, Stephen P., Yuekui Yang, James D. Spinhirne, and Alexander Marshak (2011). «Satellite remote sensing of blowing snow properties over Antarctica». In: *Journal of Geophysical Research: Atmospheres* 116 (D16). _eprint: https://agupubs.onlinelibrary.wiley.com/doi/pdf/10.1029/2011JD015828. ISSN: 2156-2202. DOI: 10.1029/2011JD015828. URL: https://onlinelibrary.wiley.com/doi/abs/10.1029/2011JD015828 (visited on 03/05/2026).

Parish, Thomas R. and David H. Bromwich (May 1, 2007). «Reexamination of the Near-Surface Airflow over the Antarctic Continent and Implications on Atmospheric Circulations at High Southern Latitudes». In: *Monthly Weather Review* 135.5, pp. 1961–1973. ISSN: 1520-0493, 0027-0644. DOI: 10.1175/MWR3374.1. URL: https://journals.ametsoc.org/view/journals/mwre/135/5/mwr3374.1.xml (visited on 03/06/2026).

Peters, Gerhard, Bernd Fischer, Hans Münster, Marco Clemens, and Andreas Wagner (Dec. 1, 2005). «Profiles of Raindrop Size Distributions as Retrieved by Microrain Radars». In: *Journal of Applied Meteorology and Climatology* 44.12, pp. 1930–1949. ISSN: 1520-0450, 0894-8763. DOI: 10.1175/JAM2316.1. URL: https://journals.ametsoc.org/view/journals/apme/44/12/jam2316.1.xml (visited on 02/17/2026).

Picard, Ghislain, Laurent Arnaud, Romain Caneill, Eric Lefebvre, and Maxim Lamare (July 17, 2019). «Observation of the process of snow accumulation on the Antarctic Plateau by time lapse laser scanning». In: *The Cryosphere* 13.7, pp. 1983–1999. ISSN: 1994-0416. DOI: 10.5194/tc-13-1983-2019. URL: https://tc.copernicus.org/articles/13/1983/2019/ (visited on 03/05/2026).

Priestley, Matthew D. K., Duncan Ackerley, Jennifer L. Catto, and Kevin I. Hodges (Mar. 2023). «Drivers of Biases in the CMIP6 Extratropical Storm Tracks. Part II: Southern Hemisphere». In: *Journal of Climate* 36.5, pp. 1469–1486. ISSN: 0894-8755, 1520-0442. DOI: 10.1175/JCLI-D-20-0977.1. URL: https://

journals.ametsoc.org/view/journals/clim/36/5/JCLI-D-20-0977.1.xml (visited on 06/09/2026).

Reynolds, Dylan, Michael Haugeneder, Michael Lehning, and Rebecca Mott (June 5, 2024). «Intermediate complexity atmospheric modeling in complex terrain: is it right?» In: *Frontiers in Earth Science* 12, p. 1388416. ISSN: 2296-6463. DOI: 10.3389/feart.2024.1388416. URL: https://www.frontiersin.org/articles/10.3389/feart.2024.1388416/full (visited on 07/31/2026).

Sato, Takeshi, Tadashi Kimura, Taminoe Ishimaru, and Toshisuke Maruyama (1993). «Field test of a new snow-particle counter (SPC) system». In: *Annals of Glaciology* 18, pp. 149–154. ISSN: 0260-3055, 1727-5644. DOI: 10.3189/S0260305500011411. URL: https://www.cambridge.org/core/product/identifier/S0260305500011411/type/journal_article (visited on 06/18/2026).

Scambos, T.A., M. Frezzotti, T. Haran, J. Bohlander, J.T.M. Lenaerts, M.R. Van Den Broeke, K. Jezek, D. Long, S. Urbini, K. Farness, T. Neumann, M. Albert, and J.-G. Winther (2012). «Extent of low-accumulation 'wind glaze' areas on the East Antarctic plateau: implications for continental ice mass balance». In: *Journal of Glaciology* 58.210. Edition: 2017/09/08, pp. 633–647. ISSN: 0022-1430. DOI: 10.3189/2012JoG11J232. URL: https://www.cambridge.org/core/product/712C217F44D42B0AF2C9365C1FB359F1.

Scarchilli, Claudio, Massimo Frezzotti, Paolo Grigioni, Lorenzo De Silvestri, Lucia Agnoletto, and Stefano Dolci (June 1, 2010). «Extraordinary blowing snow transport events in East Antarctica». In: *Climate Dynamics* 34.7, pp. 1195–1206. ISSN: 1432-0894. DOI: 10.1007/s00382-009-0601-0. URL: https://doi.org/10.1007/s00382-009-0601-0 (visited on 02/18/2026).

Schmidt, R. A. (June 1, 1982). «Vertical profiles of wind speed, snow concentration, and humidity in blowing snow». In: *Boundary-Layer Meteorology* 23.2, pp. 223–246. ISSN: 1573-1472. DOI: 10.1007/BF00123299. URL: https://doi.org/10.1007/BF00123299 (visited on 02/23/2026).

Schmidt, R. A., Rocky Mountain Forest and Range Experiment Station (U.S.) cn, and United States. Forest Service. cn (1977). *A system that measures blowing snow.* In collab. with National Agricultural Library U. S. Department of Agriculture. Fort Collins, Colo. : Rocky Mountain Forest and Range Experiment Station, Forest Service, U.S. Dept. of Agriculture. 90 pp. URL: http://archive.org/details/CAT92273412 (visited on 02/23/2026).

Sharma, Varun, Franziska Gerber, and Michael Lehning (Jan. 30, 2023). «Introducing CRYOWRF v1.0: Multiscale atmospheric flow simulations with advanced snow cover modelling». In: *Geoscientific Model Development* 16.2, pp. 719–749. ISSN: 1991-9603. DOI: 10.5194/gmd-16-719-2023. URL: https://gmd.copernicus.org/articles/16/719/2023/ (visited on 02/16/2026).

Sigmund, A., D. B. Melo, J. Dujardin, K. Nishimura, and M. Lehning (May 2025). «Parameterizing Snow Sublimation in Conditions of Drifting and Blowing

Snow». In: *Journal of Advances in Modeling Earth Systems* 17.5, e2024MS004332. ISSN: 1942-2466, 1942-2466. DOI: 10.1029/2024MS004332. URL: https://agupubs.onlinelibrary.wiley.com/doi/10.1029/2024MS004332 (visited on 07/26/2026).

Skamarock, William, Joseph Klemp, Jimy Dudhia, David Gill, Zhiquan Liu, Judith Berner, Wei Wang, Jordan Powers, Michael Duda, Dale Barker, and Xiang-Yu Huang (Mar. 1, 2019). *A Description of the Advanced Research WRF Model Version 4 NCAR TECHNICAL NOTES A Description of the Advanced Research WRF Model Version 4*.

Smoliński, A., B. Walczak, and J.W. Einax (Oct. 2002). «Hierarchical clustering extended with visual complements of environmental data set». In: *Chemometrics and Intelligent Laboratory Systems* 64.1, pp. 45–54. ISSN: 01697439. DOI: 10.1016/S0169-7439(02)00049-7. URL: https://linkinghub.elsevier.com/retrieve/pii/S0169743902000497 (visited on 07/29/2026).

Sørensen, M. (1991). «An analytic model of wind-blown sand transport». In: *Aeolian Grain Transport 1*. Ed. by Ole E. Barndorff-Nielsen and Brian B. Willetts. Vol. 1. Series Title: Acta Mechanica Supplementum. Vienna: Springer Vienna, pp. 67–81. ISBN: 978-3-211-82269-2 978-3-7091-6706-9. DOI: 10.1007/978-3-7091-6706-9_4. URL: http://link.springer.com/10.1007/978-3-7091-6706-9_4 (visited on 07/20/2026).

Souverijns, Niels, Alexandra Gossart, Irina V. Gorodetskaya, Stef Lhermitte, Alexander Mangold, Quentin Laffineur, Andy Delcloo, and Nicole P. M. van Lipzig (June 12, 2018). «How does the ice sheet surface mass balance relate to snowfall? Insights from a ground-based precipitation radar in East Antarctica». In: *The Cryosphere* 12.6, pp. 1987–2003. ISSN: 1994-0416. DOI: 10.5194/tc-12-1987-2018. URL: https://tc.copernicus.org/articles/12/1987/2018/ (visited on 06/09/2026).

Taylor, Peter (Nov. 1998). «The Thermodynamic Effects of Sublimating, Blowing Snow in the Atmospheric Boundary Layer». In: *Boundary-Layer Meteorology* 89.2, pp. 251–283. ISSN: 0006-8314, 1573-1472. DOI: 10.1023/A:1001712111718. URL: https://link.springer.com/10.1023/A:1001712111718 (visited on 06/16/2026).

Thiery, W., I. V. Gorodetskaya, R. Bintanja, N. P. M. Van Lipzig, M. R. Van den Broeke, C. H. Reijmer, and P. Kuipers Munneke (Aug. 9, 2012). «Surface and snowdrift sublimation at Princess Elisabeth station, East Antarctica». In: *The Cryosphere* 6.4, pp. 841–857. ISSN: 1994-0416. DOI: 10.5194/tc-6-841-2012. URL: https://tc.copernicus.org/articles/6/841/2012/ (visited on 02/18/2026).

Trouvilliez, Alexandre, Florence Naaim-Bouvet, Hervé Bellot, Christophe Genthon, and Hubert Gallée (Sept. 2015). «Evaluation of the FlowCapt Acoustic Sensor for the Aeolian Transport of Snow». In: *Journal of Atmospheric and Oceanic*

Technology 32.9, pp. 1630–1641. ISSN: 0739-0572, 1520-0426. DOI: 10.1175/JTECH-D-14-00104.1. URL: https://journals.ametsoc.org/view/journals/atot/32/9/jtech-d-14-00104_1.xml (visited on 06/03/2026).

Vionnet, V., E. Martin, V. Masson, G. Guyomarc'h, F. Naaim-Bouvet, A. Prokop, Y. Durand, and C. Lac (Mar. 13, 2014). «Simulation of wind-induced snow transport and sublimation in alpine terrain using a fully coupled snowpack/atmosphere model». In: *The Cryosphere* 8.2, pp. 395–415. ISSN: 1994-0424. DOI: 10.5194/tc-8-395-2014. URL: https://tc.copernicus.org/articles/8/395/2014/ (visited on 07/20/2026).

Acknowledgements

First and foremost, I would like to thank my thesis supervisors, who helped me so much all along the way: Rainette, who I could always count on, and Michi, who welcomed me into the CRYOS group in the very first month at EPFL. I would also like to thank Sergi and Hendrick, whose help was valuable and much appreciated. I count myself lucky to have been able to work with you all, from you I learned a lot, and I am grateful for the opportunities that were given to me. Finally, I would like to thank the whole CRYOS family, I am glad I got to spend this time with you.

Ci tengo a ringraziare il professor Manes, che è sempre stato estremamente disponibile.

Voglio ringraziare i miei genitori, senza il vostro supporto non sarei qui. E mamma, forse lo sai già, che se ho scelto questo percorso di studi, è per quello che tu mi hai trasmesso, insieme a nonna. Grazie a entrambi, perché ci siete sempre stati, perché mi avete sopportata quando ero insopportabile prima di un esame, sostenuta tra le molte lacrime, e festeggiato insieme a me. Ringrazio anche Greta, tra le nostre diecimila chiacchierate notturne sei diventata per me un'ancora, colei con cui posso sempre parlare di tutto, la nostra connessione è per me una delle cose più speciali che ho.

Un grazie speciale a nonna Pina, e ad Anna e Maria. Non so esprimere il bene che vi voglio.

Quest'anno via da Torino mi ha insegnato molte cose, la più importante è forse la consapevolezza che, nonostante la distanza, i miei amici ci saranno sempre. A pensarci non posso che sentirmi estremamente fortunata, e sono grata di aver trovato delle persone così speciali.

Nina, ci conosciamo ormai da tanti tanti anni, e sei ciò di più bello che mi sia rimasto dal liceo. Le sessioni passate a studiare insieme, provando tutte le aule studio di Torino, sono innumerevoli, e per me erano ormai una costante. Mi mancheranno, ma mai quanto le pause caffè. Abbiamo condiviso ben più di questo, tra viaggi, molti spritz, e chiacchierate su qualsiasi cosa. So che mi sosterrai sempre.

Grazie.

Marti, la mia fatina preferita. Non so da dove cominciare. Da quello che è stato il peggiore anno pallavolistico della nostra vita, ormai qualche anno fa, è nata un'amicizia che per me significa tutto. Grazie per essere sempre te, sempre la mia amichetta. Tu che sei sempre pronta a tirarmi su se sto male, ad ascoltarmi, a supportarmi. Sei stata la più bella scoperta che la pallavolo mi abbia regalato.

Ai miei amici del poli: Gre, Vale, Nico, Lollo, Gio e Claudio. Non so esprimere quanto io sia grata di questo nostro gruppo. Dopo anni passati a condividere tutto, ora siamo sparpagliati per il mondo. Sono fiera di ognuno di voi, e vi ringrazio per essere per sempre "gli amici dell'uni", quelli di una vita.

Ai miei amichetti della svizzera. Jordi, Ele, Ari. Grazie per avermi accolta così caldamente nel vostro gruppo. Tra giornate di studio pazzo al Rolex e pause caffé inutilmente costose e giustamente lunghe, tra picnic al lago e post su Birda, siete diventati il mio riferimento a Losanna, e degli amici che ringrazierò per sempre di avere. Sion alla fine non è che un'ora da Losanna, quindi non preoccupatevi che non vi siete ancora liberati di me.

To Céline, I count myself so lucky to have met you in that first orientation day. From there on, I got to share the fantastic experience that was Erasmus with you, and discover together the beautiful country that we landed in. For that I am grateful, it wouldn't have been the same with anyone else.